

# RECENT ADVANCES ON HYDROGEN RETENTION IN ITER'S PLASMA-FACING MATERIALS: BERYLLIUM, CARBON, AND TUNGSTEN

C. H. SKINNER,<sup>a\*</sup> A. A. HAASZ,<sup>b</sup> V. KH. ALIMOV,<sup>c</sup> N. BEKRIS,<sup>d</sup> R. A. CAUSEY,<sup>e</sup>  
R. E. H. CLARK,<sup>f</sup> J. P. COAD,<sup>g</sup> J. W. DAVIS,<sup>b</sup> R. P. DOERNER,<sup>h</sup> M. MAYER,<sup>i</sup>  
A. PISAREV,<sup>j</sup> J. ROTH,<sup>i</sup> and T. TANABE<sup>k</sup>

<sup>a</sup>Princeton Plasma Physics Laboratory, Princeton, New Jersey

<sup>b</sup>University of Toronto Institute for Aerospace Studies, Toronto, Ontario, Canada

<sup>c</sup>Institute of Physical Chemistry and Electrochemistry, Russian Academy of Sciences, Moscow, Russia

<sup>d</sup>Forschungszentrum Karlsruhe, Karlsruhe, Germany

<sup>e</sup>Sandia National Laboratories, Livermore, California

<sup>f</sup>IAEA Atomic and Molecular Data Unit, Vienna, Austria

<sup>g</sup>EURATOM/UKAEA Fusion Association, Culham Science Centre, Abingdon, OX14 3DB, United Kingdom

<sup>h</sup>University of California, San Diego, California

<sup>i</sup>Max-Planck-Institut für Plasmaphysik, EURATOM Association, Garching, Germany

<sup>j</sup>Moscow State Engineering and Physics Institute, Moscow, Russia

<sup>k</sup>Interdisciplinary Graduate School of Engineering Science, Kyushu University, Japan

Received March 21, 2008

Accepted for Publication May 14, 2008

Management of tritium inventory remains one of the grand challenges in the development of fusion energy, and the choice of plasma-facing materials is a key factor for in-vessel tritium retention. The Atomic and Molecular Data Unit of the International Atomic Energy Agency organized a Coordinated Research Project (CRP) on the overall topic of tritium inventory in fusion reactors during the period 2001–2006. This dealt with hydrogenic retention in ITER's plasma-facing materials—Be, C, and W—and in compounds (mixed materials) of these elements as well as tritium removal techniques. The results of the CRP are summarized in this paper together with recommendations for ITER. Basic parameters of diffusivity, solubility, and trapping in Be, C, and W are reviewed. For Be, the development of open porosity can account for transient hydrogenic pumping,

but long-term retention will be dominated by codeposition. Codeposition is also the dominant retention mechanism for carbon and remains a serious concern for both Be- and C-containing layers. Hydrogenic trapping in unirradiated tungsten is low but will increase with ion and neutron damage. Mixed materials will be formed in a tokamak, and these can also retain significant amounts of hydrogen isotopes. Oxidative and photon-based techniques for detritiation of plasma-facing components are described.

**KEYWORDS:** hydrogen retention, plasma-facing materials, ITER

Note: Some figures in this paper are in color only in the electronic version.

## Contents

### I. INTRODUCTION

### II. BERYLLIUM

- II.A. Solubility of Hydrogen Isotopes
- II.B. Diffusivity
- II.C. Permeation

### II.D. Implantation, Retention, and Surface Effects

### II.E. Codeposition of Beryllium with Hydrogen Isotopes

### II.F. Tokamak Results

### II.G. Beryllium Summary and Conclusions

### III. CARBON

### III.A. Diffusivity, Solubility, and Trapping

### III.B. Carbon Erosion: Laboratory Studies

#### III.B.1. Low-Energy Tritium Ion Erosion of Graphite

#### III.B.2. Hydrogen Isotope Effects on the Chemical Erosion of Carbon

\*E-mail: cskinner@pppl.gov

- III.B.3. Laboratory Studies of Chemical Erosion of DIII-D Tokamak Tiles
- III.C. Carbon Erosion: Tokamak Experience
  - III.C.1. Carbon Erosion and Deposition in JET
  - III.C.2. Carbon Erosion and Deposition in ASDEX-Upgrade
  - III.C.3. Carbon Erosion and Deposition in NSTX
  - III.C.4. Carbon Deposition and Hydrogen Isotope Retention in JT-60U
  - III.C.5. Transport and Breakup Processes of Hydrocarbons in the DIII-D Edge Plasma
- III.D. Tritium Retention in Carbon Codeposits
  - III.D.1. Dependence of Deuterium Retention on Graphite Structure
  - III.D.2. Deuterium and Tritium Retention in Codeposits Observed in JET and TFTR
  - III.D.3. Tritium Depth Profiles in Tiles Retrieved from JET and TFTR
  - III.D.4. Deuterium Retention in Codeposits Observed in ASDEX-Upgrade
  - III.D.5. Hydrogen Isotope Retention and Carbon Deposition in Tokamak Tile Gaps
  - III.D.6. Hydrogen Isotope Retention in Tokamak Dust
- III.E. Carbon Summary and Conclusions
- IV. TUNGSTEN**
  - IV.A. Diffusivity, Solubility, Permeability, and Recombination Coefficient
  - IV.B. Deuterium Depth Profiles in Tungsten Exposed to D<sup>+</sup> Ions and Deuterium Plasmas
    - IV.B.1. Tungsten Exposed to D<sup>+</sup> Ion Beams
    - IV.B.2. Tungsten Exposed to Deuterium Plasmas
  - IV.C. Blister Formation on the Tungsten Surface
  - IV.D. Temperature, Fluence, and Flux Dependence of Deuterium Retention in Tungsten
    - IV.D.1. Temperature Dependence
    - IV.D.2. Fluence Dependence
    - IV.D.3. Flux Dependence
  - IV.E. Effects of Impurities on Deuterium Trapping in Tungsten
  - IV.F. Hydrogen and Helium Trapping in Tungsten During Sequential Irradiations at 300 K
    - IV.F.1. Effect of H<sup>+</sup> or D<sup>+</sup> on He Retention
    - IV.F.2. Effect of He<sup>+</sup> on Deuterium Retention
  - IV.G. Hydrogen and Helium Trapping in Tungsten During Simultaneous Irradiations at 300 K
  - IV.H. Tokamak Experience with an All-Tungsten Machine
  - IV.I. Tungsten Summary and Conclusions
- V. HYDROGEN RETENTION IN MIXED MATERIALS**
  - V.A. Beryllium-Carbon Mixed Materials
  - V.B. Beryllium-Tungsten Mixed Materials
  - V.C. Carbon-Tungsten Mixed Materials
  - V.D. Mixed-Material Experience in Tokamaks
  - V.E. Mixed-Material Summary and Conclusions
- VI. DETRITIATION OF PLASMA-FACING MATERIALS**
  - VI.A. In Situ Detritiation by Gas Treatments
    - VI.A.1. Cleaning in Oxygen
    - VI.A.2. Use of Helium-Oxygen Discharges
  - VI.B. Photon Cleaning: Laser and Flashlamp
    - VI.B.1. General
    - VI.B.2. Flashlamp Cleaning of JET Divertor Tiles
    - VI.B.3. Laser Cleaning by Desorption of Tritium
    - VI.B.4. Detritiation by Laser Ablation
  - VI.C. Cleanup After Removal from the Tokamak
    - VI.C.1. Gamma Irradiation of Flakes
    - VI.C.2. Thermal Release of Tritium from Carbon-Based Deposits
    - VI.C.3. Detritiation of Stainless Steel
  - VI.D. Detritiation Summary and Conclusions
- VII. SUMMARY AND RECOMMENDATIONS**
- REFERENCES**

## I. INTRODUCTION

Management of tritium is a central issue in the development of magnetic fusion energy. The allowable inventory of retained tritium in a fusion reactor is limited for three reasons. First, tritium is a source term in safety assessments. The tritium inventory is controlled to ensure that any tritium released in case of a worst credible accident is below the no-evacuation limit at the site boundary. Second, tritium is expensive and in short supply. Third, the low margin for tritium breeding from lithium additionally constrains the total tritium that can be lost from the fuel cycle. In a fusion power reactor with an anticipated burn efficiency of a few percent, all three factors limit the tritium lost or retained to ~0.1% of the tritium fueled. Limitations on the allowable helium ash concentration in the core of a burning plasma and on its exhaust rate from the plasma result in more than an order of magnitude more tritium circulating through the plasma than tritium burnt in nuclear reactions, and this tritium can be retained in plasma-facing components (PFCs). The importance of these issues came to the fore during D-T experiments in TFTR and JET and in the engineering design activity for ITER.

The Atomic and Molecular Data Subcommittee of the International Fusion Research Council recommended

in 2001 that the Atomic and Molecular Data Unit of the International Atomic Energy Agency organize a Coordinated Research Project (CRP) on the overall topic of tritium inventory.<sup>1</sup> Accordingly, such a CRP was organized and included the authors as participants during a 5-yr project from 2001–2006. During the course of the CRP, a number of investigations on means of tritium retention as well as possible release mechanisms were carried out. A summary of the results from these investigations and related work is presented in this paper.

Tritium retention in the principal plasma-facing materials in ITER (beryllium, carbon, and tungsten) was studied. Section II covers the interaction of hydrogen isotopes with beryllium, including solubility, diffusivity, permeation, implantation retention, and codeposition of beryllium with hydrogen isotopes. Carbon is the topic of Sec. III. It begins with a summary of hydrogen solubility, diffusivity, and trapping parameters and reports on low-energy tritium ion erosion of graphite, hydrogen isotope effects on the chemical erosion of carbon, and chemical erosion of DIII-D divertor tiles—all of which result in source terms for impurity production and subsequent re-deposition potentially leading to tritium trapping in codeposits. Tokamak experience related to erosion and tritium retention including retention in dust is also discussed. Tungsten is covered in Sec. IV, including a

summary of hydrogen solubility, diffusivity parameters, and hydrogen and helium trapping under irradiation. Also covered is the dependence of D retention in W on the following parameters: surface and background gas impurities, temperature,  $D^+$  flux and fluence, post-irradiation air exposure, and post-irradiation time delay. Mixing of these materials is expected in the course of their interaction with the plasma. Section V covers Be/C, Be/W, and C/W compounds and the mixed-material experience in tokamaks. Once the in-vessel tritium inventory approaches the administrative limit, tritium must be removed to permit continued D-T plasma operations. Tritium removal techniques are covered in Sec. VI, including in situ gas treatments, photon cleaning including desorption and ablation, and tritium removal from the vessel after release from PFCs. Conclusions and recommendations from the CRP are given in Sec. VII.

This paper reports the work of the authors during the CRP. It is not intended as a comprehensive review of these topics and, for example, does not cover the important topic of tritium retention in neutron damaged materials. For previous papers and reviews of hydrogen retention in fusion materials, we refer the reader to Refs. 2 through 9 and the *Proceedings of the Biennial International Conferences on Plasma Surface Interactions*.<sup>10</sup>

## II. BERYLLIUM

With its low atomic number, relatively high thermal conductivity, and ability to getter oxygen impurities from the plasma, beryllium is an attractive material for the fusion reactor designer for low heat flux areas. It has been used at both the divertor and wall of JET (Ref. 11). This section will address the hydrogen solubility, diffusion, and permeation in beryllium; the retention of hydrogen in beryllium after implantation; codeposition with hydrogen; and finally tokamak results. An earlier review of tritium diffusivity and solubility in beryllium is given in Ref. 12.

### II.A. Solubility of Hydrogen Isotopes

The solubility values for hydrogen isotopes in beryllium as determined by various research groups are shown in Fig. 1. Jones and Gibson<sup>13</sup> determined the solubility of tritium in arc-cast beryllium by exposing samples to gas at fixed pressures and temperatures for times varying from 15 to 144 h. They concluded that the solubility was effectively independent of temperature. From  $\sim 550$  to 1250 K, the solubility of tritium in beryllium was reported to be a constant 6.4 appm T/Be  $\cdot$  atm<sup>1/2</sup>.

Swansiger<sup>14</sup> used 98.5 and 99.8% pure beryllium in experiments on tritium solubility in beryllium using the gas uptake technique. He reported the measured retention in the sample to be independent of sample thickness and purity. From 713 to 783 K the solubility was

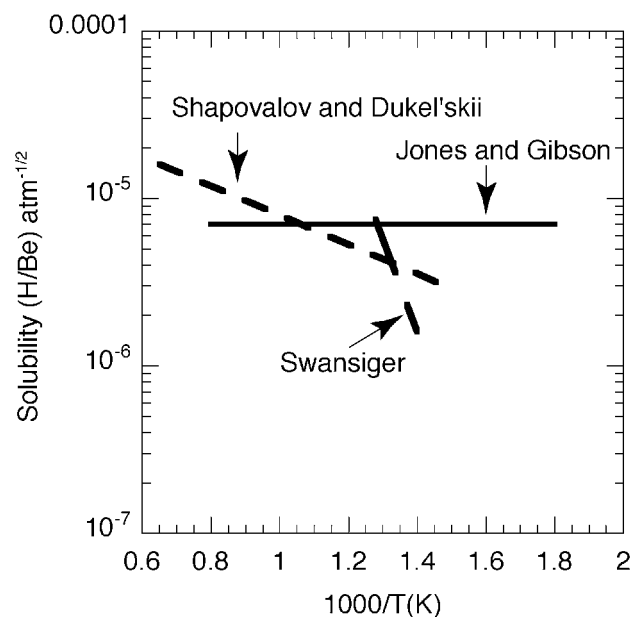


Fig. 1. Solubility of hydrogen isotopes in beryllium (from Ref. 4).

reported to be  $S = 18.2 \exp(-1.0 \text{ eV/kT}) \text{ T/Be} \cdot \text{atm}^{1/2}$ . While the amount of absorbed tritium decreased rapidly with decreasing temperature for temperatures from 783 to 713 K, it rose again as the temperature was dropped below 650 K. This effect was suggested to be due to trapping. Shapovalov and Dukel'skii<sup>15</sup> used hydrogenation to equilibrium at various hydrogen pressures with quenching and vacuum extraction to determine the solubility of hydrogen in sintered, distilled alpha beryllium. For the temperature range 673 to 1473 K, they reported the solubility to be given by  $S = 5.8 \times 10^{-5} \exp(-0.174 \text{ eV/kT}) \text{ H/Be} \cdot \text{atm}^{1/2}$ . It is interesting to examine Fig. 1 and compare the three different reported solubilities. Over the temperature ranges where the measurements were performed, all of the reported solubilities agree within an order of magnitude even though the reported activation energies vary by as much as 1 eV. It is difficult to examine these reported results and conclude that the solubility of hydrogen in beryllium behaves similarly to that of hydrogen in most metals. This will be discussed in Sec. II.G.

### II.B. Diffusivity

The Arrhenius plot for the reported diffusivities of hydrogen isotopes in beryllium is shown in Fig. 2. Jones and Gibson<sup>13</sup> studied tritium diffusion in arc-cast beryllium at temperatures from 673 to 1173 K. In their experiments, beryllium was exposed to tritium gas for various times, temperatures, and pressures during isothermal anneals. The samples were then moved to another part of the

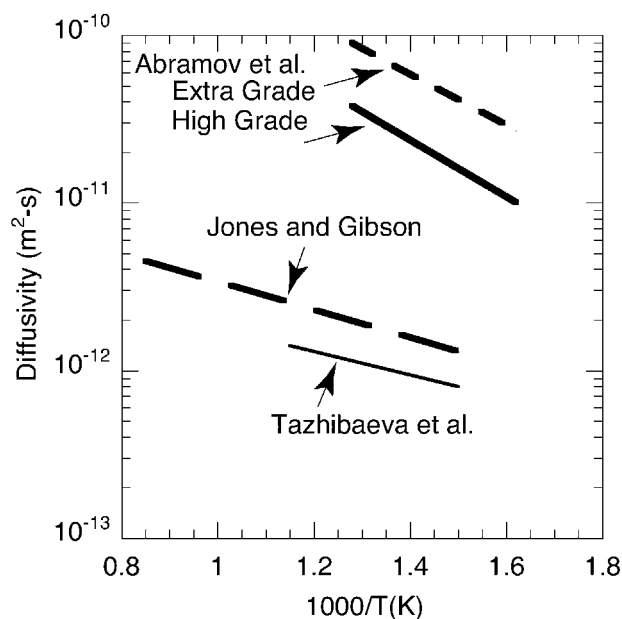


Fig. 2. Diffusivity of hydrogen isotopes in beryllium (from Ref. 4).

apparatus and heated to selected temperatures. Small amounts of hydrogen gas were present in the apparatus to dilute the released tritium. In all cases, the release was not typical of normal diffusion. At a given temperature, the release would eventually drop to almost zero, only to rise again after the temperature was increased. It was possible to repeat this stepwise increase in release several times for each sample. Relatively thick oxide layers on the samples were thought to have affected the results. Still, the data were analyzed by fitting the logarithm of fractional release versus time to determine the diffusivity at each of the anneal temperatures. Their expression for the diffusivity is given by  $D = 3 \times 10^{-11} \exp(-0.19 \text{ eV/kT}) \text{ m}^2/\text{s}$ .

Abramov et al.<sup>16</sup> determined the diffusivity of deuterium in beryllium using the gas-driven permeation technique. Two different high-purity (99.0 and 99.8%) beryllium materials were used in the experiments. Multilayer permeation theory was used in the data analysis to take into consideration the effect of the oxide layer on the permeation. For the 99.0% purity beryllium, the Arrhenius equation for the diffusivity is  $D = 8.0 \times 10^{-9} \exp(-0.36 \text{ eV/kT}) \text{ m}^2/\text{s}$ . For the 99.8% purity beryllium, the diffusivity is given by  $D = 6.7 \times 10^{-9} \exp(-0.29 \text{ eV/kT}) \text{ m}^2/\text{s}$ . In a similar study, Tazhibaeva et al.<sup>17</sup> determined diffusivities for deuterium in 98% pure beryllium using the gas-driven permeation technique. Like the Abramov et al.<sup>16</sup> work, they used the multilayer analysis technique to account for the effect of the oxide layer. Over the temperature range of 673 to 873 K, they reported the diffusivity to be  $D = 9 \times 10^{-12} \exp(-0.15 \text{ eV/kT}) \text{ m}^2/\text{s}$ .

In a series of experiments, Thompson and Macaulay-Newcombe<sup>18,19</sup> examined the diffusion of deuterium in single crystal and polycrystalline beryllium. For experiments where the deuterium was loaded from the gas phase at elevated temperatures, the effective diffusivity of the deuterium in the single crystal material was lower than that for the polycrystalline material. They reported that the diffusivity given by Abramov et al.<sup>16</sup> gave a good fit to the data for the polycrystalline beryllium. When the authors attempted to make similar measurements using implanted deuterium, they found that the effective diffusivity in the single crystals was enhanced by the beam. They suggested that the diffusivity measured for deuterium in single crystals during gas loading was the “real” diffusivity for deuterium in beryllium and that other measurements were affected by “short circuit” diffusion along grain boundaries.

### II.C. Permeation

Using both tubes and membranes, Al'tovskiy et al.<sup>20</sup> measured the gas phase permeation of hydrogen through 98.4% purity powder metallurgy beryllium. Pressures were varied from 3 to 21 atm while temperatures varied from 773 K up to 923 K. For the tubes, the activation energy of the permeation was determined to be 0.91 eV while that for the membranes was 0.28 eV. The authors did report that the permeation was affected by the grain size of the material with permeation decreasing as the grain size decreased. Oxide effects were not considered by the authors. The gas-driven technique was also used by Abramov et al.<sup>16</sup> to examine hydrogen isotope permeation through beryllium, but they were very careful in their consideration of the surface oxide. While selected values for the permeation were shown in their discussion of the pressure dependence of permeation flux (e.g.,  $P = 2.1 \times 10^{17} \text{ D/m}^2 \cdot \text{s}$  at 725 K and a pressure of  $5 \times 10^3 \text{ Pa}$ ), no values were given in the text for the permeation.

$\text{D}_3^+$  ions with an energy of 3 keV were used by Anderl et al.<sup>21</sup> at beam densities of  $\sim 5 \times 10^{19} \text{ D/m}^2 \cdot \text{s}$  to measure the ion beam-driven permeation of deuterium through 99.96% purity cast beryllium. The samples were 20 mm<sup>2</sup> with thicknesses of 25 to 71  $\mu\text{m}$ . No permeation at all was seen for temperatures below 750 K. For temperatures slightly above this temperature, permeation fractions of  $< 10^{-5}$  were recorded along with breakthrough times four orders of magnitude longer than predicted. The authors reported the upstream surface of the sample to have severe damage and pitting to a depth of 1  $\mu\text{m}$ . This damage was listed as the probable cause of the low permeation rate. The long breakthrough time was credited to trapping.

Casey et al.<sup>22</sup> used 200-eV particles but much higher fluxes ( $1.1 \times 10^{21} \text{ T/m}^2 \cdot \text{s}$ ) in their measurements of hydrogen isotope permeation through 99.4% purity S65B beryllium. Sample thicknesses were varied between 51 and 254  $\mu\text{m}$  while temperatures varied between 673 and

823 K. The permeation fractions of the implanted tritium were higher than those reported by Anderl et al.,<sup>21</sup> falling between  $5 \times 10^{-6}$  and  $2 \times 10^{-4}$ . The rate of permeation did not properly scale with sample thickness. The final conclusion of the work was that the oxide layer on the upstream and downstream sides of the sample controlled the rate of permeation.

#### II.D. Implantation, Retention, and Surface Effects

Anderl et al.<sup>23</sup> completed a very thorough review of hydrogen isotope retention in beryllium due to implantation in 1999. Some of the earliest hydrogen isotope implantation experiments for beryllium were performed by Langley.<sup>24</sup> The beryllium used in the experiments was  $\sim 99.1\%$  pure and was prepared by cold isostatic pressing followed by hot isostatic pressing. For 25-keV deuterium, he recorded nearly 100% retention until the particle fluence reached  $\sim 2 \times 10^{22}$  D/m<sup>2</sup>. Above this fluence, the retention flattened to a limit of  $\sim 2.8 \times 10^{22}$  D/m<sup>2</sup>. Similar experiments were performed by Wampler<sup>25</sup> where 99.6% purity cold and hot pressed beryllium samples were loaded to saturation with 500- and 1500-eV deuterium ions. Saturation in the implant zone occurred at an atomic ratio of  $\sim 0.31$  D/Be. Thermal release experiments of saturated samples showed the retention to be controlled by 1.0- and 1.8-eV traps. Möller et al.<sup>26</sup> implanted polycrystalline sintered S65 beryllium samples with monoenergetic deuterium ions in the energy range from 60 eV/atom to 10 keV/atom at temperatures from room temperature to 920 K. Similar to the findings of Langley,<sup>24</sup> post-irradiation examination of the samples showed oxidation of the surface, up to about 20 monolayers thickness even though the background pressure in the experimental chamber was maintained at  $10^{-8}$  Pa. Also similar to the results of Wampler,<sup>25</sup> saturation scaling linearly with particle range was noted.

In a later set of experiments using low concentrations of deuterium in zone melt recrystallized single crystal beryllium, Wampler<sup>27</sup> recorded thermal release of the deuterium controlled by a 2.3-eV trap. When the samples were prebombarded with helium to produce bubbles into which the deuterium could agglomerate, the effective permeation out of the bubbles to the surface was seen to be seven orders of magnitude lower than the value calculated using published solubility and diffusivity data. In a series of experiments on deuterium retention in several metals, Haasz and Davis<sup>28</sup> reported a 0.39 D/Be saturation in the implant zone. During thermal desorption of the deuterium after implantation, most of the deuterium was released at  $\sim 500$  K. Yoshida et al.<sup>29</sup> used 8-keV deuterium ions in their experiments with 99% pure powder metallurgy beryllium. Bubbles were seen to form for all temperatures examined between room temperature and 873 K. For temperatures above 573 K, large roundish bubbles formed at higher doses. The bubbles remained even after annealing at temperatures as high as 973 K,

agreeing with Wampler's<sup>27</sup> data showing very low permeation from bubbles. In experiments on deuterium implantation into actively cooled beryllium monoblocks using very high fluences of ions, Falter et al.<sup>30</sup> also saw the saturation-type behavior for beryllium. They compared their data for different temperatures and ion energies to others in the literature and showed the saturation values to vary directly with the energy of the particles. Macaulay-Newcombe et al.<sup>31</sup> ion implanted 99% purity hot isostatic pressed beryllium samples at 298 K using 30-keV particles. They also used gas charging of the beryllium at 773 K using deuterium gas at a pressure of 13.3 kPa. Subsequent outgassing of the ion implanted sample showed release at  $\sim 710$  and 820 K, agreeing fairly well with the earlier data of Wampler.<sup>25</sup> For the gas charging, relatively small amounts of retained deuterium were seen during desorption. Also, subsequent use of the same samples without annealing between experiments increased the amount of absorption and the temperature at which the gas was released. The oxide layer was seen to increase with each usage, possibly explaining the behavior.

Several experiments have been performed using lower-energy hydrogen isotope ions on beryllium. Hsu et al.<sup>32</sup> looked at the transient release of deuterium immediately following implantation of Brush Wellman S-65 B beryllium using a Penning discharge. In these experiments, the sample was first heated to the desired temperature (333 to 800 K), and the discharge was then initiated. The particle flux was held at  $7.4 \times 10^{20}$  D/m<sup>2</sup>·s with ion energies of 150 and 500 eV. The same sample was used for all experiments. For the experiments where the oxide layer was thought to be removed, the transient release followed a  $t^{-1}$  behavior. The integrated release increased steadily with temperature until it leveled off at 700 K. The average amount of released deuterium was  $\sim 10^{21}$  D/m<sup>2</sup>. Very intense fluxes of 100-eV deuterium and tritium ions were used by Causey et al.<sup>33</sup> in their retention measurements in S-65 beryllium. In this case the flux was varied between  $1 \times 10^{21}$  and  $2.8 \times 10^{22}$  ions/m<sup>2</sup>·s while the temperature of the measurements varied from 373 to 973 K. With the exception of the single point at 973 K, the retention decreased continuously with increasing temperature and was  $< 3 \times 10^{21}$  (D + T)/m<sup>2</sup> for all cases. Open porosity in the implant zone was listed as a possible reason for the low retention. Similar retention values were seen in the experiments on S-65B performed by Doerner et al.<sup>34</sup> using the PISCES experiment. They also listed open porosity in the implant zone as the cause of the lower than expected retention values. Sharapov et al.<sup>35</sup> used hot isostatic pressed beryllium containing 2.2% BeO in their deuterium accumulation experiments at 740 K. A plasma source with a heated cathode was used to provide atomic deuterium, and the sample was biased with a +80 V to limit the positively charged ions. They reported that the retention increased from  $2 \times 10^{20}$  to  $\sim 2 \times 10^{21}$  D/m<sup>2</sup> as the fluence increased from  $\sim 6 \times 10^{22}$  to  $2 \times 10^{24}$  D/m<sup>2</sup>. Depth profiling of the samples

showed the depth of penetration increasing from  $\sim 80$  to 460 nm as the time of exposure went from 10 min up to 240 min. They also reported the oxide layer to be growing at a rate of 0.4 to 0.5 nm/min.

Key experiments reported in Refs. 36, 37, and 38 provided the real understanding of the retention of hydrogen implanted into beryllium. Chernikov et al.<sup>36</sup> and Alimov et al.<sup>37</sup> showed that hydrogen isotope retention is strongly affected by adsorption on bubble and cavity walls. According to Chernikov et al.,<sup>36</sup> at 300 K tiny deuterium bubbles of a high volume density are formed at low fluences in 97.8% purity TIP-30 beryllium but then progress to the formation of microchannels. Even when these microchannels intersect with the surface, the deuterium retention remains at or above 8 at.%. For irradiation at 500 to 700 K, small faceted bubbles and large oblate gas-filled cavities are formed. This microstructure extends beyond the range of the implanted ions. At 700 K, the concentration of deuterium is lowered to  $\sim 0.5$  to 1.0% in the near-surface layer (0.5 to 1.0  $\mu\text{m}$ ). Alimov et al.<sup>37</sup> in their work using S-65B beryllium postulated that the retention in this porous region was due to trapping of deuterium atoms in radiation-produced vacancies, deuterium adsorption on bubble and cavity walls, and the bonding of deuterium atoms to beryllium oxide present in the surface oxide layer and as metallurgical inclusion in the bulk. Markin et al.<sup>38</sup> looked at the thermal desorption of deuterium from ion implanted TIP-30 beryllium samples. At lower temperatures, the desorption occurred at two peaks ( $\sim 460$  and 490 K). While the temperature location of the peaks did not depend on the ion fluence, the magnitude of each peak did. There was also a higher-temperature release of deuterium where the peak of the release rate increased from 850 to 1050 K as the ion fluence was increased, but the peak ultimately returned to  $\sim 850$  K as the fluence reached very high values. The lower-temperature peaks were postulated to be due to the release from the network of opened channels and to the uncovering of bubbles/closed channels to the outer surface. The higher-temperature peak was postulated to be due to liberation of deuterium atoms bound at immobile and stable vacancy complexes.

## II.E. Codeposition of Beryllium with Hydrogen Isotopes

Experiments on the codeposition of beryllium with hydrogen have been reported by Mayer,<sup>39</sup> Causey and Walsh,<sup>40</sup> and Baldwin et al.<sup>41</sup> In the study performed by Mayer,<sup>39</sup> the sputtered beryllium was produced by the impinging 0.1 mA of 4.5-keV  $\text{D}_3^+$  ions onto a beryllium disk. The sputtered beryllium was collected on a silicon collector. While the vacuum in the apparatus was quite good ( $10^{-5}$  Pa), the relatively slow sputtering process resulted in the formation of a beryllium oxide layer instead of a beryllium layer ( $\text{O}/\text{Be} \approx 1$ ). A significant amount of carbon was also detected within the codeposited layer, presumably due to the conditions of the vacuum. While

this experiment and the ones by Causey and Walsh<sup>40</sup> and Baldwin et al.<sup>41</sup> were intended to examine the codeposition of hydrogen isotopes with beryllium (or beryllium oxide), the reflection of the primary ions resulted in the formation of a co-implanted surface. In the Causey and Walsh<sup>40</sup> experiments, high flux and high fluence of 100-eV deuterons were used to sputter the beryllium. The much more intense sputtering rate of this experiment resulted in layers composed primarily of beryllium ( $\text{O}/\text{Be}$  levels varied between 0.03 and 0.125). In these experiments the level of carbon in the codeposited layer was measured to be in the 1 to 2% range. Finally, in the measurements made by Baldwin et al.,<sup>41</sup> a high flux of  $\sim 40$ -eV deuterium ions was used to sputter beryllium-coated carbon samples. Even though the target material used in these experiments was carbon, depth profiles of the codeposited material revealed relatively low carbon concentrations (in the percent range) throughout the bulk of the codeposited films. This indicates that the presence of beryllium in the plasma had reduced erosion of carbon from the target. Beryllium is then the primary material eroding from the resulting mixed Be/C surface layer (see Sec. V.A). On the other hand, the oxygen content in these films varied dramatically, being in the percent range during low-temperature collection and increasing to  $\sim 30\%$  for collection of codeposited material at elevated temperature. The results for the three experiments are shown in Fig. 3. For the Mayer/BeO experiment, the results are similar to that for the codeposition of carbon and hydrogen. For the Causey-Walsh and Baldwin et al. Be experiments, the retention is significantly lower, and the deuterium content in the layer decreases much more rapidly with the increasing temperature of the collecting

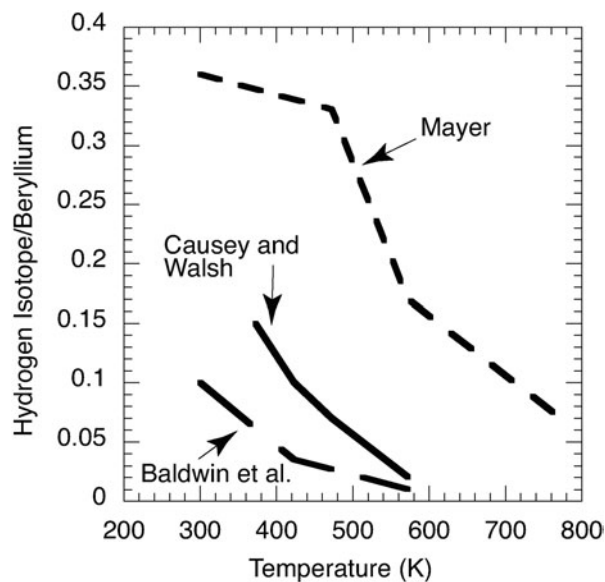


Fig. 3. Codeposition fraction of beryllium with hydrogen isotopes (adapted from Ref. 41).

material. The conclusion to be drawn from these experiments is that while the level of oxygen present in the codeposited material certainly impacts the total retention in the codeposited layer, there is also a temperature-dependent effect that dominates over the oxygen term. The deuterium content in the codeposited layers also seems to vary with the energy of the reflected ions, but this relationship is still actively being investigated.

## II.F. Tokamak Results

The behavior of the hydrogen isotopes in beryllium has been studied extensively for the JET device. Saibene et al.<sup>42</sup> used the test vessel equipped with a beryllium evaporator as used on JET to determine the hydrogen recycling coefficient for beryllium. The beryllium for these experiments was a thick in situ deposited beryllium layer  $>50 \mu\text{m}$  thick. A radio-frequency assisted direct-current discharge was used to generate hydrogen ion fluxes of  $\sim 9 \times 10^{17} \text{ H/m}^2 \cdot \text{s}$  with energies up to 1 keV. For temperatures between 373 and 523 K, the initial pumping of the hydrogen ions was very strong. At  $\sim 6$  to 8 s into the discharge, the pumping action decreased rapidly but did not drop to zero even after 60 s. During the initial stage of the discharge, the pumping parameter, defined as  $D/2K$  or diffusivity/ $(2 \times \text{recombination rate coefficient})$ , averaged  $\sim 4 \times 10^{20} \text{ m}^{-2}$ , similar to the values calculated for nickel and stainless steel. The authors stated that values this high for the pumping parameter suggest high diffusivity and relatively low recombination. Sartori et al.<sup>43</sup> used gas balance measurements in JET to examine the in-vessel retention of the hydrogen isotope fuel. They found that the amount of deuterium required to fuel the tokamak during the beryllium phase of JET was higher than that for the earlier carbon phase by a factor of  $\sim 2$  for a typical discharge. Unlike carbon, continuous gas feeding was required to maintain a density flattop when beryllium was used. Additionally, after beryllium phase discharges, the measured release fraction was increased, indicating a higher dynamic retention during the discharge. It was noted that even a thin layer of beryllium on the carbon was sufficient to change the outgassing characteristics, suggesting that the retention was driven by surface effects. Ehrenberg et al.<sup>44</sup> examined pumping with beryllium in JET during the same time period as Refs. 42 and 43. They showed that the JET beryllium pumped  $\sim 10^{21}$  deuterium atoms/s at the beginning of the shot and then continued to pump at a slower rate over the next 10 s. This rate is compared to the carbon phase where much lower initial pumping was recorded with no pumping several seconds into the shot. After the shot was terminated, the beryllium outgassing rate was proportional to  $t^{-n}$ , where  $0.6 \leq n \leq 0.7$ . This power law was obeyed from  $\sim 10$  s after termination of the discharge up to  $\sim 1000$  s. Integrating the outgassed molecules yielded recovery fractions of 30 to 70% of the amount pumped during the discharge. The authors argued that the release

could only be explained if it were recombination limited. In 1994, Andrew and Pick<sup>45</sup> gave a more detailed model of the retention and release of the hydrogen isotope fuels from the JET beryllium. They described the pumping action as due to a saturation effect over a very large fraction of the wall. The subsequent release after termination of the discharge was described as a detrapping process with subsequent recombination of the detrapped atoms.

## II.G. Beryllium Summary and Conclusions

For an understanding of the behavior of hydrogen implanted into beryllium, the defining experiments are those performed by Anderl et al.<sup>21</sup> in 1992; Yoshida et al.<sup>29</sup> in 1996; and, most importantly, the subsequent series of experiments by Chernikov et al.,<sup>36</sup> Alimov et al.,<sup>37</sup> and Marken et al.<sup>38</sup> This combination of experiments, each building on the results of the earlier data, showed the development of connected porosity in beryllium samples exposed to energetic hydrogen isotope ions with the porosity extending beyond the range of the particles. Prior to these measurements, researchers examining the interaction of hydrogen with beryllium thought of beryllium in the same manner as they would think of hydrogen in metals such as nickel, iron, or copper. The normal assumption would be that hydrogen injected into beryllium would go into solution and diffuse throughout the metal. In reality, hydrogen's behavior in beryllium is closer to that of helium in metals. The very low solubility (perhaps almost zero) of hydrogen in beryllium prevents injected hydrogen from staying in solution in beryllium. After extensive bombardment, a honeycomb-type structure extending beyond the particle range develops. At least part of this structure is composed of beryllium oxide. At lower temperatures, this structure is able to retain  $\sim 0.3$  to  $0.4 \text{ H/Be}$  (Refs. 24, 25, and 28), tied at least partially to the oxide. This behavior explains the initial strong pumping of hydrogen presented by newly exposed beryllium. It is this same porosity that is likely responsible for a sizeable fraction of the pumping seen during the later stage of the tokamak discharges. One has only to look at the honeycomb structure presented by Chernikov et al.<sup>36</sup> to understand its potential as a reservoir for stored gas. During the discharge, release of hydrogen from the saturated near-surface region provides a large excess of molecules that can flow either inward or outward through the porosity. At the end of the discharge, the gas begins to come back out of the porosity, but the tortuous path out results in time constants in the tens of seconds. A second possible mechanism of pumping during the discharge is the diffusion of atoms deeper into the material. Based on the results of experiments by Thompson and Macaulay-Newcombe<sup>18,19</sup> and Wampler,<sup>27</sup> it is postulated here that diffusion occurs along grain boundaries. The release of the atoms from these grain boundaries with their subsequent recombination add to that gas dumping back out

of the porosity to prepare the beryllium for pumping during the next discharge

Regardless of whether experimentalists finally perform the necessary experiments to determine the true form of hydrogen migration in beryllium, the behavior of beryllium in a tokamak is known. Implantation results in open porosity in any area where the beryllium faces the hydrogen plasma. This open porosity becomes an excellent getter of oxygen and forms a thin honeycomb layer of beryllium oxide. While the affinity of hydrogen to metal oxides can result in substantial hydrogen uptake in this layer, the oxide layer is expected to be very thin (nanometer-scale thickness), and hence, the global retention will still be dominated by codeposition of fuel atoms with either beryllium or carbon (if it is present).

### III. CARBON

Carbon has been extensively used in most of the recent and current major tokamak fusion reactors for shielding the vacuum vessel from the plasma, e.g., TFTR, JET, JT-60, ASDEX-Upgrade, and DIII-D. Carbon has also been selected for use in the hydrogen phase of ITER for high heat flux components in the divertor. Because of its low-Z, carbon impurities are less detrimental to the plasma compared to similar amounts of high-Z metals. Because of its excellent thermomechanical properties, carbon is able to tolerate high heat loads during off-normal events. Carbon's main drawbacks are its erosion behavior, its capacity to trap hydrogen, and diminished structural integrity and thermal conductivity due to neutron irradiation. Erosion can occur from physical sputtering, <sup>46,47</sup> radiation-enhanced sublimation, <sup>46,47</sup> and chemical reactions with the hydrogen fuel <sup>48,49</sup>—and with oxygen impurities. Chemical erosion dominates in the divertor where plasma temperatures are a few electron volts with corresponding H<sup>+</sup> energies of approximately tens of electron volts—below the threshold for physical sputtering. The chemical erosion yield of carbon can be further enhanced by the presence of some energetic (>100 eV) hydrogen or impurity ions/neutrals through a synergistic effect.<sup>50</sup> Erosion of carbon-based materials leads to the production of C atoms and hydrocarbon molecules and radicals, which can then either enter the core plasma or get transported in the plasma edge until they intercept solid surfaces where redeposition could occur. Carbon redeposition in conjunction with H isotopes can result in the formation of codeposited layers—with thicknesses reaching >100 μm—with large capacity for tritium retention in T-D burning reactors. Indeed, it is the tritium trapped in codeposits that may limit the operation of ITER, and therefore, research is underway to develop techniques for the periodic removal of T from the codeposits. Here, we present basic parameters on diffusivity, solubility, and trapping (Sec. III.A); recent results on

carbon erosion: laboratory studies (Sec. III.B) and tokamak experience (Sec. III.C); and tritium retention in carbon codeposits (Sec. III.D) including tritium retention in dust. At the time of writing (March 2008) a final decision on the use of carbon PFCs for the divertor target during the D-T operational phase is under debate by the ITER organization.

#### III.A. Diffusivity, Solubility, and Trapping

The carbon materials used in fusion reactors are different forms of graphite and carbon-fiber composites (CFCs) comprising carbon fibers embedded in a carbon matrix. The basic properties of carbon/graphite presented here are discussed in more detail in recent reviews by Causey<sup>4</sup> and Haasz and Davis.<sup>5</sup> Isotropic fine-grain graphites and CFCs have typical densities of less than ~2000 kg/m<sup>3</sup> compared with 2250 kg/m<sup>3</sup> for single crystal graphite. The latter is made up of a highly ordered structure of parallel planes, resulting in nonisotropic H diffusion along and across the planes.<sup>50–52</sup> By comparison, the less dense graphites are composed of grains (~10 μm), and the grains are further composed of crystallites (~5 nm) (Refs. 4 and 51), resulting in a highly porous structure. The Brunauer-Emmett-Teller surface area of typical graphites and CFCs is 0.25 to 1.0 m<sup>2</sup>/g (Refs. 4 and 53).

As depicted in Fig. 4, four primary mechanisms have been identified for the transport, trapping, and retention of hydrogen in carbon-based materials<sup>4,5</sup>:

1. During energetic hydrogen ion/plasma irradiation, a saturated surface layer will form within the ion range. The depth of this layer depends on the incident ion energy, and the trapped hydrogen concentration within

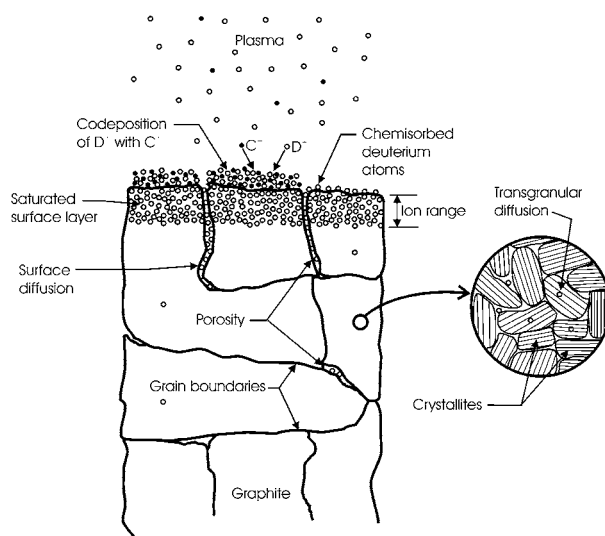


Fig. 4. Schematic of the primary mechanisms for hydrogen retention in graphite (diagram is adapted from Ref. 5).

this layer is a function of temperature; at 300 K, H/C is  $\sim 0.4$  (Ref. 5). In addition to the trapped hydrogen, mobile hydrogen is also present in the implantation zone. Mixed isotope experiments with simultaneous  $H^+-D^+$  irradiation of graphite led to the conclusion that thermalized mobile H and D atoms in the implantation zone move and recombine on internal surfaces.<sup>50,52</sup> On the other hand, during  $H^+-D^+$  irradiation,  $CH_4$  is formed at the end of the ion range.<sup>50,52</sup> The concept of trapping at the edges and within crystallites was used by Haasz et al. in their two-region model for graphite in order to reproduce experimental results for molecule formation and reemission during simultaneous  $H^+-D^+$  irradiation.<sup>51</sup>

2. Following saturation of the implantation zone, some of the mobile H atoms “diffuse” beyond this zone into the bulk, primarily along internal porous surfaces and grain boundaries, e.g., Refs. 5, 54, 55, and 56. Deep diffusion into the bulk was also observed for thermal H and D atoms, e.g., Refs. 57 and 58, and molecules,<sup>59</sup> which do not get implanted into the near surface but rather are adsorbed on porous surfaces. Surface adsorption of H atoms occurs at different types of sites with multiple or continuous activation energies (0.2 to 2.2 eV) (Refs. 4 and 60). While H atom adsorption can occur at relatively low temperatures, molecular adsorption must first involve the dissociation of  $H_2$ , requiring high temperatures, e.g., Strehlow's experiments at 1023 K (Ref. 61). Once adsorbed, the hydrogen then migrates by jumping from one surface site to another.<sup>4,51</sup> Using measured tritium profiles in POCO AXF-5Q graphite removed from TFTR and subsequently exposed to a plasma, Causey et al. derived an effective surface diffusion coefficient of  $1.2 \times 10^{-4} \exp(-0.9 \text{ eV}/kT) \text{ m}^2 \cdot \text{s}$  for hydrogen on graphite pores.<sup>4,55</sup>

3. At elevated temperatures ( $>1200 \text{ K}$ ), hydrogen undergoes transgranular diffusion in the graphite lattice,<sup>55</sup> i.e., H atom diffusion into individual grains, both along intercrystallite surfaces and within crystallites.<sup>51</sup> Although Causey<sup>4,62</sup> uses standard concepts of diffusion and trapping of hydrogen in graphite to derive coefficients of diffusion and solubility, he clearly states that “it is almost definite that hydrogen does not go into solution in the graphite crystallites.” This implies that hydrogen is trapped in the grains, at crystallite edges or in intrinsic traps within crystallites, which are accessible at temperatures above  $\sim 1200 \text{ K}$ . A trap energy of 4.3 eV was derived from the hydrogen migration study.<sup>55</sup> Neutron irradiation can significantly increase the 4.3-eV trap density, which can lead to significant tritium inventories over the temperature range of 1200 to 1500 K. At lower temperatures, the traps are not accessible by the tritium, and at higher temperatures, the trap is no longer effective.

Various experimental results on transgranular effective diffusivity and effective solubility of hydrogen in graphite are shown in Fig. 5 (Refs. 62 through 66) and

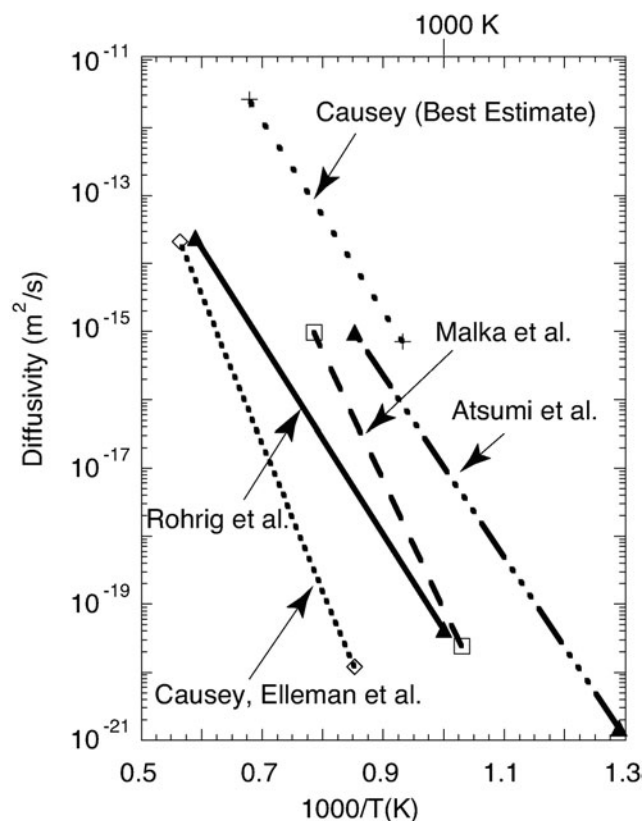


Fig. 5. Effective diffusivity of hydrogen in graphite grains. Data are from Causey,<sup>62</sup> Malka et al.,<sup>66</sup> Atsumi et al.,<sup>63</sup> Rohrig et al.,<sup>65</sup> and Causey et al.,<sup>64</sup> all contained in Ref. 4.

Fig. 6 (Refs. 62 and 63), respectively. Here, we include expressions of effective diffusivity and effective solubility given by Causey<sup>62</sup> and Atsumi et al.<sup>63</sup>:

Diffusivity

Causey (best estimate)<sup>62</sup>

$$D = 9.3 \times 10^{-5} \exp(-2.8 \text{ eV}/kT) \text{ m}^2 \cdot \text{s}$$

Atsumi et al.<sup>63</sup>

$$D = 1.69 \times 10^{-4} \exp(-2.6 \text{ eV}/kT) \text{ m}^2 \cdot \text{s}$$

Solubility

Atsumi et al.<sup>63</sup>

$$S = 6.4 \times 10^{-5} \exp(+0.2 \text{ eV}/kT) \text{ atom fraction/atm}^{0.5}$$

4. The fourth mechanism for trapping hydrogen is codeposition, which entails the formation of hydrogen-containing carbon layers via the codeposition of eroded C atoms and C-containing molecules and/or radicals in combination with hydrogen. Codeposits can form on both plasma-facing and shadowed areas in tokamaks. In JET, codeposits have been observed to exceed  $200 \mu\text{m}$  (see Sec. III.C.1). It is expected that tritium retention in ITER will be dominated by codeposition. Techniques for the removal of D from codeposits are discussed in Sec. VI.

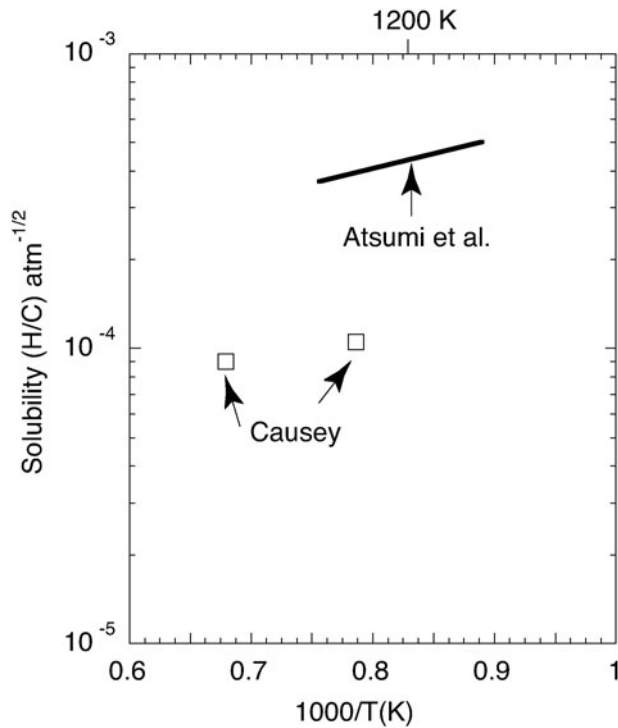


Fig. 6. Effective solubility of hydrogen in graphite grains. Data are from Causey<sup>62</sup> and Atsumi et al.,<sup>63</sup> both contained in Ref. 4.

### III.B. Carbon Erosion: Laboratory Studies

#### III.B.1. Low-Energy Tritium Ion Erosion of Graphite

An extensive database exists for the chemical erosion of graphite by sub-eV hydrogen atoms and energetic hydrogen ions in the energy range 100 to 3000 eV, e.g., Refs. 48 and 49. The chemical erosion yields due to sub-eV H atoms are typically two to three orders of magnitude lower than those for ions with energy  $>100$  eV. The reaction rates depend on temperature—with a maximum occurring at  $\sim 500$  to  $800$  K, depending on energy and flux density. The reaction products produced by the sub-eV atoms are dominated by heavy hydrocarbons, whereas for energetic ions methane dominates.<sup>48,49</sup> As the energy of the impacting ions/atoms decreases, the relative contribution of methane to the total hydrocarbon yield ( $\Sigma C_x H_y$ ) decreases; e.g., for 3-keV  $H^+$ , the  $CH_4$  comprises  $\sim 90\%$  of the total C yield, while at 50 eV, it drops to  $\sim 50\%$ , and for  $< 0.1$ -eV  $H^0$  atoms,  $CH_4$  contributes only  $\sim 5$  to  $10\%$  (Ref. 67).

Chemical erosion studies were also performed with CFCs. No differences were seen in either the total chemical erosion yield or the distribution of hydrocarbons between two orientations of the CFC and pyrolytic graphite.<sup>68</sup> On the other hand, significant reductions in  $H^+$ -induced chemical erosion have been observed for CFCs doped with boron and silicon.<sup>69</sup>

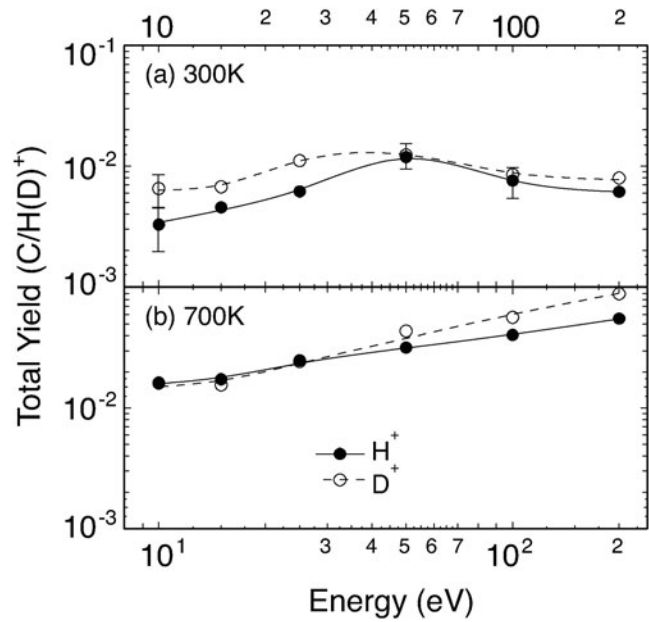


Fig. 7. Isotopic comparison of the total chemical erosion yield of graphite due to  $H^+$  and  $D^+$  impact at 300 and 700 K. (Data adapted from Ref. 70.)

Tokamak operation with low-temperature divertor plasmas has triggered laboratory studies of the chemical erosion of graphite with  $H^+$  ( $D^+$ ) energies of tens of eV—characteristic of the divertor plasma (e.g., Refs. 70, 71, and 72). Recently, this work was extended to include  $T^+$  ion irradiation.<sup>73</sup> As the incident  $H^+$  and  $D^+$  energy is reduced from 200 to 10 eV, the temperature dependence curves of the  $CH_4$  and the total C (sum of all C in the released hydrocarbons) yields broaden such that significant yields are seen even at 300 K (Refs. 48 and 70). This room temperature yield is energy dependent with a peak near 50 eV; see Fig. 7 (Ref. 70).

As a function of energy and temperature, the erosion yields are similar for both  $H^+$  and  $D^+$  irradiations, with the deuterium yields being up to two times higher under some energy-temperature conditions; see Fig. 7 (Ref. 70). Modeling of the experimental methane yields,<sup>74</sup> assuming a square-root mass dependence, generally fit all of the  $H^+$  and  $D^+$  yields within the experimental uncertainty of about  $\pm 50\%$ . Subsequent experiments using  $T^+$  ions have confirmed the absence of strong isotope dependence; see Fig. 8 (Ref. 73).

Combined irradiation of graphite with low-energy H (sub-eV to 100 eV) and energetic (above 300 eV) hydrogenic and nonhydrogenic ions leads to an enhancement of the chemical erosion yield compared to the sub-eV  $H^0$  or low-energy  $H^+$ -only cases. This is due to the additional energy deposition and associated lattice damage by the added energetic ions. Reference 50 has an overview of carbon erosion studied in dual-beam experiments.

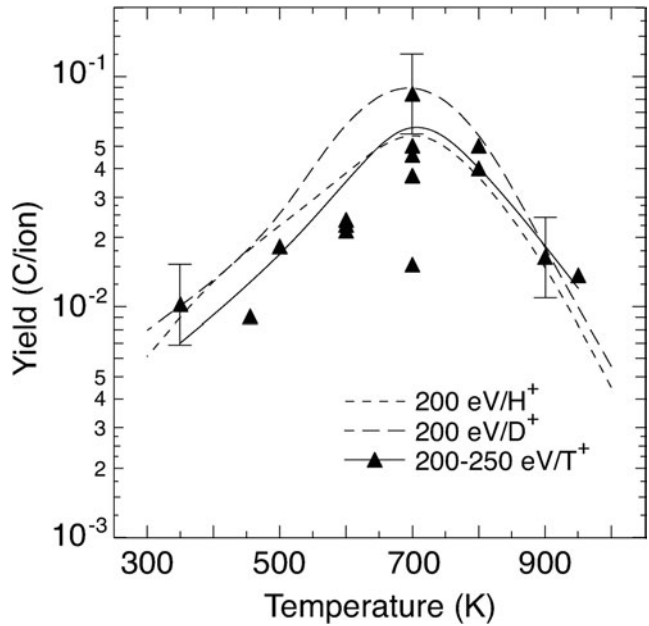


Fig. 8. Hydrocarbon yields as a function of graphite temperature for H<sup>+</sup>, D<sup>+</sup>, and T<sup>+</sup> impact on graphite. (H<sup>+</sup> and D<sup>+</sup> data are adapted from Refs. 70 and 75, and T<sup>+</sup> data are adapted from Refs. 73 and 75.) Lines are drawn to guide the eye.

### III.B.2. Hydrogen Isotope Effects on the Chemical Erosion of Carbon

The topic of isotopic effect on the chemical erosion of carbon has received considerable attention in the plasma-surface interaction community, and several experiments have been performed in a variety of devices, including ion beams, laboratory plasmas, and tokamaks. The measurement techniques used include mass loss, mass spectroscopy, and optical spectroscopy; see Ref. 75 for related references and a recent overview of these results. The D-yield/H-yield ratios ( $Y_{D^+}/Y_{H^+}$ ) obtained in these experiments at room temperature and  $T_{max}$ , plotted as a function of ion energy, are presented in Fig. 9. For all temperatures some isotopic effect for H<sup>+</sup> and D<sup>+</sup> is evident, with the deuterium yield being larger.<sup>75</sup> Typically, the observed  $Y_{D^+}/Y_{H^+}$  ratio lies between 1 and 2. (The notably higher yield ratios of Balden and Roth<sup>76</sup> remain unresolved.) This is fully consistent with the square root of mass dependence proposed by Mech et al.,<sup>74</sup> which implies that the erosion due to tritium would not be significantly larger than for deuterium, consistent with the tritium yields measured by Macaulay-Newcombe et al.<sup>73</sup> This is also consistent with the dependence of radiation damage on hydrogen ion isotope mass.<sup>77</sup> At energies much higher than the

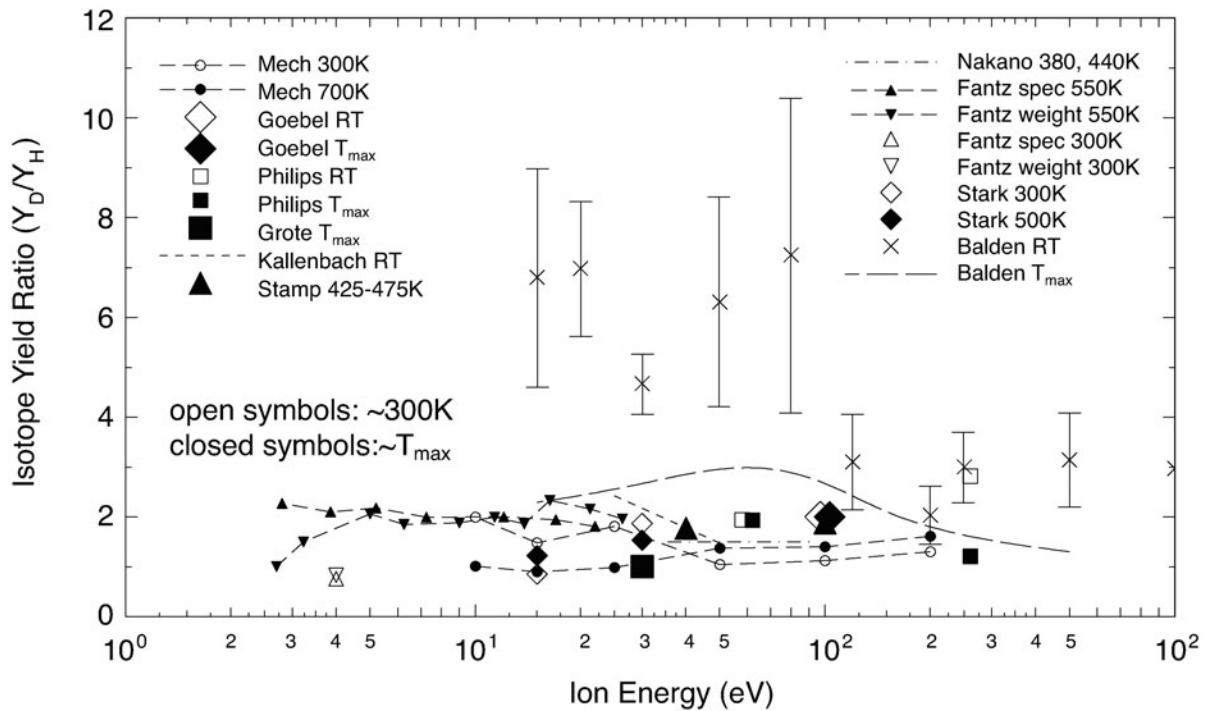


Fig. 9. Summary of the isotopic ratios of chemical erosion of carbon as determined in the various studies reported in Ref. 75 (data are adapted from Ref. 75).

threshold energy, the radiation damage increases roughly with the square root of mass.<sup>77</sup>

At low temperatures and low ion energies, molecular dynamics calculations indicate that a kinetic bond-breaking process will lead to the emission of hydrocarbon radicals from hydrogenated carbon surfaces, e.g., Refs. 71 and 78. At room temperature the calculated erosion yield ratios for the three isotopes appear to vary linearly with mass for incident ion energies below  $\sim 25$  eV and as the square root of mass for energies above  $\sim 25$  eV (Refs. 71 and 72). By gradually lowering the incident ion energy in the molecular dynamics calculations, a threshold energy was found; no carbon sputtering was seen at ion energies below  $\sim 1.0$  eV for any of the three isotopes H, D, T (Ref. 71). This is consistent with the modeling considerations of Hopf et al. where a threshold energy in the range of C-C bond energies in organic molecules (several eV) is suggested.<sup>79</sup> At energies close to the threshold for these kinetic effects, stronger isotopic differences might be expected if the threshold energy differs for different isotopes. An experimental verification of this hypothesis, however, is hampered by the lack of sufficiently high-flux ion sources with energies below 10 eV (Ref. 79).

### III.B.3. Laboratory Studies of Chemical Erosion of DIII-D Tokamak Tiles

This study was triggered by some unexplainable trends in spectroscopic observations of CD bands in DIII-D over an 8-yr period. The laboratory experiments were undertaken with the objective to assess whether the observed effect was due to changes in the chemical reactivity of the graphite caused by extensive plasma exposure and periodic boronizations.

Spectroscopic analysis of the DIII-D plasma has shown that the brightness of the CD emission band in the lower divertor has decreased by an order of magnitude over the course of 8 yr of plasma discharges (approximately 23 000 plasma shots).<sup>80</sup> Over this time period the  $B_{CD}/B_{CII}$  ratio has also decreased by a factor of 4. Both of these observations imply that the role of chemical erosion as a carbon source has been progressively reduced over the 8-yr period. A possible implication is that the carbon tiles in the lower divertor have undergone some surface modification, resulting in a reduced chemical reactivity caused by the routine boronizations in DIII-D or some sort of plasma conditioning of the tiles.<sup>80</sup>

Using a mass-analyzed low-energy  $D^+$  ion beam, controlled laboratory measurements of the chemical erosion yield were made on DIII-D divertor tile specimens from the inner and outer strike-point positions.<sup>81</sup> The measured yields are very similar to the yields obtained with pyrolytic graphite and virgin DIII-D tile specimens, showing no evidence of reduced chemical reactivity due to tile surface modification during prolonged DIII-D

plasma exposure—ruling out any plasma conditioning effect. The similar chemical erosion yield of pyrolytic graphite and the DIII-D virgin specimen further implies that the DIII-D divertor tiles have not experienced any significant changes in their physical properties due to surface preparation prior to installation in the divertor.<sup>81</sup> Therefore, at this time the observed trends in the spectroscopic observations of CD bands in DIII-D remain unexplained.

## III.C. Carbon Erosion: Tokamak Experience

### III.C.1. Carbon Erosion and Deposition in JET

In JET the characteristic pattern of erosion and re-deposition of plasma impurities has been strongly asymmetric for operations with every configuration of the divertor since it was installed in 1994 (Refs. 82 through 88). For example, Fig. 10 shows the deposition on a poloidal set of divertor tiles during the period 1999–2001, as measured by a micrometer.<sup>88</sup> The tile numbers (1 through 8) and the numbering of the measurement

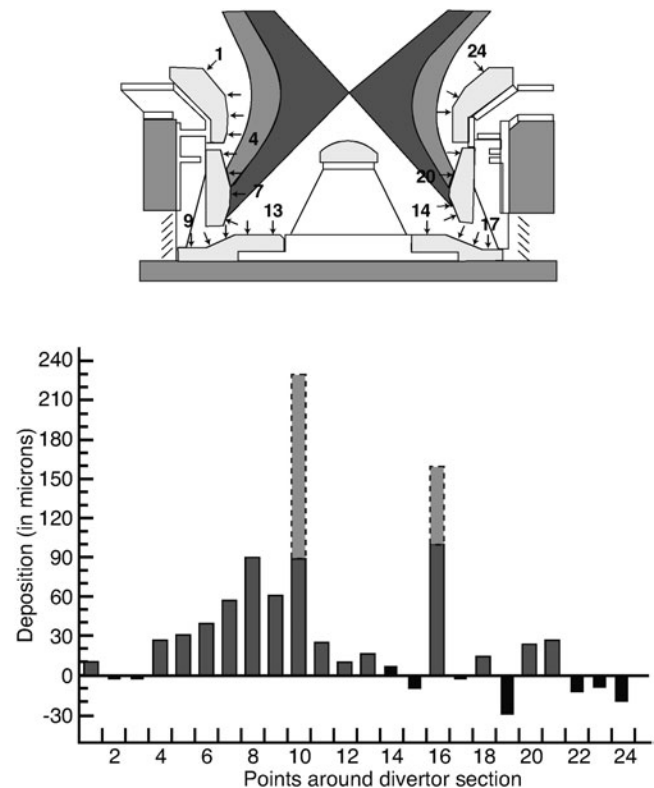


Fig. 10. Thickness of codeposited layer on a poloidal set of divertor tiles during the period 1999–2001 (measured by micrometer) (from Ref. 88). Gray bars denote the decrease in apparent thickness during many repeat measurements. The tile numbers (1 through 8) and the numbering of the measurement points (1 through 24) are shown in the upper part of the figure.

points (1 through 24) are shown in the upper part of Fig. 10. The deposit thickness on the inner divertor wall (tiles 1 and 3) increases toward the bottom, reaching a maximum of  $\sim 90 \mu\text{m}$ . There are even thicker deposits ( $\sim 200 \mu\text{m}$ ) on the small section of the floor that can be accessed by the plasma both at the inner (point 10) and outer (point 16) divertor legs. These are powdery in nature, hence the range of micrometer values at these points. Only small amounts of erosion/deposition are found elsewhere in the outer divertor (of the order of the accuracy of the measurement, which is  $\pm 10 \mu\text{m}$ ).

There is clearly more deposition in the divertor than erosion; so, much of the deposited material must come from the main chamber. Furthermore, in 1995 JET operated for a few months with a beryllium divertor, and carbon was deposited at the inner divertor, so it was obvious then that the main chamber contributed to the deposition. The inner wall cladding was shown to be one source,<sup>87</sup> and more recent measurements have shown that the outer poloidal limiters are also net erosion zones.<sup>85</sup> Other areas of the main chamber may also be net erosion zones. Under normal field conditions (grad B $\downarrow$ ), plasma impurities (on average 8% Be,  $\sim 1\%$  Ni plus other metallic impurities, balance carbon) erode from the main chamber drift around the scrape-off layer (SOL) and deposit where this intersects the inner divertor. However, carbon is released by chemical erosion from these deposits at the inner divertor, leaving a Be-rich film, and migrates in the plasma to the limiting accessible point at the inner corner of the divertor (point 10 in Fig. 10) (Refs. 86 and 88). Impurities are ejected into the shadowed region at the inner corner of the JET divertor to form films of  $\sim 100\text{-}\mu\text{m}$  thickness when power is applied to the neighborhood of point 10. This two-step process has been developed to explain results from a quartz microbalance (QMB) installed at the inner divertor for the MkIISRP campaign (2001–2004) (Ref. 89). The QMB has shown that most of the flux to the shadowed region occurs only when power is applied to the neighborhood of point 10, and there is little flux when the strike point is up on the inner divertor wall. The overall deposition at the inner divertor during the JET MkIIGB campaign (1999–2001) has been estimated at  $\sim 500 \text{ g}$  (predominantly carbon, plus beryllium and small amounts of other impurities), or  $\sim 20 \text{ mg/s}$  of divertor operation.<sup>90</sup>

During the 2001–2004 JET campaign, there was a 4-week period of operation with reversed magnetic field (grad B $\uparrow$ ). Under these conditions, plasma conditions (e.g., temperatures, densities, sputtered impurities) are more equitable in the two divertor legs, and infrared camera measurements show that a deposited film starts to grow on tile 7 (Ref. 86). Postmortem analysis after the campaign revealed that for the first time in a JET divertor, significant deposition (tens of microns) was also found in the shadowed region at the outer corner of the divertor.

### III.C.2. Carbon Erosion and Deposition in ASDEX-Upgrade

Net carbon erosion is observed over a large fraction of the ASDEX-Upgrade main chamber, especially at the inner heat shield<sup>91,92</sup> and the ion cyclotron resonant heating and auxiliary limiters at the low field side.<sup>93</sup> Large carbon influxes were still observed from the inner heat shield even after coating with tungsten,<sup>92</sup> indicating that this is an important carbon recycling area.<sup>94</sup> In the divertor, the outer baffle<sup>95,96</sup> and the outer strike point are net carbon erosion areas with a maximum campaign-averaged carbon erosion rate of  $>1 \text{ nm/s}$  at the strike point.<sup>96</sup> Eroded C, B (originating from boronizations), and metals (W, Fe, Cu, etc.) are redeposited mainly in the inner divertor.<sup>95</sup> The thickest layers, observed at the inner strike point, have a growth rate of  $\sim 2 \text{ nm/s}$ . Only a small deposition area is observed in the outer divertor in the lower corner, where the strike point is not positioned. Most boron and some fraction of the deposited carbon in the inner divertor originate from the main chamber. There is, however, some indication that carbon is transported from the outer divertor to the main chamber<sup>97</sup> and finally to the inner divertor.

Carbon is observed to migrate to remote areas without direct plasma contact, such as the roof baffle tiles just opposite the strike points,<sup>95</sup> all areas below the roof baffle,<sup>98,99</sup> and gaps between tiles<sup>100</sup>—forming soft deuterium-rich layers. The thickest layers are observed in areas with direct line of sight to the strike points, where hydrocarbon layers are mainly formed by particles with near-unity surface-loss probabilities.<sup>99</sup> Hydrocarbon species with lower surface loss probabilities (0.2 to 0.9) are also present, but because these particles are able to survive several wall collisions, they are responsible for layer growth in areas without direct line of sight to the plasma. Particles with very low surface loss probabilities  $<10^{-3}$  form thin layers ( $<1 \text{ nm}$  per campaign) in the pump ducts.<sup>98</sup> Re-erosion of redeposited layers in remote areas is observed during some discharges using QMBs (Ref. 101). This re-erosion is probably due to etching by low-energy or thermal atomic hydrogen. The re-erosion is temperature dependent and increases strongly with increasing temperature from 300 to 473 K (Ref. 99). The layer growth in remote areas is determined by the temperature-dependent balance between the influx of carbon atoms and hydrocarbon radicals, and etching by atomic hydrogen.

### III.C.3. Carbon Erosion and Deposition in NSTX

Hydrogen isotopes can be absorbed by plasma-facing materials during a tokamak discharge and released following the discharge, a process known as dynamic retention. Hydrogen can also be codeposited with eroded boron, beryllium, or carbon, and the layer growth results in a continuous increase of the in-vessel hydrogen

isotope inventory.<sup>102–104</sup> These processes have traditionally been studied by measurements of the global particle balance of gas fueling and exhaust (with time resolution but no spatial information)<sup>45,105</sup> and by tile surface analysis (spatial resolution but no time information).<sup>106</sup> QMBs can also be used to study hydrogenic retention and have the advantage of both a well-defined spatial location and time resolution.

The National Spherical Torus Experiment (NSTX) is aimed at exploring the physics of high beta and high confinement in a low aspect ratio device.<sup>107</sup> QMBs have been used to investigate the time dependence of deposition and dynamic retention in shadowed areas. Two QMBs were installed at a location 0.77 m outside the last closed flux surface to assess the deposition to be expected on a typical diagnostic window or mirror.<sup>108</sup> Ex situ analysis showed deposits of carbon, oxygen, and deuterium. The QMB facing away from the plasma recorded deposition of lower sticking probability molecules at 10% of the rate of the plasma-facing one. Time-resolved measurements over 497 discharges recorded  $29.2 \mu\text{g}/\text{cm}^2$  of deposition on the plasma-facing QMB; however, surprisingly, a total of  $15.9 \mu\text{g}/\text{cm}^2$  of material loss occurred in steps coincident with seven discharges presumably due to peeling or detachment of deposited layers from the crystal. Monte Carlo modeling of quiescent plasmas showed negligible direct deposition at the QMB location suggesting that transient processes such as edge-localized modes (ELMs), disruptions, and plasma start-up/shutdown are likely to dominate the deposition.<sup>108</sup>

Subsequently the QMBs were positioned in 7-cm-wide slots in the upper and lower outer divertor, 7 cm back from the tile surface.<sup>109</sup> The QMBs showed transient excursions at the occurrence of a discharge; Fig. 11 shows the first four discharges of May 10, 2005. The most striking feature at this location is a large stepup in mass with the first discharge of the day that relaxed to a higher level. Such a large stepup in layer thickness is universally observed on the first discharge of the day whatever its plasma parameters. The next three discharges had similar plasma parameters [lower single null, plasma current,  $I_p \approx 900$  kA, 4 MW neutral beam injection (NBI), peak electron temperature,  $T_e \approx 1$  keV, maximum line electron density  $N_{el} \approx 6 \times 10^{15}/\text{cm}^2$ ] but showed only a transient rise that decayed back to the prior level without a significant longer-term change in mass. This pattern cannot be explained by codeposition but is consistent with dynamic retention—that is mass gain through transient uptake of deuterium from the plasma followed by outgassing. Long-term QMB measurements show net erosion and deposition to be small at the QMB locations.

#### III.C.4. Carbon Deposition and Hydrogen Isotope Retention in JT-60U

More than half of the high-energy tritons produced in D-D reactions in JT60-U are directly implanted deep

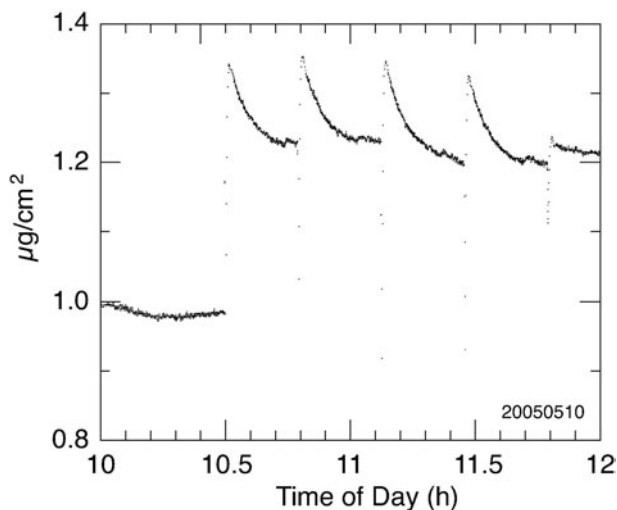


Fig. 11. Change in mass recorded by the NSTX Bay H bottom QMB on the first four discharges of May 10, 2005, showing the large stepup on the first shot. The y-axis zero is arbitrary (from Ref. 109).

into the tiles. These are not removed by isotopic exchange and/or thermal diffusion (with the exception of tritons implanted within  $\sim 1 \mu\text{m}$ ). The remaining tritons are thermalized in the plasma. Most of these impinge on the plasma-facing surfaces and are either retained, reflected and recycled, or evacuated. Tritons in the top surface layers can be completely removed by isotope exchange during subsequent D and H discharges. Nevertheless, some of the thermalized tritium is retained in redeposited carbon layers in shadowed areas and tile gaps that are not exposed to the plasma<sup>110</sup>; see Sec. III.D.5.

H and D as operating gases<sup>111,112</sup> behave similarly and are incorporated (retained) in the redeposited carbon layers.<sup>113</sup> Carbon deposition profiles in the divertor region show strong inboard/outboard asymmetry as observed in most divertor tokamaks<sup>114</sup>—thick redeposited layers on the inner tiles and eroded areas on the outer tiles. No significant carbon deposition was observed on plasma shadowed areas except on the bottom side of the outer dome wing (see Sec. III.D.5, Fig. 18). The carbon deposition rate in the divertor region is estimated to be  $\sim 9 \times 10^{20}$  atoms/s normalized for NBI duration during the 1997–2002 campaigns. Since  $\sim 40\%$  of the net deposition on the divertor was attributed to the erosion of the first wall, the net erosion of the first wall is  $\sim 220$  kg/yr.

The (H+D)/C ratio was uniformly  $\sim 0.03$  in the redeposited layers on the inner divertor tiles<sup>113</sup> except for a few microns of the top surface where it was  $\sim 0.05$  (Ref. 115). Surface D within a few microns was mostly replaced by H during subsequent H discharges used for tritium removal, indicating possible T removal by D discharges. Rather high D retention was observed on the

outer dome wing probably due to high-energy implantation of deuterons originating from NBI. Little deposition and debris were observed in remote areas, even in the NBI ducts and cryopanel.<sup>116</sup> The retained hydrogen comprises (a) dynamic retention on the plasma-facing surfaces that could saturate during one discharge and (b) static retention on plasma shadowed surfaces that would accumulate continuously.<sup>117</sup> The relatively low deuterium retention seen in JT-60U is attributed to operation at 573 K, which leads to surface temperatures well above 1000 K (Ref. 118) at the redeposited layers on the inner divertor.<sup>119</sup>

A newly developed tritium imaging plate technique<sup>120</sup> was used to obtain detailed tritium distribution on the divertor tiles of JET and JT-60U. In shadowed areas or tile gaps in the divertor, the deposition was quite inhomogeneous; thicker layers were observed in the line of sight of the strike points, directly accessible by the eroded carbon/hydrocarbon neutrals and radicals. The tritium content in such layers was higher than that in the layers formed on the plasma-facing surfaces because the temperature of the shadowed areas remained low during discharges.

### III.C.5. Transport and Breakup Processes of Hydrocarbons in the DIII-D Edge Plasma

Injection of  $^{13}\text{CH}_4$  into tokamaks has been used in the past as a tool for monitoring the deposition pattern for locally produced impurities. Such experiments have previously been carried out on TEXTOR (Refs. 121 and 122), JET (Ref. 123), JT-60U (Ref. 124), and ASDEX-Upgrade (Ref. 125), using single or multiple injection locations. Several experiments have also been carried out in DIII-D, with the objective of improving our understanding of hydrocarbon transport and various breakup reactions in the edge plasma of a tokamak. These processes have direct impact on C redeposition and associated codeposit formation.

In the DIII-D experiment,  $^{13}\text{CH}_4$  was injected from a toroidally symmetric source into the crown (top) of lower single-null plasmas. In the first experiment of this set, low-density L-mode plasmas were used,<sup>126,127</sup> while in the second, partially detached, ELMy H-mode discharges were used.<sup>128</sup> In the L-mode experiments, the largest concentration of  $^{13}\text{C}$  was observed on the inner divertor tiles,<sup>127</sup> while in the H-mode case, an approximately equal amount of deposition was also observed in the private flux zone between the divertor strike points. Modeling indicates that the deposition is strongly linked to parallel transport in the SOL (Ref. 129).

The second set of experiments involved the local injection of methane into the plasma at the outer divertor strike point, in order to simulate the release of hydrocarbons due to chemical sputtering.<sup>130</sup> These experiments involved the use of a self-contained gas injection system, the porous plug injector (PPI), capable of injecting small

quantities of gas into the lower divertor of DIII-D. A key feature of the probe is the carbon plate through which gas is injected. This plate has approximately 1000 small holes over an area  $\sim 3$  cm in diameter, such that the holes comprise  $< 10\%$  of the surface area. This configuration allows a distributed injection of gas so as to minimize the disturbance to the plasma, while still producing large spectroscopic signals. This approach also better reproduces the immediate environment experienced by a hydrocarbon molecule released by chemical sputtering—the molecules are released from an essentially continuous carbon surface. The primary goal of the PPI is to derive photon efficiencies for molecular and atomic species resulting from the breakup and ionization of hydrocarbons released from the divertor surface. In the initial experiment, gas flow was approximately ten times that due to intrinsic chemical erosion, which may have caused local disturbances to the plasma. Follow-up experiments, with gas flow reduced to be approximately equal to that of intrinsic chemical erosion rates and improved diagnostics, were performed in 2007, leading to more precise values for photon efficiencies and estimates for the relative importance of physical and chemical sputtering of carbon.<sup>131</sup>

### III.D. Tritium Retention in Carbon Codeposits

#### III.D.1. Dependence of Deuterium Retention on Graphite Structure

##### *Total deuterium retention*

Retention of hydrogen isotopes at high ion fluences depends on material structure. In single crystal and dense pyrolytic graphite, implanted hydrogen does not diffuse from the implanted region, and after reaching a local concentration of  $\text{D}/\text{C} \approx 0.4$  at 300 K (lower at higher temperatures), further implanted hydrogen is reemitted.<sup>5,132–134</sup> In fine-grain graphite (typical density of  $\sim 1850$  kg/m<sup>3</sup>), no saturation occurs, and retention slowly increases with incident ion fluence.<sup>134,135</sup> The same tendency, but much more pronounced, is found in doped graphites<sup>136</sup> and CFCs (Ref. 56). Comparisons of the  $\text{D}^+$  fluence dependence of different graphite structures, spanning monocrystal, fine-grain, and doped graphites, irradiated at 300 K are shown in Fig. 12; the relatively higher slopes for the doped graphites (designated by CKC-dopant) are attributed more to structure than to the effect of the dopants.<sup>136,137</sup> Recent measurements for composites NB31 and N11 are shown in Fig. 13 (Ref. 56). D retention in  $\text{D}^+$ -irradiated NB31, measured by nuclear reaction analysis (NRA), shows a quasi-square-root dependence on incident fluence at 323 and 473 K, while at 523 K the retention level is a factor of  $\sim 3$  lower. Samples of N11 exposed to a plasma in PISCES-A at 473 K (analyzed by NRA) also showed no

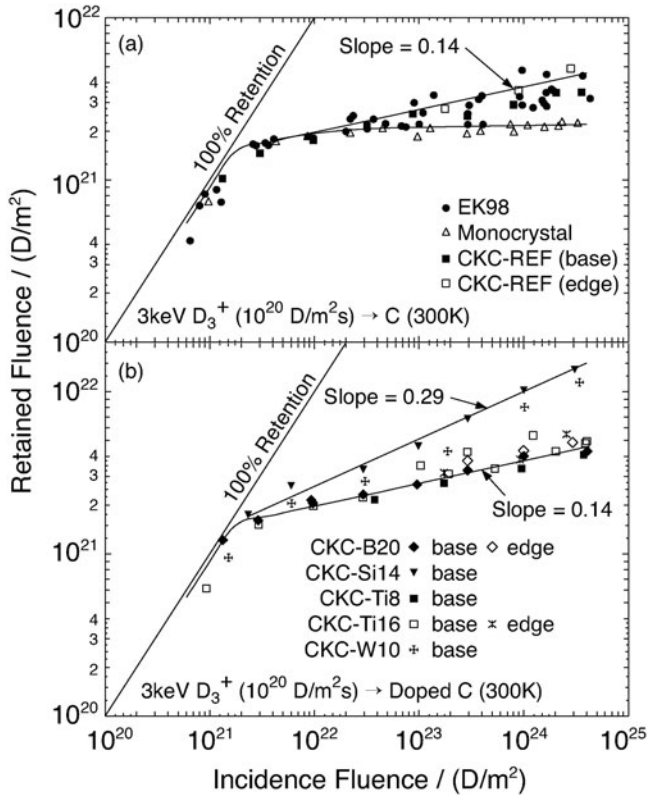


Fig. 12. Comparisons of D retention in different graphite structures as a function of D<sup>+</sup> fluence (from Ref. 136).

saturation even at a fluence of  $2 \times 10^{26}$  D/m<sup>2</sup>; somewhat lower retention was seen at 673 K. By comparison, a saturation trend is observed in HPG pyrolytic graphite.<sup>138</sup>

*Deuterium depth profiles*

A deep penetration of deuterium into the CF222 CFC (up to 2 to 3 mm) was reported after its exposure to plasmas in PISCES-A (Ref. 139). Tritium depth profiles in 2D CFC divertor tiles retrieved from JET have revealed that a large fraction (up to 61%) of the retained tritium had diffused deep into the bulk (up to 20 mm); by comparison, only a few percent was found in the 4D CFC tiles from TFTR (Refs. 54, 140, and 141).<sup>a</sup>

In NB31 irradiated at 323 K with 200-eV D<sup>+</sup>, the D depth profile is characterized by a near-surface maximum and a long tail in the bulk, increasing with ion fluence. Depth profiles at 323 K show that saturation occurs only within the near-surface layer equivalent to the ion range. The near-surface maximum widens as the fluence increases. For fluences above  $5 \times 10^{24}$  D/m<sup>2</sup>, the tail extends beyond 14 μm with D concentrations of

<sup>a</sup>2D, 4D, etc., refer to the dimensionality of the weave of the fibers.

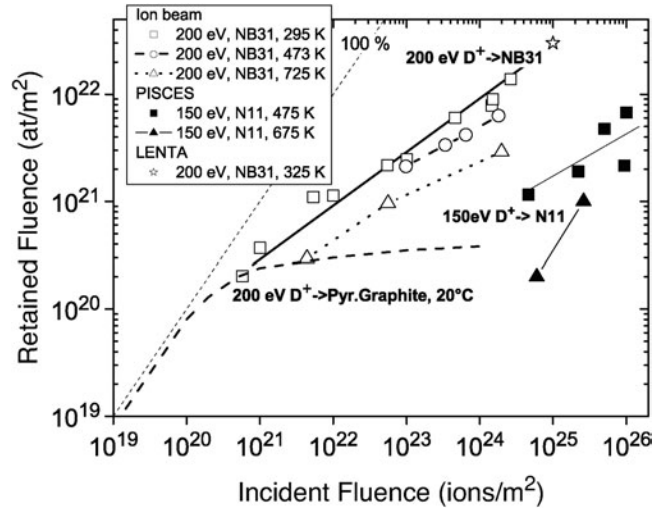


Fig. 13. Deuterium retention in CFC materials compared with pyrolytic graphite (from Ref. 56) as a function of incident D<sup>+</sup> ion fluence. Additionally, data for LENTA are given (from Ref. 144).

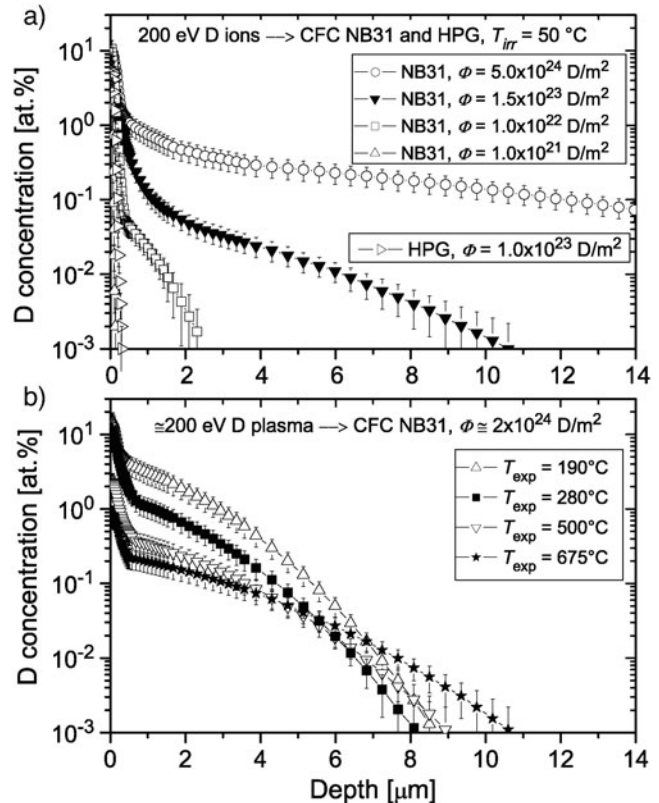


Fig. 14. Depth profiles of D in CFC NB31 and pyrolytic graphite HPG irradiated with (a) various fluences of 200-eV D<sup>+</sup> at 300 K and (b) D magnetron plasma to the fluence of  $2 \times 10^{24}$  D/m<sup>2</sup> at various temperatures. Retention in HPG pyrolytic graphite is shown for comparison (from Ref. 138).

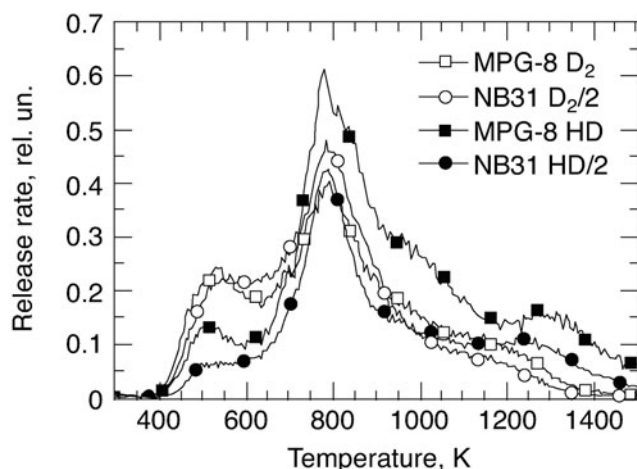


Fig. 15. Thermal desorption of  $D_2$  and HD from fine-grain graphite MPG-8 and CFC NB31 after irradiation in LENTA by 200-eV D ions to the fluence of  $10^{25} D/m^2$  at 323 K. Data for NB31 are divided by a factor of 2 to compare with MPG-8 (from Ref. 144).

$\sim 10^{-1}$  at.%; see Fig. 14a. It is evident that the structure of the CFC NB31 allows deuterium to penetrate into the bulk even at room temperature while no diffusion tail is observed in HPG (Refs. 134 and 142). This could have implications for long-pulse/high-fluence machines such as ITER and probably plays a role in the retention rate observed in long pulses in Tore Supra.<sup>143</sup> Depth profiles for different temperatures are shown in Fig. 14b.

#### Thermal desorption spectra

TDS measurements for CFC NB31 and powder graphite MPG-8 exposed to various plasmas demonstrated a variety of narrow peaks in the range of 500 to 1200 K, which are combined in three broad peaks as shown in Fig. 15. Experiments with ion implantation and saturation from  $D_2$  gas exposure gave similar peak positions but different relative peak intensities, connected with the production of radiation defects and different accessibility of the trapping sites.<sup>144</sup> The positions of the main groups of peaks were the same for powder graphite and the NB31 CFC although the CFC traps twice as much deuterium. The release of  $D_2$  molecules often correlates with the release of  $H_2$ , HD,  $CD_4$ , and HDO after plasma exposure. This suggests that release starts from detrapping of D and H atoms, followed by their fast migration to the surface, recombination with other complexes, and release of various H- and D-containing molecules.

#### III.D.2. Deuterium and Tritium Retention in Codeposits Observed in JET and TFTR

Gas retention in JET is regularly inferred from post-mortem analysis of a relatively small sample of tiles

removed during each shutdown. This value, however, will be lower than the real figure for a campaign of plasma discharges because it also includes the effects of periods of glow discharge cleaning (GDC) and of exposing the vessel and the samples to air. Comparisons between gas balance and postmortem analysis when JET was a limiter machine indicated a discrepancy of a factor of  $\sim 2$  (Refs. 145 and 146). Since the divertor was installed in JET in 1994, gas balance measurements have been difficult because of the simultaneous installation of a fully toroidal divertor cryopump. Deuterium retention values averaged over typically 1 week have been of the order of 8% but with a factor of 2 error bar.

During the deuterium-tritium experiment (DTE1) in JET in 1998, 40% of the 35 g tritium input was retained.<sup>43</sup> By running a campaign of cleanup discharges, the retained tritium was reduced to 17% of the input. The removable fraction may have been in the dynamic wall inventory, which can isotope exchange with the fueling gas, while most of the remaining 17% is assumed to be in codeposited films that are not affected by plasma discharges. A further 6% was released to air during the subsequent JET shutdown. Postmortem analyses following the DTE1 campaign revealed that the codeposited material was located mainly at the inner corner of the divertor.<sup>146</sup> Thick carbon-based films containing H isotopes with H/C in the range 0.7 to 1.0 were found in regions shadowed from the plasma such as at the inner louvers, where the deposition was so heavy that the deposits had spalled off to form flakes. Analysis of the flakes showed that the D:T ratio was similar to the relative fueling amounts during the entire campaign. The H-isotope content of deposits elsewhere in the vessel was lower as a result of plasma interaction. In subsequent campaigns, deposits at the inner divertor corner have continued to dominate, with comparable amounts of carbon deposition (and hence H-isotope trapping).<sup>90</sup> Following a trace tritium campaign in 2003 (using 0.38 g tritium in total), the tritium content of selected components removed from JET was used to estimate the tritium retention, which was found to be  $\sim 15\%$  of the input. The most recent gas balance measurements show the D retention in JET to be  $\sim 11\%$  (averaged over L-mode, type III ELMy H-mode and type I ELMy H-mode discharges).<sup>147</sup> The T retention rate in the 2003 experiment was of similar order (given the inaccuracies of the measurements), but it is possible for T to be retained at a greater rate than D because of isotope exchange.

TFTR plasmas had a circular cross section with major radius typically 2.5 m and minor radius 0.9 m. The plasma boundary was defined by an inner toroidal limiter composed of graphite tiles and carbon composite tiles in high heat flux regions. Analysis of in-vessel components exposed during the deuterium phase of TFTR showed the main mechanism for retention was codeposition. The ratio of deuterium retained in the vacuum vessel to the total used in neutral beam fueling was found

to be  $44\% \pm 17\%$ . Of this, 19% was on the plasma-facing surface of the bumper limiter tiles, 7% on the tile sides, and 18% on the vacuum vessel wall. During 3.5 yr of TFTR D-T operations, 100 g of tritium was processed, and 5 g of tritium was supplied to the plasma by NBI and direct gas puffs. The tritium inventory in tiles and coupons removed from the vessel was compared with estimates of tritium retention obtained through modeling of the carbon erosion/deposition in selected discharges.<sup>148</sup> The comparison showed that known erosion mechanisms and subsequent codeposition were sufficient to account for the order of magnitude of retention. The tritium input and exhaust were also carefully tracked. There were three periods of plasma operations interspersed with cleanup campaigns to remove tritium.<sup>104</sup> During the three run periods (excluding periods of active tritium removal),  $\sim 51\%$  of the tritium supplied to the plasma was retained in the vacuum vessel, a fraction similar to that found in earlier deuterium measurements. Active tritium removal by glow discharge and air ventilation was successful in removing substantial amounts of tritium between periods of plasma operations. At the end of April 1998, the long-term tritium retention was 16%. T retention was also extrapolated from measurements of tiles and coupons retrieved from TFTR. The T inventory was estimated to be 0.2 g T in the inner limiter, with the highest concentrations at the top and bottom of the limiter, and 0.36 g T on the outer wall. The total of 0.56 g T was consistent with the difference inventory measured by gas balance of 0.64 g (Ref. 104).

### III.D.3. Tritium Depth Profiles in Tiles Retrieved from JET and TFTR

Tritium depth profiles for tiles retrieved from JET and TFTR revealed a nonuniform surface distribution of tritium over the vessel,<sup>84,149</sup> and this was also confirmed by deuterium analysis.<sup>146</sup> In JET a substantial amount of tritium is retained in the divertor region in the form of flakes, and a significant part of the retained tritium is also trapped deep in the bulk of the tiles. Figure 16 shows typical tritium profiles in tiles IN3 and BN4 due to diffusion.<sup>84,141</sup> The diffusion profile can be fitted with an equation of the type

$$A_D = A_B + A_0 e^{(-kD)}, \quad (1)$$

where

$A_D$  = tritium activity measured (or calculated for the part lost during cuts)

$A_B$  = activity in the bulk of the tile

$D$  = depth (mm)

$k$  = constant having a dimension of inverse length ( $\text{mm}^{-1}$ ).

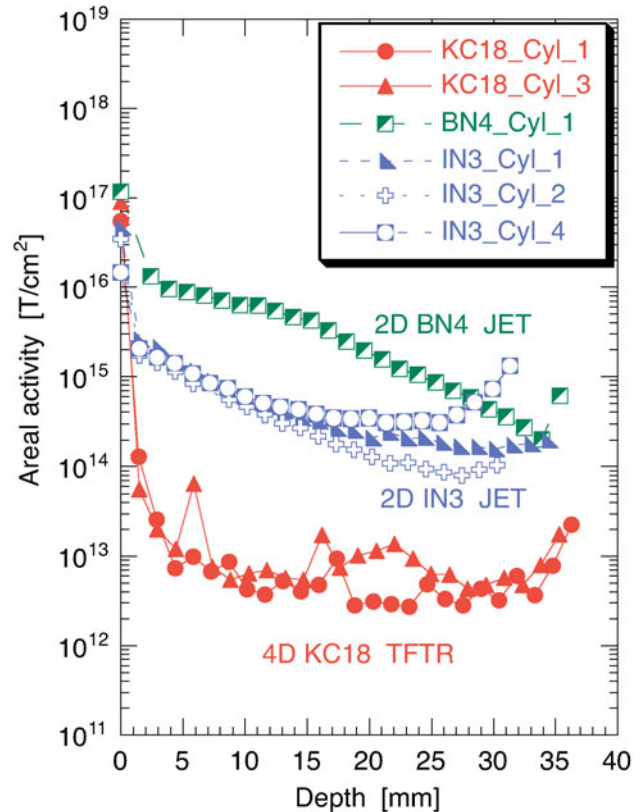


Fig. 16. Tritium depth profiles for the JET 2D divertor tiles IN3 and BN4, and the 4D TFTR tile KC18 (from Refs. 84 and 141).

The latter depends on temperature, tile material (graphite or CFC), and structure (2D, 3D, 4D, etc.) (see footnote a on p. 906). For the JET divertor tile IN3, this value is fairly constant,  $\sim 0.2 \text{ mm}^{-1}$ . The preexponential factor  $A_0$  represents the tritium activity on the surface of the tile, not including the tritium content of any deposited film on the surface. Typical values for  $A_B$ ,  $A_0$ , and  $k$  are given in Table I (Refs. 84 and 149). Table I also compares the activity found in the first millimeter of the plasma-exposed surface of the tile (first disk) with the tritium activity in the bulk of the tile calculated by the equation above.

As illustrated in Fig. 16, all cylinders exhibit almost the same surface activity ranging between  $10^{16}$  and  $10^{17} \text{ T/cm}^2$ . Another remarkable point is that the bulk activity of all cylinders sharply decreases after the first sample (1 mm below the plasma exposed surface) and seems to reach an almost constant value at  $\sim 3 \times 10^{14} \text{ T/cm}^3$  for the JET samples, while the bulk values for the TFTR samples are more than one order of magnitude lower. This comparison indicates that for similar tritium surface activity, the tritium inventory in the TFTR-4D CFC is much lower than in the JET-2D CFC. This could be attributed to a lower diffusion of small molecular species ( $Q_2$ ,  $Q = \text{H, D, or T}$ ) in 4D tiles along the weaves of the

TABLE I  
Tritium Fraction in the Bulk of Various Cylinders Retrieved from JET 2D CFC Divertor Tiles  
After the DTE1 Campaign and from TFTR 4D CFC Tiles\*

Tile/Cylinder (Cylinder Diameter: 0.78 cm)	Volume of the Cylinder (cm <sup>3</sup> )	Plasma Exposed Disk ( $A_1$ ) (T/disk)	Total Activity ( $A_{total}$ ) (T/cyl)	$A_B$ (T)	$A_0$ (T)	$K$ (mm <sup>-1</sup> )	Bulk Fraction Activity (%) <sup>a</sup>	Error (%)
IN3 cyl-1	1.85	$2.24 \times 10^{16}$	$3.59 \times 10^{16}$	$8.46 \times 10^{13}$	$1.65 \times 10^{15}$	0.21	37.6	5
IN3 cyl-2	1.60	$1.65 \times 10^{16}$	$2.57 \times 10^{16}$	$2.74 \times 10^{13}$	$1.03 \times 10^{15}$	0.16	35.8	6
IN3 cyl-4	1.55	$6.98 \times 10^{15}$	$2.12 \times 10^{16}$	$1.57 \times 10^{14}$	$1.16 \times 10^{15}$	0.21	67.1	4
BN4 cyl-1	1.70	$5.58 \times 10^{16}$	$1.43 \times 10^{17}$	—	—	—	61.0	12 <sup>b</sup>
KC18 cyl-1	1.79	$2.62 \times 10^{16}$	$2.65 \times 10^{16}$	$2.70 \times 10^{12}$	$3.70 \times 10^{14}$	1.27	1.1	—
KC18 cyl-2	0.68	$4.10 \times 10^{16}$	$4.13 \times 10^{16}$	—	—	—	0.7	—
KC18 cyl-3	1.73	$4.28 \times 10^{16}$	$4.31 \times 10^{16}$	$3.94 \times 10^{12}$	$9.21 \times 10^{13}$	0.95	0.7	—

\*References 84 and 149.

<sup>a</sup>Bulk activity is calculated as  $\{1 - (A_1/A_{total})\} \times 100$  where  $(A_1/A_{total})$  represents the fraction of the surface activity.

<sup>b</sup>The best fitting equation involves a double exponential expression taking into account front and rear side diffusion.

fibers. We may then expect even less T retention in the bulk of higher level CFCs (e.g., 7D or even 11D) (see footnote a on p. 906).

#### III.D.4. Deuterium Retention in Codeposits Observed in ASDEX-Upgrade

Deuterium-containing codeposited layers are observed predominantly in the inner divertor of ASDEX-Upgrade, where amorphous hydrocarbon layers with some additional boron and D/(B + C) in the range 0.2 to 0.4 are formed on all tiles.<sup>95</sup> Soft deuterium-rich layers with higher D/C ratio (0.4 to 1.0) are formed in remote areas without direct plasma contact at the roof baffle tiles just opposite the inner strike point and on areas below the roof baffle.<sup>98,99</sup> Also, very soft and deuterium-rich hydrocarbon layers with D/C from 1.3 to 1.7 were observed on the liquid nitrogen-cooled panels of the cryopumps.<sup>99</sup>

The amount of D trapped in different areas of ASDEX-Upgrade is summarized in Table II. Deuterium is mainly trapped in codeposited layers on inner divertor tiles, where 50 to 60% of the total D inventory is found. Some tiles showed a smaller D/(B + C) ratio of  $\sim 0.2$ , probably due to elevated temperatures. An upper value for the possible inventory is obtained from the amount of deposited B + C, assuming a ratio of D/(B + C) = 0.4; see Table II (Ref. 150). About 30% of the D inventory is found at roof baffle tiles in the divertor (mainly just opposite the inner divertor strike point) and on the structure below the roof baffle, and only  $\sim 10\%$  is found in other areas, such as the upper divertor tiles, side faces of main chamber limiters, and gaps between tiles in the main chamber. Migration of D to very remote areas, such as pump ducts, is negligible. The amount of retained D corresponds to 3 to 4% of the total deuterium input.<sup>151</sup>

TABLE II  
Amount of D Trapped in Codeposited Layers in Different Areas of ASDEX-U\*

Location	Amount of D (g)	Campaign Dates
Inner divertor tiles	1.15 (1.84)	2002–2003
Roof baffle tiles	0.16	2002–2003
Outer divertor tiles	0.14	2002–2003
Gaps between divertor tiles	0.12	2002–2003
Below roof baffle	0.46	2002–2003
Pump ducts	0.005	2001–2002
Upper divertor tiles	0.16	2003–2004
Gaps between inner heat shield tiles	0.07	2002–2003
Auxiliary limiters in main chamber	0.03	2005–2006
Total	2.30 (2.99)	2002–2003

\*Numbers in parentheses are obtained from the amounts of deposited B and C, assuming D/(B + C) = 0.4 (Ref. 150).

#### III.D.5. Hydrogen Isotope Retention and Carbon Deposition in Tokamak Tile Gaps

Carbon deposition profiles at tile sides (or tile gaps) are clearly correlated to hydrogen (H, D, T) retention, and the carbon deposition profiles are quite consistent with tritium retention profiles given by the tritium imaging plate technique.<sup>152</sup> Generally, carbon deposition decreases from the front side to the bottom side, and at least two decay components, one with an e-folding length of  $\sim 3$  mm and the other with  $> 10$  mm are distinguished as depicted in Fig. 17 (Ref. 152). The detailed deposition

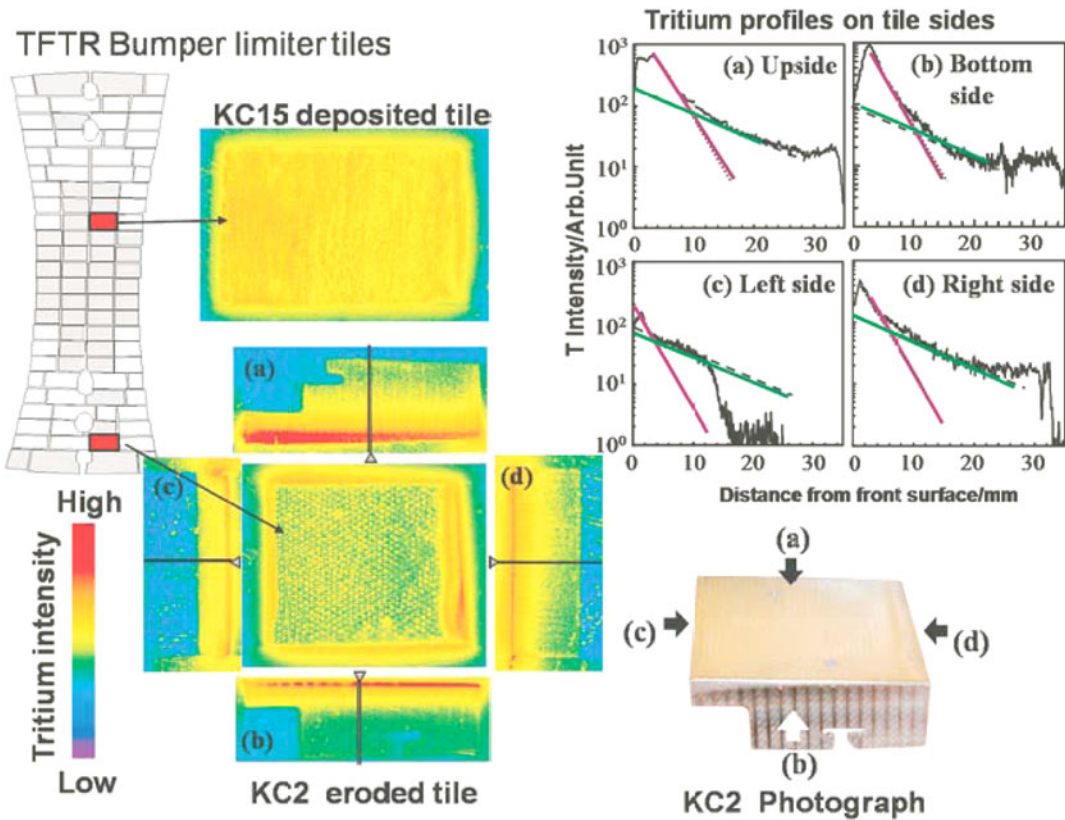


Fig. 17. Tritium profiles on two carbon tiles used as TFTR bumper limiters: eroded tile (KC15) and deposited tile (KC2) (from Ref. 152). Tritium distributions on tile sides of KC2 are also shown.

profiles are quite dependent on the location of tiles as well as different machines.

From the tritium intensity levels shown in Fig. 17 for two TFTR bumper limiter tiles, it is evident that the tritium intensity on all sides of the eroded tile (KC2) is higher than the front surface intensity, indicating the occurrence of local transport and prompt redeposition of carbon near the eroded area. Since the tritium intensity was nearly proportional to the tritium concentration in the surface layers as determined by combustion<sup>112</sup> and the tritium profiles were well correlated to carbon deposition profiles,<sup>112,153,154</sup> one can estimate the extent of carbon deposition in the tile gaps from tritium profiles. The side tritium profiles of tile KC2 show how carbon is penetrated and deposited in the gaps. Most of the carbon (and tritium) accumulated near the front (plasma-facing surface) and decreased exponentially toward the rear—with an e-folding length of  $\sim 3$  mm for all tiles.

At least two different decay lengths of carbon deposition in tile gaps were also observed in JT-60U (Ref. 154) (see Fig. 18), JET (Refs. 112, 154, and 110), and ASDEX Upgrade (Refs. 100 and 150). The mechanism leading to gap deposition involves two different processes. Firstly, carbon ions entering the gap get deposited within the

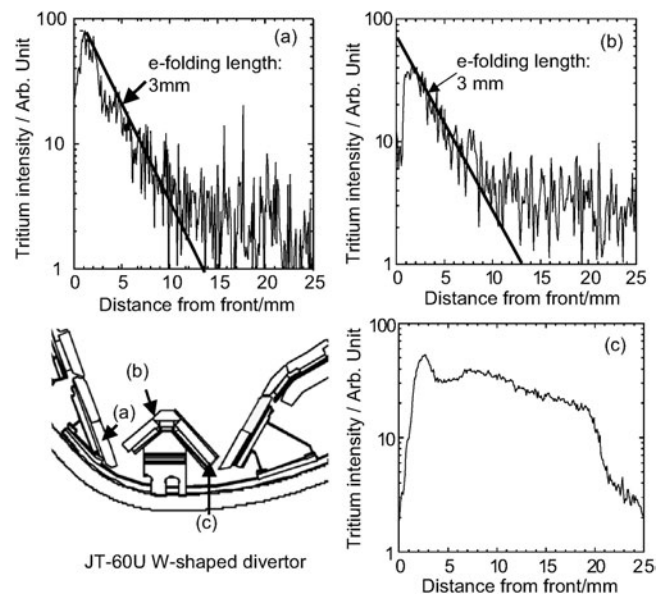


Fig. 18. Tritium profiles on the side surfaces of JT-60U divertor tiles (from Ref. 154): (a) toroidal side of inner divertor tile, (b) poloidal side of dome top tile, and (c) bottom side of outer dome wing tile.

radius of gyration, incorporating tritium as observed in the tile side profiles; hence, carbon deposition in gaps is larger for the tiles facing the magnetic field than for those in shadowed areas.<sup>99,114,119,150</sup> Secondly, transport deeper in the gaps is perpendicular to the magnetic field and is due to neutral particles. This may be neutral carbon atoms or neutral hydrocarbon radicals with low sticking coefficient.<sup>99,100</sup> This deep penetration is dependent on the tile location and tile gap width.<sup>155</sup> Recent simulations performed by Ohya et al.<sup>156</sup> and Inai and Ohaya<sup>157</sup> were able to confirm the short decay deposition due to ionization and gyration of incident carbon ions at the plasma-facing surface. The deeper penetration was successfully modeled by assuming neutral particles with low sticking coefficient, which are able to survive several wall collisions.<sup>100</sup> At elevated temperatures re-erosion by atomic hydrogen may play an important role.<sup>99</sup>

#### III.D.6. Hydrogen Isotope Retention in Tokamak Dust

Early studies of dust produced by a plasma disruption simulator found a retention level of  $6 \times 10^{19}$  D/g of carbon or D/C of  $1.2 \times 10^{-3}$  (Ref. 158). The D content in dust retrieved from TFTR mid-infrared instrument diagnostic windows<sup>159</sup> was measured to be D/C  $\approx 5.8 \times 10^{-3}$ , and the T/C ratio was 26 times lower, as expected from the T/D fueling ratio. Analysis of dust vacuumed from the TFTR vacuum vessel also showed a low D/C ratio of  $8.1 \times 10^{-3}$  and T/C of  $4.4 \times 10^{-4}$ . Baking of 0.24 g of flakes from TFTR codeposits at 773 K for 1 h released 0.72 Ci or 75  $\mu\text{g}$  of tritium, a T/C ratio of  $3 \times 10^{-4}$  (Ref. 160) broadly consistent with the dust results. Even this low amount of tritium was enough to cause the flakes to spontaneously levitate under the influence of a static electric field,<sup>161</sup> suggesting that in accident scenarios ambient static electric fields will facilitate the spread of tritiated dust. Ion beam analysis (IBA) of JET flakes showed a D/C ratio of 0.75 (Ref. 162), which is about two orders of magnitude higher than the TFTR deuterium content. This suggests that the low D/C ratios found in TFTR and in the disruption simulator dust were due to previous exposure to high temperatures.

The transport of dust particles in plasmas may play a significant role in the performance of next-step fusion devices. Highly mobile incandescent dust particles were observed in NSTX for the majority of the discharges using fast visible cameras.<sup>163</sup> Particles were most often born in the divertor region during events such as ELMs or disruptions. Particles born on the midplane were most often deflected by the plasma boundary and remained outside the SOL. The dynamics of the dust trajectories can be quite complex exhibiting a large variation in both speed (10 to 200 m/s) and direction. Particles may have constant velocities or exhibit various degrees of acceleration or deceleration. Abrupt reversals in direction are sometimes observed while some of the larger particles are seen to break apart during midflight. Three-

dimensional trajectories of the dust particles have been derived from measurements of dust trajectories taken simultaneously from two observation points with two fast cameras<sup>163</sup> and will be used to benchmark dust transport models.

Methods to measure the inventory of dust particles and to remove dust if it approaches safety limits is a high challenge for the radiological environment and scale of next-step burning plasma devices such as ITER. Diagnostics that could provide assurance that ITER is in compliance with its dust inventory limits are in their infancy.<sup>3</sup> A separate challenge is demonstrating techniques that could remove dust from the tokamak once the limits are approached. An electrostatic dust detector, based on fine grids of interlocking circuit traces, biased to 30 or 50 V, has been developed for the detection of dust on remote surfaces in air and vacuum environments.<sup>164,165</sup> The current flowing through the short circuit creates a voltage pulse, and the total number of pulses can be related to the mass of impinging dust. The response (counts/mg  $\cdot$  cm<sup>-2</sup>) is maximal for smaller particles.<sup>166</sup> The short-circuit events are transient as heating by the current pulse caused up to 90% of the particles to be ejected from the grid or vaporized.<sup>167</sup> This both resets the detector for subsequent dust particles and raises the possibility for using this device to transport dust and remove it from difficult-to-access locations in tokamaks. The contemporary development of microelectronic and flat screen technology offer new possibilities for routine electrostatic dust detection and transport with miniaturized hardware and without the need for dedicated intervention. A mosaic of electrostatic elements in a next-step tokamak could be potentially used for detecting conductive dust settling on remote surfaces and also ensure that these surfaces remain substantially dust free.

#### III.E. Carbon Summary and Conclusions

Carbon has been extensively used in most of the recent and current major tokamak fusion reactors for shielding the vacuum vessel from the plasma and has also been selected for use for the ITER divertor target plates, although the use of carbon in ITER's D-T phase is at the present uncertain. Key issues related to the use of carbon in tokamaks are carbon's erosion behavior and its capacity to trap hydrogen. Carbon erosion typically occurs in the main chamber of contemporary tokamaks. By contrast, more deposition than erosion occurs in the divertor, implying that much of the deposited material must come from the main chamber. Deposition in the divertor is asymmetric, with most of the deposits being on the inner divertor. Examples include thick codeposits in shadowed areas of the inner divertor of JET and ASDEX-Upgrade.

In ITER chemical erosion is expected to be dominant in the divertor where plasma temperatures are a few electron volts with corresponding H<sup>+</sup> energies of tens of

electron volts—below the threshold for physical sputtering. Eroded C (atoms/molecules/radicals) can get transported in the plasma edge until they intercept solid surfaces where redeposition, in conjunction with H isotopes, can result in the continuous growth of codeposited layers. (In ASDEX-Upgrade, there is some indication that carbon is transported from the outer divertor to the main chamber and finally to the inner divertor.) Thus, the codeposits serve as reservoirs for trapped tritium. During the D-T campaigns in both JET and TFTR, massive amounts of the injected fuel were retained by the carbon walls of the vessel (mostly in codeposits) leading to a retention fraction of 40 to 50%, and this was subsequently reduced in cleanup operations. The relatively lower D retention seen in JT-60U is attributed to operation at 573 K, which leads to temperatures above 1000 K on the surface of the inner divertor. By comparison, in the JET divertor, most of the deposition was on the horizontal divertor tiles (which were fixed to the water-cooled plates) and the louvers just in front of the cryopumps. Consequently, the JET divertor deposition areas were at temperatures much lower than the machine temperature.

Carbon deposition profiles observed in tile gaps of several tokamaks correlate well with hydrogenic retention profiles. Generally, most of the carbon (and tritium) accumulates near the front (plasma-facing surface) of the gap and decreases exponentially toward the bottom, with at least two e-folding lengths of  $\sim 3$  and 10 mm.

Dust produced in D-T burning tokamaks will contain tritium and thus will have tritium inventory and safety implications. The tritium content of the dust is expected to be high for dust formed by chemical synthesis or by flaking of codeposits but relatively low for dust produced in high-temperature off-normal events such as disruptions.

Laboratory experiments with ion beams and plasma devices have shown that hydrogen retention in carbon-based materials depends on material structure. In single crystal and pyrolytic graphite, implanted hydrogen gets trapped in the implantation zone until saturation is reached, after which further implanted hydrogen is re-emitted. In less dense forms of graphite, no saturation occurs, and retention slowly increases with increasing incident ion fluence, with some of the incident D diffusing more deeply into the material. The same tendency, but much more pronounced, is found in doped graphites and CFCs. Tritium depth profiles in 2D CFC divertor tiles retrieved from JET have revealed that a large fraction (up to  $\sim 60\%$ ) of the retained tritium had diffused deep into the bulk (to 35 mm); by comparison, only a few percent was found in the 4D CFC tiles from TFTR.

In conclusion, codeposits formed in D-T burning reactors with carbon PFCs can act as reservoirs for tritium retention, depending on the PFC temperature. Techniques for the periodic removal of T from codeposits are described in Sec. VI.

## IV. TUNGSTEN

Because of its favorable physical properties, such as low erosion yield and high melting temperature, tungsten is a candidate armor material for some parts of the ITER divertor and perhaps the whole first wall in future reactors. As a plasma-facing material, tungsten will be subjected to intense fluxes of energetic deuterium and tritium ions and neutrals. Implantation of these ions into W PFCs leads to concerns about tritium inventory after long-term plasma exposure. Most of the data on hydrogen isotope retention and recycling for tungsten generated before 2000 have been reviewed by Causey<sup>4</sup> and Causey and Venhaus.<sup>168</sup> In this section we present recent results on D retention in single crystal tungsten (SCW) and polycrystalline tungsten (PCW), exposed to D<sup>+</sup> ions and D plasmas (PCW is planned to be used in ITER). We also present D and He retention results for sequential and simultaneous D<sup>+</sup> and He<sup>+</sup> irradiations of PCW.

Although this section focuses on experimental results, we note that work is also progressing on modeling D trapping in tungsten due to D<sup>+</sup> irradiation. Using the TMAP7 multitrapp diffusion code,<sup>169</sup> deuterium trapping energies were derived from experimental thermal desorption spectra obtained for D<sup>+</sup>-irradiated SCW (Ref. 170).

### IV.A. Diffusivity, Solubility, Permeability, and Recombination Coefficient

Diffusivity is one of the fundamental properties affecting retention and migration of hydrogen in a material. For tungsten, there have been several studies of this basic parameter. Unfortunately, the temperature range over which these measurements have been performed is also quite limited. Frauenfelder<sup>171</sup> used the outgassing rate of hydrogen from saturated samples to determine the diffusivity of hydrogen in tungsten at temperatures between 1200 and 2400 K. A rolled tungsten sheet with a purity of 99.95% was used. The diffusivity determined by Frauenfelder was  $D = 4.1 \times 10^{-7} \exp(-0.39 \text{ eV/kT}) \text{ m}^2/\text{s}$ . Results similar to those of Frauenfelder were determined by Ryabchikov<sup>172</sup> over the temperature range of 1900 to 2400 K. Over the quite limited temperature range of 910 to 1060 K, Zakharov et al.<sup>173</sup> used permeation techniques to determine the diffusivity of hydrogen in 99.9% pure tungsten. Their diffusivity is given by  $D = 6 \times 10^{-4} \exp(-1.07 \text{ eV/kT}) \text{ m}^2/\text{s}$ . Benamati et al.<sup>174</sup> also used gaseous permeation experiments to determine the diffusivity of deuterium in tungsten containing 5% rhenium. Over the very limited temperature range of  $\sim 850$  to 885 K, the values determined for the diffusivity from the permeation data agreed well with an extrapolation of the Zakharov et al. data.<sup>173</sup> It is important to note that trapping was not taken into consideration in the analysis of the data by either Zakharov et al.<sup>173</sup> or Benamati et al.<sup>174</sup> By performing his experiments at temperatures above the range where trapping is effective, Frauenfelder<sup>171</sup>

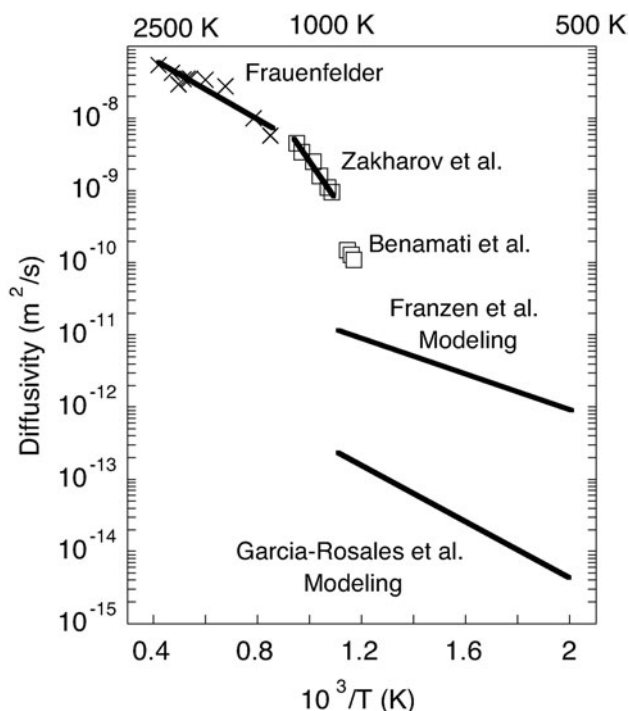


Fig. 19. Diffusivity of hydrogen in tungsten. Data are from Frauenfelder,<sup>171</sup> Zakharov et al.,<sup>173</sup> Benamati et al.,<sup>174</sup> Franzen et al.,<sup>176</sup> and Garcia-Rosales et al.,<sup>175</sup> all contained in Ref. 4.

was able to report diffusivity independent of trapping. Garcia-Rosales et al.<sup>175</sup> modeled the release of deuterium implanted into wrought tungsten and reported the calculated diffusivity to be  $D = 3.5 \times 10^{-11} \exp(-0.39 \text{ eV/kT}) \text{ m}^2/\text{s}$ . Franzen et al.<sup>176</sup> modeled the reemission of deuterium from wrought tungsten and SCW. Their expression for the diffusivity for deuterium in the wrought tungsten is  $D = 1.5 \times 10^{-10} \exp(-0.25 \text{ eV/kT}) \text{ m}^2/\text{s}$ . The activation energy for the SCW was the same as reported for the wrought tungsten, but the leading coefficient was reported to be twice as large. A plot of the diffusion coefficients is shown as Fig. 19.

Similar to the diffusion coefficients for tungsten, the data on the solubility of hydrogen in tungsten is also very limited. In his report, Frauenfelder<sup>171</sup> showed the solubility of hydrogen in tungsten to be given by  $S = 9.3 \times 10^{-3} \exp(-1.04 \text{ eV/kT}) \text{ H}/(\text{W} \cdot \text{atm}^{1/2})$ , where  $S$  is expressed in terms of the hydrogen/tungsten atomic fraction per square root of the hydrogen pressure on the tungsten in atmospheres. His measurements with the 99.95% pure tungsten covered the temperature range of 1100 to 2400 K. Mazayev et al.<sup>177</sup> measured the solubility of hydrogen in tungsten over the temperature range of 1900 to 2400 K. Mazayev et al.'s data agreed well with that presented by Frauenfelder. Benamati et al.<sup>174</sup> also used their permeation data for hydrogen through tungsten with 5% rhenium to approximate the solubility. Over

the limited temperature range of  $\sim 850$  to  $885$  K, they determined the solubility of hydrogen in the tungsten alloy to be a constant  $6 \times 10^{-7} \text{ H}/(\text{M} \cdot \text{atm}^{1/2})$ , where  $\text{H}/\text{M}$  denotes the atomic fraction of hydrogen to alloy. Figure 20 shows a comparison of the reported solubilities for hydrogen in tungsten.

The gas-driven permeation of hydrogen through tungsten has been measured by Frauenfelder,<sup>178</sup> Aitken et al.,<sup>179</sup> Zakharov et al.,<sup>173</sup> and Benamati et al.<sup>174</sup> All four reports list the permeation as being proportional to the square root of the driving pressure. The activation energies reported by the four vary between  $\sim 1.0$  and  $1.4$  eV. It is interesting to note that the two studies at the higher temperatures, Frauenfelder<sup>178</sup> and Aitken et al.,<sup>179</sup> agree quite well. The two studies performed at lower temperatures, Zakharov et al.<sup>173</sup> and Benamati et al.,<sup>174</sup> agree well but do not agree well with the other two. This disagreement points out the danger of extrapolating results to significantly different parameter regimes but also suggests that there may be a change in the mechanisms controlling the process.

The recombination rate coefficient  $K_R$  plays a very important role in determining the uptake of materials exposed to intense hydrogen plasmas. In a report on implantation-driven permeation by Anderl et al.,<sup>180</sup> recombination rate coefficients for hydrogen on tungsten were given. Thin foils of 99.95% purity, reduction rolled,

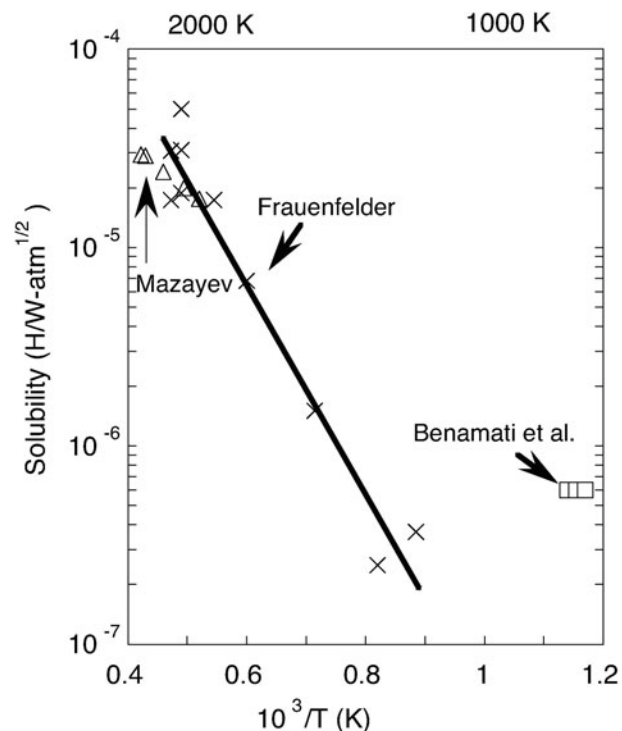


Fig. 20. Solubility of hydrogen in tungsten. Data are from Frauenfelder,<sup>171</sup> Mazayev,<sup>177</sup> and Benamati et al.,<sup>174</sup> all contained in Ref. 4.

powder metallurgy tungsten were used in the permeation studies using 3-keV  $D_3^+$  ions. For measurements over the temperature range of 690 to 825 K, the effective recombination rate coefficient was reported to be  $K_R = 3.2 \times 10^{-15} \exp(-1.16 \text{ eV/kT}) \text{ m}^4/\text{s}$ . Over the temperature range where the measurements were performed, the recombination rate coefficient averaged  $\sim 1 \times 10^{-22} \text{ m}^4/\text{s}$ , a value considerably larger than those measured for materials such as iron<sup>181</sup> and nickel<sup>182</sup> at the same temperatures. It should be noted that in a theoretical calculation of permeation, the assumption of such a value for the recombination rate coefficient on the surface being bombarded would increase the permeation rate by a factor of only 2 in comparison to assuming the diffusing concentration of hydrogen to be zero at that boundary. Causey et al.<sup>183</sup> used an intense flux ( $8.8 \times 10^{21} (\text{D} + \text{T})/\text{m}^2 \cdot \text{s}$ ) of 100-eV ions in experiments on the retention of hydrogen isotopes in high-purity (99.99%) and lanthanum oxide doped powder metallurgy tungsten disks. Experiments were performed over the temperature range of 423 to 973 K. It was reported that not only was the release not recombination rate limited, but also the intense flux increased the effective diffusivity in the implant zone.

#### IV.B. Deuterium Depth Profiles in Tungsten Exposed to $D^+$ Ions and Deuterium Plasmas

The retention of deuterium in tungsten develops differently at different depths. NRA enables D concentrations to be measured to depths of  $0.5 \mu\text{m}$  by detecting alpha particles produced by the  $D(^3\text{He}, \alpha)\text{H}$  reaction and to depths of  $7 \mu\text{m}$  by detecting protons from the reaction  $D(^3\text{He}, p)^4\text{He}$  (Refs. 184 and 185). The depth at which deuterium is retained in W exposed to  $D^+$  can be divided into three zones: (a) the near-surface layer ( $0.2$  to  $0.5 \mu\text{m}$ , depending on ion energy), (b) the subsurface layer ( $0.5$  to  $4 \mu\text{m}$ ), and (c) the bulk ( $>6 \mu\text{m}$ ); see Figs. 21 and 22 (Refs. 186 and 187).

##### IV.B.1. Tungsten Exposed to $D^+$ Ion Beams

When SCW is irradiated with 200-eV  $D^+$  at 300 K, the near-surface D concentration increases from  $\sim 10^{-2}$  to  $\sim 5$  at.% as the  $D^+$  fluence is increased from  $5 \times 10^{22}$  to  $1 \times 10^{24} \text{ D}^+/\text{m}^2$ ; see Fig. 21a. The large increase of the D concentration can only be explained by a structural change during  $D^+$  irradiation, providing traps for D retention. The concentration within the subsurface layer is  $\sim 10^{-2}$  at.% for all ion fluences used (Fig. 21a), whereas the D concentration in the bulk (at depths  $>6 \mu\text{m}$ ) lies in the range  $10^{-4}$  to  $\sim 3 \times 10^{-3}$  at.% (Refs. 186 and 187).

Similarly, in PCW irradiated with 200-eV  $D^+$  at 323 K, the near-surface D concentration ranges from 1 to 5 at.%; see Fig. 21b. Within the subsurface layer, as the fluence is increased to  $1 \times 10^{24} \text{ D}^+/\text{m}^2$ , the D concentration reaches its maximum value of 0.1 at.%, which is about ten times

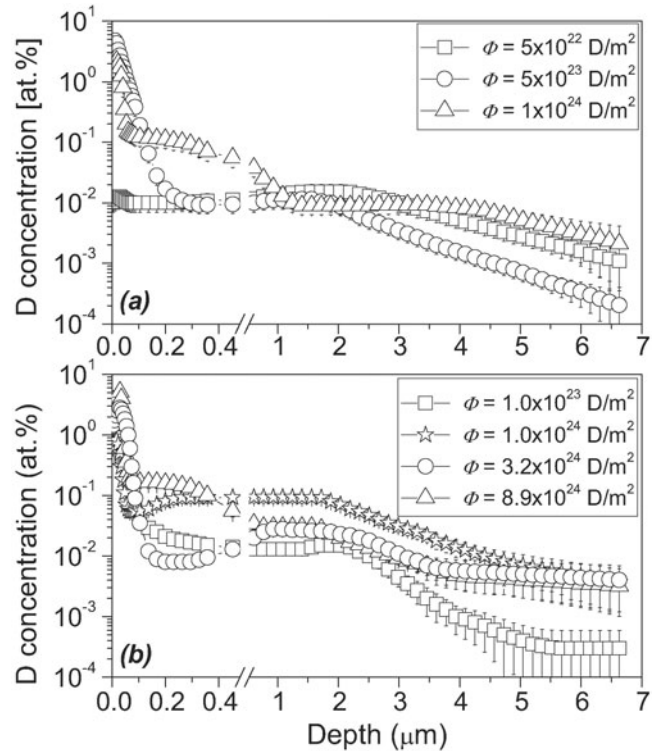


Fig. 21. Depth profiles of deuterium trapped in W irradiated with 200-eV  $D^+$  at 300 to 323 K: (a) SCW and (b) PCW (from Refs. 186 and 187).

higher than SCW. A further fluence increase leads to a decrease in the D concentration, and for fluences  $\geq 3.2 \times 10^{24} \text{ D}^+/\text{m}^2$ , the concentration drops to  $\sim 3 \times 10^{-2}$  at.%. The D concentration in the bulk increases with  $D^+$  fluence and reaches a value of  $\sim 6 \times 10^{-3}$  at.% at fluences  $> 1 \times 10^{24} \text{ D}^+/\text{m}^2$  (Refs. 186 and 187).

Blisters were observed on the surfaces of PCW specimens at ion fluences above  $1 \times 10^{24} \text{ D}^+/\text{m}^2$ . The release of deuterium from the subsurface layer of the PCW may be connected with the appearance of blisters and flaking and accompanying porosity development. Note that blisters were not observed on the surface of SCW irradiated with 200-eV  $D^+$ , and the D concentration did not show a release of deuterium with increasing fluence. More information on blisters is in Sec. IV.C.

##### IV.B.2. Tungsten Exposed to Deuterium Plasmas

The D depth profiles in SCW and PCW specimens exposed to low-energy ( $\sim 200 \text{ eV/D}$ ), high flux ( $\sim 1 \times 10^{21} \text{ D}^+ \text{ m}^{-2} \cdot \text{s}^{-1}$ ) magnetron D plasmas at 303 to 313 K, are characterized by a sharp near-surface concentration maximum of  $\sim 1$  at.% and a decreasing concentration tail into the bulk (Fig. 22). At temperatures in the range 413 to 493 K, the D profile demonstrates, in addition to the near-surface peak, a relatively high D concentration (0.3 to 0.4 at.%) in the subsurface layer. The main difference

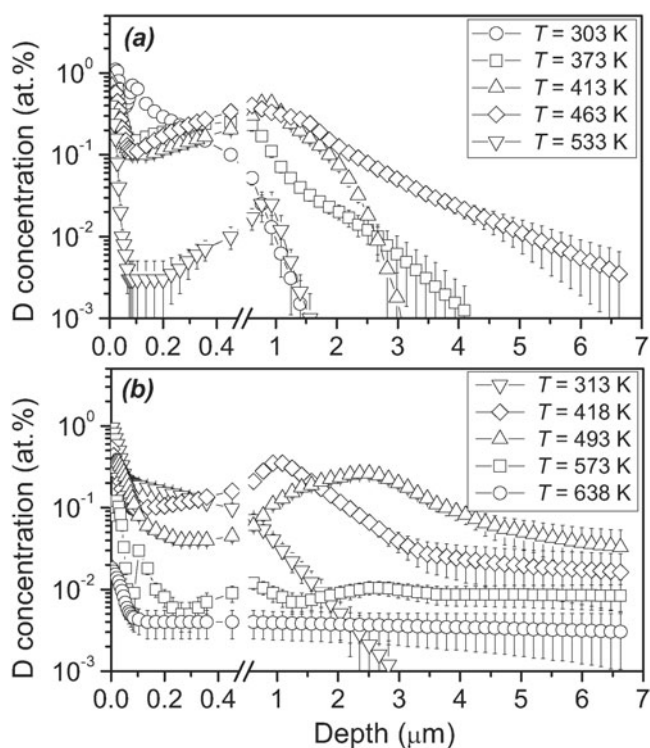


Fig. 22. Depth profiles of deuterium trapped in W exposed to a 200 eV/D<sup>+</sup> plasma with high ion flux ( $\sim 1 \times 10^{21}$  D<sup>+</sup> m<sup>-2</sup>·s<sup>-1</sup>) to a fluence of  $\sim 2 \times 10^{24}$  D<sup>+</sup>/m<sup>2</sup> at various temperatures: (a) SCW and (b) PCW (from Ref. 187).

between SCW and PCW is the constant concentration level in the bulk for PCW, which is absent in the single crystal. The total D retention in both single and PCW increases with the exposure temperature, reaching its maximum value of  $5 \times 10^{20}$  D/m<sup>2</sup> at 463 to 493 K, and then decreases as the temperature increases further<sup>187</sup>; also see Sec. IV.D.1.

The concentration of D<sub>2</sub> molecules (in arbitrary units) within the near-surface layer of SCW exposed to a deuterium plasma at 373 K was determined by measuring the D<sub>2</sub> release rate [residual gas analysis (RGA)] in the course of surface sputtering with Ar<sup>+</sup> ions.<sup>187</sup> A characteristic of the D<sub>2</sub> release rate is that the repetitive D<sub>2</sub> gas bursts occur throughout the whole analysis time, which corresponds to an analysis depth of  $\sim 450$  nm (Fig. 23). The appearance of D<sub>2</sub> molecules is related to the formation of voids filled by gaseous deuterium.<sup>187</sup>

The dependence of the D concentration on the temperature of post-irradiation annealing can provide information about the nature of traps that are responsible for capturing deuterium. Changes in the D depth profile in PCW irradiated at 388 K with 1500-eV D<sup>+</sup> ions to a fluence of  $5 \times 10^{23}$  D<sup>+</sup>/m<sup>2</sup> caused by isochronous annealing (for 10 min) show that there are two ranges of the annealing temperature where the D concentration in W is

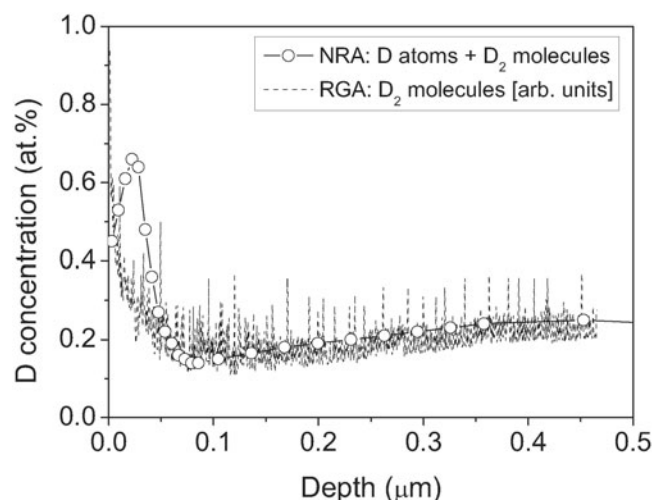


Fig. 23. Depth profile of deuterium trapped in SCW exposed to a 200 eV/D<sup>+</sup> plasma with  $\sim 1 \times 10^{21}$  D<sup>+</sup> m<sup>-2</sup>·s<sup>-1</sup> flux to a fluence of  $\sim 2 \times 10^{24}$  D<sup>+</sup>/m<sup>2</sup> at 373 K as measured with NRA, D(<sup>3</sup>He,α)H, and sputter RGA (from Ref. 187).

significantly reduced: 400 to 500 K (for  $\sim 3$ -μm depth) and 680 to 750 K (depths  $\geq 6$  μm) (Ref. 187). According to van Veen et al.<sup>188</sup> the D<sub>2</sub> gas inside the voids is expected to be released during annealing at 400 to 600 K (detrapping energy  $\approx 1.0$  eV), whereas the D atoms bound on the inner surface of voids (binding energy  $\approx 1.7$  eV) is expected to be released at 700 to 900 K. Using TMAP7 modeling, Poon et al. have identified three trapping energies:  $\sim 1.1$  and 1.35 eV corresponding to vacancy traps and 2.1 eV corresponding to trapping on inner surfaces of voids.<sup>170</sup>

#### IV.C. Blister Formation on the Tungsten Surface

Recent observations of modification of tungsten surfaces by exposure to either hydrogen ion beams or plasmas have shown the formation of blisters.<sup>186,187,189–197</sup> The blister size ranges from one to hundreds of microns, and depends on the structure of the W materials, exposure/irradiation temperature, flux/fluence of hydrogen ions, and the carbon impurity content in the hydrogen beam or plasma. There is some regularity in the development of blisters.<sup>191,194,196</sup> Firstly, for a particular ion energy, blisters are observed on the irradiated W surface after a corresponding critical fluence is reached. Secondly, at low D<sup>+</sup> fluences, the blisters increase in their size and number with increasing fluence, and the size increase tends to saturate at a certain fluence, which might be attributed to rupturing of blisters. Thirdly, the critical fluence for blistering increases with decreasing ion energy. Fourthly, at D<sup>+</sup> energies  $< 100$  eV, the blister size does not appear to depend on the ion energy, whereas at energies  $> 100$  eV, the size increases with increasing ion

energy. Fifthly, carbon impurities in the hydrogen ion beam or plasma enhance blister formation. The reason could be attributed to the formation of a W-C layer on the W surface. This layer prevents the implanted hydrogen from leaving the tungsten and causes enhanced diffusion into the bulk, leading to blister formation. Sixthly, blisters are not formed at temperatures  $>870$  K.

There are two main models that describe the blistering process. One is the gas-driven model<sup>198,199</sup> in which bubbles are assumed to grow by coalescence or the loop punching mechanism. As more D is deposited and bubbles grow, cooperative fracture between the bubbles suddenly becomes an easier way of relieving their overpressure, thus initiating cracks, allowing internal gas release, and lifting the surface of the implanted material into dome-shaped blisters; see, e.g., Ref. 189. In the alternative "lateral stresses model,"<sup>200,201</sup> stresses are assumed to be introduced in the implanted layer, and the surface will buckle if the integrated stress becomes too high. The D concentration in W materials exposed to  $D^+$  ions at conditions when blisters appear on the surface is found to be relatively low ( $\sim 10^{-1}$  at.%); see Figs. 21 and 22. This fact supports the lateral stresses model for the blister formation mechanism.

The high deuterium concentration in the subsurface layer and the formation of blisters lead to the conclusion that low-energy  $D^+$  ions in beams or plasmas modify the surface to depths of up to several microns both for SCW and PCW (Refs. 186, 187, and 189). The sputter-RGA measurement shows that some of the deuterium is accumulated in the form of  $D_2$  molecules in the near-surface layer.<sup>187</sup> The decrease of the D concentration at a depth of  $\sim 1$   $\mu\text{m}$  in PCW at the annealing temperatures 420 to 520 K (Ref. 187) favors the assumption that some of the deuterium retained within the subsurface layer is accumulated in the form of  $D_2$  molecules. As the ion fluence increases, the concentration of gas-filled voids within the subsurface layer (1 to 5  $\mu\text{m}$ ) increases, and interconnected porosity starts to develop. This leads to the release of a fraction of the molecular deuterium and is demonstrated by the decrease of the D concentration in PCW at fluences  $>1 \times 10^{24} D^+/m^2$ ; see Fig. 21b (Refs. 186, 187, and 189). A review of hydrogen bubbles in metals by Condon and Schober<sup>202</sup> outlines some possible void formation mechanisms.

#### IV.D. Temperature, Fluence, and Flux Dependence of Deuterium Retention in Tungsten

##### IV.D.1. Temperature Dependence

The retention of hydrogen in both SCW and PCW exposed to D plasmas is dependent on the exposure temperature; see Fig. 24. For a D plasma with  $\sim 200$ -eV  $D^+$  (high flux of  $\sim 1 \times 10^{21} D^+ m^{-2} \cdot s^{-1}$  flux and  $\sim 2 \times 10^{24} D^+/m^2$  fluence), D retention in both SCW and PCW is  $\sim 1 \times 10^{20} D/m^2$  at  $\sim 300$  K. As the temperature in-

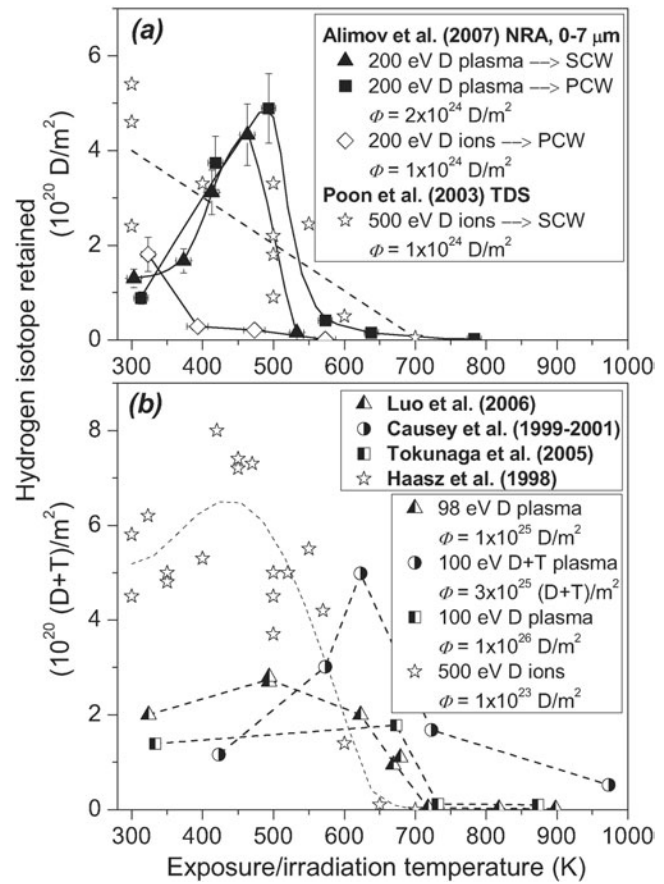


Fig. 24. (a) Temperature dependence of D retention in SCW and PCW exposed to an  $\sim 200$  eV/ $D^+$  plasma with  $\sim 1 \times 10^{21} D^+ m^{-2} \cdot s^{-1}$  flux (from Ref. 187). Deuterium retention curves for PCW (from Ref. 187) and SCW (from Ref. 207) irradiated with 200- to 500-eV  $D^+$  ion beams with fluxes of  $4 \times 10^{19}$  to  $6 \times 10^{19} D^+ m^{-2} \cdot s^{-1}$  are shown for comparison. (b) Temperature dependence of D retention in PCW: data are for low-energy [98 to 100 eV/ $D^+(T^+)$ ] and high flux ( $\sim 1 \times 10^{22} D^+(T^+) m^{-2} \cdot s^{-1}$ ) D or ( $D+T$ ) plasmas and also for a 500-eV/ $D^+$  ion beam with a flux of  $8 \times 10^{19} D^+ m^{-2} \cdot s^{-1}$ . Data in (b) are taken from Refs. 190, 195, 197, 204, and 205. The ion energy and fluence for each exposure/irradiation experiment are indicated in the legend.

creases, the amount of D retained rises to its maximum of  $\sim 4 \times 10^{20}$  to  $6 \times 10^{20} D/m^2$  at 460 to 490 K and then decreases by an order of magnitude to  $\sim 2 \times 10^{19} D/m^2$  at  $\sim 530$  K for SCW and  $\sim 640$  K for PCW; see Fig. 24a (Ref. 187). We note that in both the SCW and PCW exposed to D plasmas at 300 to 310 K, the D retention in the near surface (0 to 0.3  $\mu\text{m}$ ) is higher than in the subsurface layer and in the bulk (0.3 to 7  $\mu\text{m}$ ); see Fig. 22. However, at temperatures  $>350$  K, D retention at depths  $>0.3$   $\mu\text{m}$  starts to dominate and reaches  $\sim 90\%$  of the total D retained at 450 to 500 K (Ref. 203).

In PCW and SCW irradiated with ion beams of 200-eV  $D^+$  and 500-eV  $D^+$  energy at a low flux ( $4 \times 10^{19}$  to  $6 \times 10^{19} D^+ m^{-2} \cdot s^{-1}$ ), the D retention decreases as the irradiation temperature increases above 300 K; see Fig. 24a. However, irradiation of PCW with 500-eV  $D^+$  ions with a flux of  $8 \times 10^{19} D^+ m^{-2} \cdot s^{-1}$  does lead to a maximum in the D retention plot at  $\sim 450$  K (Ref. 204); see Fig. 24b. It is evident that the temperature at which the maximum occurs increases when the flux of D diffusing into the bulk becomes higher. Data on the D retention in PCW exposed to low-energy ( $\sim 100$ -eV  $D^+$ ) and high-flux ( $\sim 1 \times 10^{22} D^+ m^{-2} \cdot s^{-1}$ ) D plasmas<sup>190,195,197,205</sup> show that a large decrease in the D retention is observed at temperatures above 650 to 700 K, whereas for ion fluxes of  $\sim 1 \times 10^{21} D^+ m^{-2} \cdot s^{-1}$ , the decrease in D retention begins at  $\sim 500$  K (Ref. 187). Evidently, the incident  $D^+$  flux (rather the flux of D atoms diffusing into the bulk) affects not only the D retention in W materials, as was reported in Refs. 190 and 206 but also the temperature where the D retention reaches its maximum.

#### IV.D.2. Fluence Dependence

In PCW irradiated at 300 K with 500- and 1000-eV  $D^+$  ions, the retained amount of D tends to saturation for fluences  $> 10^{23} D^+/m^2$  (Refs. 28 and 204); see Fig. 25a. Although the 1000-eV  $D^+$  is slightly above the energy for damage formation (940 eV for  $D^+$ ), the saturation levels for the 500- and 1000-eV cases are very similar ( $\sim 6 \times 10^{20} D/m^2$ ). NRA measurements of the near-surface depth profiles show D being trapped way beyond the ion range to depths of  $\sim 500$  nm at both 500 and 1000 eV (Ref. 184).

Irradiation of W with 500-eV and 1000-eV  $D^+$  at 500 K did not show signs of saturation even at a fluence of  $10^{25} D^+/m^2$ ; see Fig. 25b. This is consistent with a diffusion-limited trapping mechanism (slope  $\sim 0.5$ ) (Ref. 204). However, NRA measurements on both the front and back surfaces of a specimen irradiated with 500-eV  $D^+$  to a fluence of  $10^{24} D^+/m^2$  showed D concentrations of  $\sim 0.05$  at.%, without peaks, indicating a uniform D concentration throughout the bulk.<sup>204</sup>

In vacuum plasma-sprayed W (VPSW) of 9% porosity irradiated with 200-eV  $D^+$  ions at 323 K, the D retention increases as the square root of the ion fluence and does not demonstrate saturation<sup>203</sup>; see Fig. 25a. Relatively high D retention in the VPSW ( $\sim 2 \times 10^{21} D/m^2$  at a fluence of  $10^{24} D^+/m^2$ ) is caused by high porosity of the material. Analysis of deuterium depth profiles after D ion irradiation at various temperatures leads to the conclusion that deuterium is accumulated in the VPSW mainly in the form of  $D_2$  molecules at irradiation temperatures of 300 to 500 K (Ref. 203).

The fluence dependence of D retention in SCW for 500-eV  $D^+$  irradiations at 300 K is similar to that of PCW (Refs. 204 and 207). Initially, the retention increases with increasing  $D^+$  fluence, tending to a saturation level

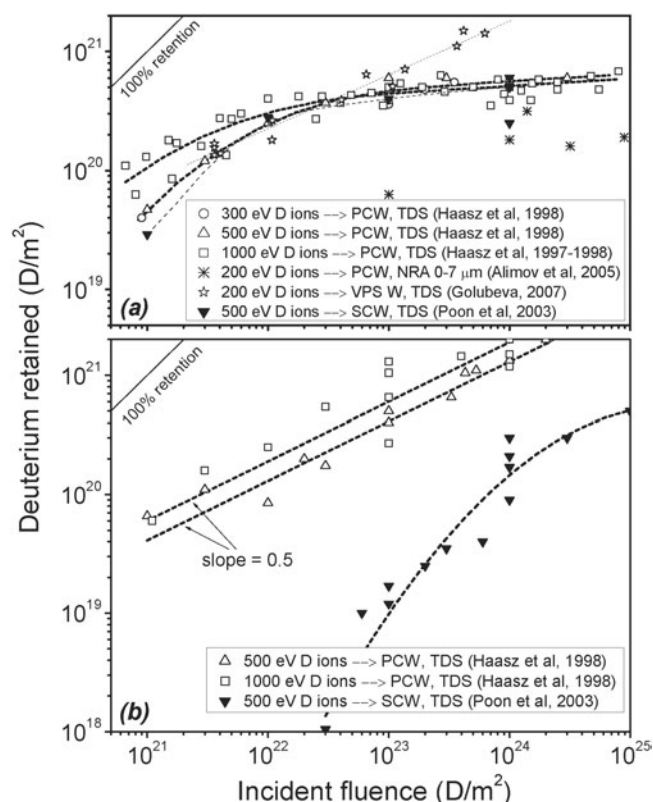


Fig. 25. Fluence dependence of D retention in PCW, SCW, and VPSW (9% porosity) irradiated with 200- to 1000-eV  $D^+$  at (a) 300 to 323 K and (b) 500 K (data are adapted from Refs. 28, 186, 203, 204, and 207).

of  $\sim 6 \times 10^{20} D/m^2$  for incident fluences  $> 10^{23} D^+/m^2$ ; Fig. 25a. At 500 K the retention curves for both SCW and PCW are similar in that they both show an increasing trend with increasing fluence, without reaching saturation even at  $10^{25}/m^2$ ; Fig. 25b. However, they differ in the slope of the curves and the magnitude of the amount of D retained, with the SCW showing less retention,<sup>204,207</sup> which implies significantly fewer trapping sites in the single crystal.

#### IV.D.3. Flux Dependence

Deuterium retention in SCW implanted with 500-eV  $D^+$  ions at 300 K was found to vary significantly at low  $D^+$  ion fluxes ( $< 10^{18} D^+/m^2 \cdot s$ ) and low  $D^+$  fluences ( $< 10^{21} D^+/m^2$ ) (Ref. 206); see Fig. 26. The prominent decrease in retention for fluxes below  $10^{18} D^+/m^2 \cdot s$  suggests a flux threshold level for D retention. For a higher fluence of  $10^{22} D^+/m^2$ , the flux dependence is more difficult to observe (Fig. 26). The suggested explanation for this effect is as follows. Under irradiation, a steady state will be established between the incident  $D^+$  flux and the flux of D diffusing out of the implantation zone, such that the local mobile D concentration will depend on the

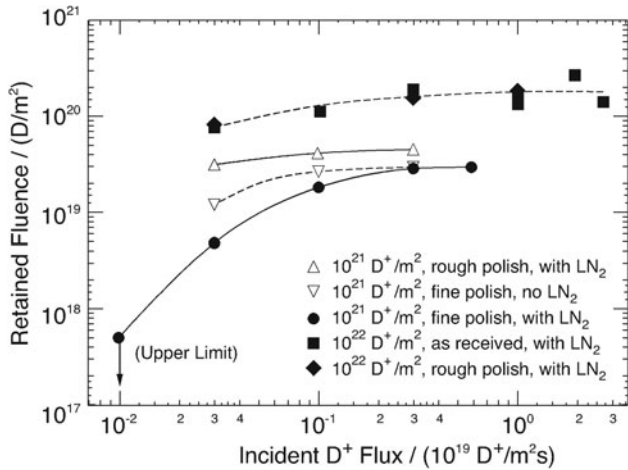


Fig. 26. Deuterium retention in SCW as a function of incident  $D^+$  flux at fluences of  $10^{21}$  to  $10^{22}$   $D^+/m^2$  at 300 K for various experimental conditions (adapted from Ref. 206).

incident flux. Hydrogen trapping is thought to occur only when the local D concentration exceeds a local threshold value, i.e., high enough to cause lattice distortion. Thus, for sufficiently low fluxes, there will not be any hydrogen trapping. For fluxes that lead to mobile D concentrations above the threshold, trapping can occur; however, the rate of trapping does not appear to have any dependence on flux above this threshold value. This threshold effect is present for all fluences studied.<sup>206</sup>

#### IV.E. Effects of Impurities on Deuterium Trapping in Tungsten

The impurities that can potentially affect D retention during  $D^+$  irradiation can originate from either the bulk or from the gas phase during irradiation. Differences in D retention observed for SCW specimens obtained from Johnson-Matthey (JM-SCW) and the State Institute of Rare Metals, Moscow (M-SCW) have been attributed to differences in bulk impurities. The JM-SCW with ten times higher O and C bulk impurities had generally higher D retention.<sup>207</sup>

Secondary ion mass spectrometry (SIMS) depth profiles of M-SCW specimens were used to follow the evolution of near-surface impurities at various stages of the experiments (Fig. 27) (Ref. 207). After  $D^+$  irradiation all of the elements profiled had gained near-surface peaks (Fig. 27b). The peak locations correspond to the  $D^+$  implant zone ( $\sim 20$  nm). It appears that  $D^+$  implantation has enhanced O and C diffusion from the surface into the bulk. Since 500 eV is too low to create vacancies by the  $D^+$  ions, the enhanced diffusion was attributed to lattice strain and dislocations caused by the high concentration of mobile D in a material with very low solubility.<sup>207</sup> Post-implantation TDS (heating to 1775 K) caused a sig-

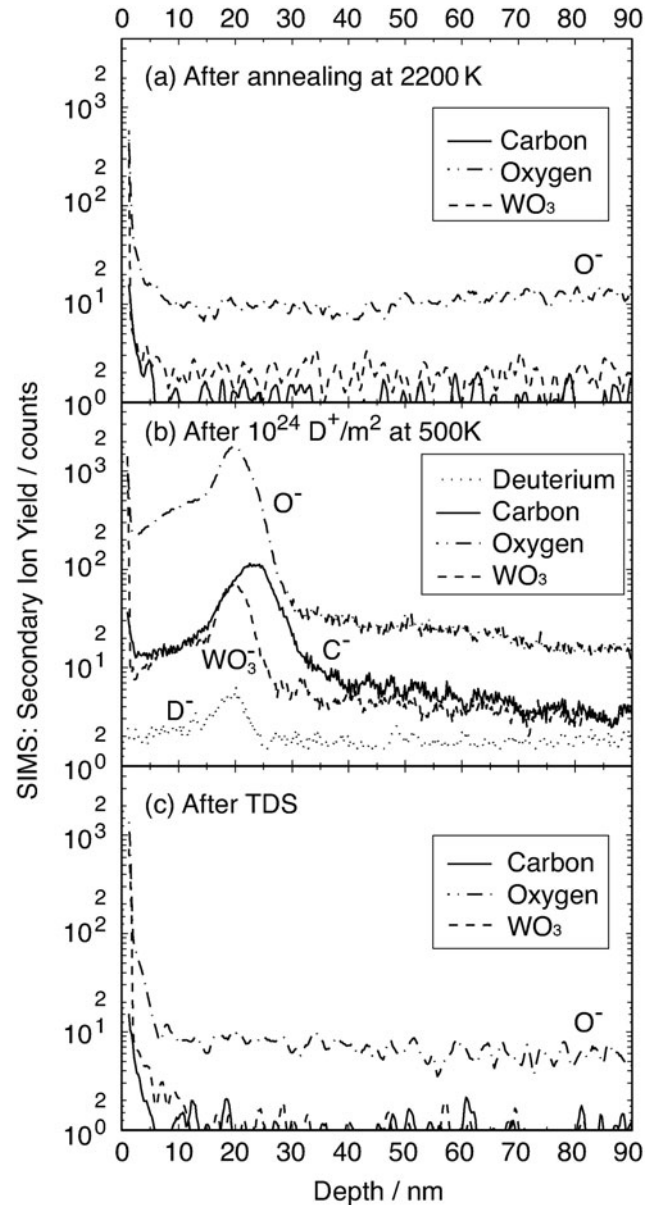


Fig. 27. SIMS depth profiles of Moscow SCW showing the evolution of impurities after (a) annealing at 2200 K, (b) implantation to  $10^{24}$   $D^+/m^2$  at 500 K, and (c) TDS at 1775 K (data are from Ref. 207).

nificant reduction of C and O, dropping to the initial post-anneal levels; compare Figs. 27a and 27c.

Surface impurities originating from the background gas during  $D^+$  irradiation can also affect the amount of D retained.<sup>208</sup> Reduction of the background gas levels has led to reductions in the near-surface O and C concentrations and the retained amount of D. Through elastic collisions, the impacting 500-eV  $D^+$  ions can transfer energy to the O and C atoms<sup>208,209</sup> allowing them to reach depths equivalent to the 500-eV  $D^+$  implant zone.<sup>210</sup> In addition, the energy transfer from O or C to a W atom is sufficient

to create vacancy-type defects where D can be trapped.<sup>211</sup> It then follows that by reducing the impurity content in the background gas, and thus the concentration of surface impurities during  $D^+$  irradiation, the number of vacancies created will be reduced, and the amount of D trapped will decrease, as observed in the experiments.<sup>208</sup> Exposure to background gas impurities during the various stages of the experiment (implantation, postimplantation, and TDS) and the time delay between implantation and TDS may also affect the measured D retention.<sup>210</sup> Air exposure has a negligible effect while post-irradiation time delay leads to detrapping and release of D from shallow traps.<sup>210</sup>

Deuterium retention was also studied in W alloyed with other metals. The presence of 1 to 10% Re in an admixture of W-Re alloy did not influence the deuterium retention within the accuracy of the measurements.<sup>212</sup> With W-La<sub>2</sub>O<sub>3</sub> the fluence dependence behavior of D retention due to 500-eV  $D^+$  implantations at 300 and 500 K was similar to that of pure W; however, the near-surface (within 500 nm) NRA-measured depth distribution in W-La<sub>2</sub>O<sub>3</sub> was a factor of  $\sim 10$  higher than in pure W (Ref. 184).

#### IV.F. Hydrogen and Helium Trapping in Tungsten During Sequential Irradiations at 300 K

Under burning plasma conditions, virtually all tungsten plasma-facing surfaces will be irradiated with D, T, and He ions and neutrals. Material changes due to He ion irradiation may affect the transport, trapping, and recycling behavior of hydrogen in tungsten. Here, we highlight recent experimental results on the effect of  $H^+$  (or  $D^+$ ) on He trapping and the effect of  $He^+$  on H (or D) trapping in PCW for sequential (Sec. IV.F) and simultaneous (Sec. IV.G) irradiations at 300 K (Refs. 213 and 214). For corresponding results at 700 K, refer to Refs. 213 and 214.

##### IV.F.1. Effect of $H^+$ or $D^+$ on He Retention

###### Effect of $H^+$ (or $D^+$ ) post-irradiation on He retention

Comparisons of TDS profiles for 500-eV irradiations of PCW by sequential (SEQ)  $He^+-H^+(D^+)$  and  $He^+$ -only at 300 K show that the characteristic TDS peaks at  $>800$  K typical for the  $He^+$ -only irradiation are not present<sup>213</sup>; compare Figs. 28a and 28b. This indicates that the incident H and D ions have detrapped the He from the more energetic traps. Instead, He was found to desorb at 500 and 680 K, the latter being characteristic of D release for  $D^+$ -only irradiation; see Fig. 28c. The absence of peaks  $>800$  K suggests the elimination of He-vacancy ( $He_nV_m$ ) complexes in the implantation zone.<sup>213</sup>

Helium release at 500 K is the only part of the  $He^+$ -only TDS spectrum that is largely unchanged by post- $H^+$  or post- $D^+$  irradiation. This peak was attributed to He

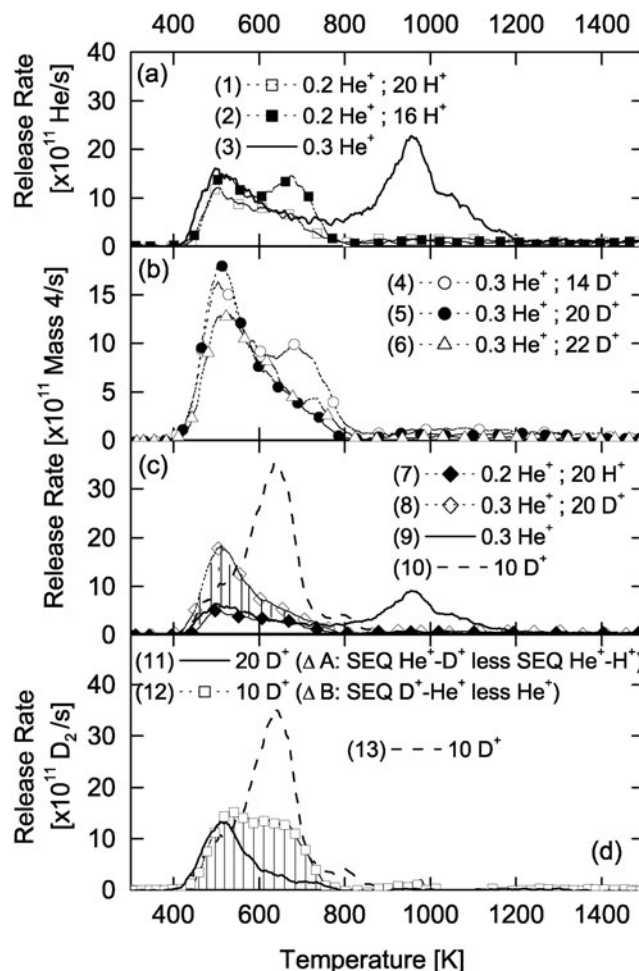


Fig. 28. TDS profiles for 500-eV SEQ irradiations of PCW at 300 K: (a) SEQ  $He^+-H^+$ , (b) SEQ  $He^+-D^+$ , (c) comparison of two SEQ cases with  $D^+$ -only and  $He^+$ -only profiles, and (d) derived profiles for D release compared with a D release profile obtained for  $D^+$ -only irradiation (data are adapted from Ref. 213). (Legend:  $H^+$ ,  $D^+$ , and  $He^+$  fluences are given in units of  $10^{22}$  ions/m<sup>2</sup>.)

trapped at grain boundaries or interstitial loops surrounding  $He_nV_m$  complexes.<sup>213</sup> With the  $He_nV_m$  complexes now removed by  $H^+$  (or  $D^+$ ) postirradiation, the unchanged 500 K peak suggests trapping at grain boundaries. The peak at 680 K, which was not observed for  $He^+$ -only irradiation, may involve He trapping with D (or H), but its reduction with increasing  $H^+$  (or  $D^+$ ) fluence suggests that it is a remnant of the  $He_nV_m$  complex. The concept of joint D-He trapping is supported by the nearly overlapping elastic recoil detection (ERD) depth profiles of D and He in the near surface ( $\sim 20$  to 30 nm). This overlapping of the D and He ERD profiles further implies that the pre-implanted He blocks the transport of D beyond the implantation zone.<sup>213</sup>

### Effect of $D^+$ pre-irradiation on He retention

Here, the sequence of irradiation is reversed:  $D^+$  first, then  $He^+$ . The TDS desorption profiles indicate that in the range of 800 to 1200 K, where no D desorption peaks are expected, the trapping of He is unaffected by the presence of the pre-implanted D, and He is released in the same manner as for  $He^+$ -only irradiations.<sup>213</sup>

### IV.F.2. Effect of $He^+$ on Deuterium Retention

#### Effect of $He^+$ pre-irradiation on D retention

The effect of preimplanted He on D retention can be seen by taking the difference between the SEQ  $He^+$ - $D^+$  and  $He^+$ - $H^+$  profiles shown as hatched area in Fig. 28c; see also  $\Delta A$  in Fig. 28d. It is evident that the postimplanted  $D^+$  is released at  $\sim 500$  K, with the near elimination of the 680 K peak, which is dominant for  $D^+$ -only irradiations.<sup>213</sup> This D release at 500 K appears to be largely unaffected by the He presence. It is possible that the postimplanted  $D^+$  breaks apart the  $He_n V_m$  complexes and retraps interstitially with the He atoms.<sup>213</sup> The overlap of He and D ERD depth profiles suggests a possible He-D trap configuration in the near surface.

#### Effect of $He^+$ post-irradiation on D retention

Subtracting the  $He^+$ -only profile from the SEQ  $D^+$ - $He^+$  gives a good approximation of the D retention profile for the SEQ  $D^+$ - $He^+$  irradiation, shown as  $\Delta B$  in Fig. 28d (Ref. 213). The observed reduction in the 680 K peak, compared to the  $D^+$ -only case, corresponds to  $\sim 40\%$  reduction in D retention. In previous studies the 680 K peak for  $D^+$ -only was interpreted to be D trapped at vacancies at the near surface and extended defects deep in the bulk, e.g., Refs. 207, 215, and 216. Since ERD He depth profiles for 300 K implants show He to be within the near surface ( $\sim 35$  nm), the reduction in the 680 K D peak is attributed to He detrapping of D at vacancies in the near surface.<sup>213</sup>

### IV.G. Hydrogen and Helium Trapping in Tungsten During Simultaneous Irradiations at 300 K

The TDS desorption profiles observed for simultaneous (SIM)  $He^+$ - $H^+$  irradiations closely follow the  $He^+$ -only profiles (Fig. 29a) (Ref. 214). Overall, the presence of  $H^+$  does not appear to have a significant effect on the He release. The total He retained also closely follows the  $He^+$ -only values and fluence dependence trend.<sup>214</sup>

The most revealing difference between the SIM  $He^+$ - $H^+$  and SIM  $He^+$ - $D^+$  profiles occurs in the temperature range of 400 to 800 K, indicating significant contributions of  $D_2$  to the total mass-4 release in the SIM  $He^+$ - $D^+$  cases; see Fig. 29b (Ref. 214). This is the temperature range where D release is observed for  $D^+$ -only irradiations at 300 K (Ref. 207). By taking the difference

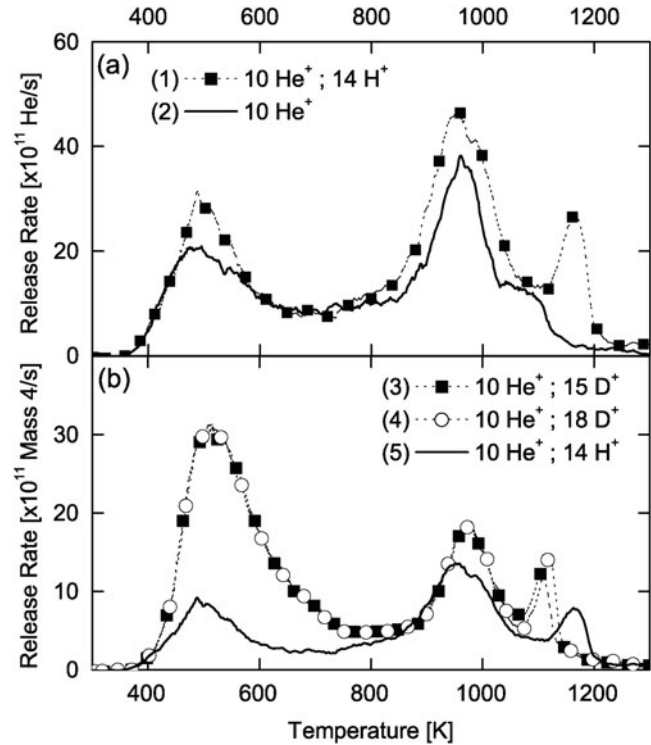


Fig. 29. TDS profiles for 500-eV irradiations of PCW at 300 K for  $He^+$ -only, SIM  $He^+$ - $H^+$ , and SIM  $He^+$ - $D^+$  (data are from Ref. 214). (Legend:  $H^+$ ,  $D^+$ , and  $He^+$  fluences are given in units of  $10^{22}$  ions/ $m^2$ .)

between the SIM  $He^+$ - $D^+$  and SIM  $He^+$ - $H^+$  profiles (Fig. 29b), the D contribution can be derived. Plots of this difference for several  $He^+$  and  $D^+$  fluences reveal only one desorption peak, centered on  $\sim 520$  K; the  $\sim 650$  K peak characteristic of  $D^+$ -only is significantly reduced.<sup>214</sup> This indicates that He has modified the nature of some trapping sites.

ERD depth profiles of D and He for SIM  $He^+$ - $D^+$  at 300 K show that both He and D are confined to a depth of 30 to 35 nm (Ref. 214), similar to the depth profiles seen for SEQ  $He^+$ - $D^+$  irradiations.<sup>213</sup> Deuterium, when implanted alone into tungsten at 300 K, diffuses deep into the bulk ( $>500$  nm) (Ref. 204). Hence, the shallower D range observed for both SIM  $He^+$ - $D^+$  (Ref. 214) and SEQ  $He^+$ - $D^+$  (Ref. 213) irradiations indicates that the presence of He in tungsten limits D diffusion into the bulk.

### IV.H. Tokamak Experience with an All-Tungsten Machine

ASDEX-Upgrade was operated as a full tungsten machine without boronizations during the discharge period 2007. Compared to the earlier predominantly carbon machine, the carbon deposition in the divertor decreased by a factor of  $\sim 15$ , and the long-term deuterium inventory decreased by a factor of 5 to 10. In the predominantly carbon machine, the total D inventory was

dominated by codeposition with C (and to a minor extent with B) in the inner divertor, while in the all-W machine the D inventory is dominated by implantation and deep diffusion at the outer strike point.<sup>217</sup>

#### IV.I. Tungsten Summary and Conclusions

Hydrogen retention in tungsten is mainly controlled by hydrogen's low solubility and high diffusivity in tungsten. In unirradiated tungsten, the diffusing hydrogen is trapped at intrinsic defects in the bulk. However, during D<sup>+</sup> ion irradiation or D plasma exposure, the D concentration in the implantation zone greatly exceeds the solubility limit and stresses the matrix lattice until plastic deformation, coupled with the formation of voids and vacancy clusters, occurs to alleviate these induced stresses. This can occur even at energies below the displacement threshold for D<sup>+</sup> in W (<940 eV). This deformation is assumed to be responsible for the sudden increase in trapping sites for deuterium and the concurrent accumulation of deuterium, both in the form of D<sub>2</sub> molecules and D atoms, at depths of several micrometers. The ion-induced lateral stresses in the near-surface layer can also cause blistering. It has been shown that D retention in W during D<sup>+</sup> irradiation also depends on material structure and impurities in the bulk and on the surface.

The amount of D trapped in W during D<sup>+</sup> ion/D plasma irradiation depends on the D<sup>+</sup> ion energy, flux, fluence, and W temperature. For D<sup>+</sup> energies below ~500 eV, the amount of D retained is a function of irradiation temperature: In some cases a decreasing trend with increasing temperature is seen, while in most cases a maximum in D retention is observed, and the temperature at which the maximum occurs increases with increasing incident D<sup>+</sup> flux. For D<sup>+</sup> energies of 1000 eV or less, and temperatures  $\geq 500$  K, D retention increases with increasing incident D<sup>+</sup> fluence with a slope of ~0.5, which indicates diffusion-limited trapping. Available results at 300 K differ, requiring further studies.

New results on sequential and simultaneous irradiation of W with H<sup>+</sup>(D<sup>+</sup>) and He<sup>+</sup> indicate that the presence of He in the implantation zone acts as a barrier for H(D) diffusion into the bulk.

Generally, one can predict the hydrogen isotope retention in tungsten materials for various implantation conditions. However, further studies are needed to gain a thorough understanding of hydrogen trapping mechanisms, e.g., retention at high ion fluxes and high irradiation temperatures, depth profiles, and analysis of microscopic ion-induced defects. While D retention in a predominantly carbon machine is dominated by C codeposition, in an all-W machine it is dominated by implantation and deep diffusion at the outer strike point. Regarding the use of W in ITER, further investigations are also required to assess the effects of neutron-induced displacements/traps on tritium trapping/retention; such work is now in progress.

## V. HYDROGEN RETENTION IN MIXED MATERIALS

In any plasma confinement device constructed with PFCs made with more than a single element, the issue of fuel retention in a mixture of the plasma-facing elements must be addressed. Much work has gone into the characterization of mixed materials composed of the ITER materials, specifically tungsten, carbon, and beryllium.<sup>218</sup> This section will highlight the present understanding of hydrogen isotope retention in these mixed materials and will also indicate where the existing knowledge base appears to be lacking.

### V.A. Beryllium-Carbon Mixed Materials

PISCES-B linear divertor simulator<sup>219,220</sup> utilizes beryllium-seeded deuterium plasmas to investigate mixed-material erosion and codeposition properties of the Be-C and Be-W material combinations. The beryllium-containing plasma simulates the erosion of a particular first-wall material into the ITER SOL plasma and its subsequent flow toward the carbon and tungsten material located in the ITER divertor region.

The first, most dramatic result obtained from the PISCES-B experiments was the suppression of carbon erosion, both physical sputtering and chemical erosion, at very low levels (~0.1%) of incident beryllium impurity ions.<sup>221,222</sup> Typical deuterium plasma parameters in PISCES-B are ion flux  $\sim 4 \times 10^{22} \text{ m}^{-2} \cdot \text{s}^{-1}$ , incident ion energy ~50 eV, and surface temperature ranging from 400 to 1300 K. This result was confirmed using both spectroscopic as well as weight loss measurements. Initial measurements focused on the equilibrium state of the plasma-exposed surface. In other words, long fluence plasma exposures were performed, after which the surfaces of the plasma-bombarded targets were examined. In addition, during these large fluence exposures, material collectors (referred to as witness plates) were positioned outside the plasma column to collect eroded material.<sup>223</sup>

Subsequent experiments have documented the temporal evolution of the mixed beryllium-carbon plasma-created surface.<sup>224,225</sup> Through focusing on the time-dependent evolution of the surface and its associated plasma-material interactions, the fundamental mechanisms responsible for the mitigation of carbon erosion from the mixed-material surface have been identified. A thin, protective Be<sub>2</sub>C layer forms on the plasma-exposed carbon surface, and this surface layer is responsible for the chemical erosion suppression.<sup>226</sup>

The formation of a mixed-material surface layer has dramatic implications for ITER from the point of view of codeposition. The mixed Be-C surface and the suppression of carbon erosion from the resultant surface causes the codeposited material to become dominated by beryllium codeposition. This work is described in Sec. II.E.

Information on deuterium inventory and thermal stability of graphite targets following exposure to beryllium-containing deuterium plasmas is inferred from gas desorption profiles during thermal desorption mass spectroscopy (TDS). During TDS, targets are heated in vacuum for  $>1$  h with a linear temperature ramp to  $\sim 1400$  K while the partial pressures of deuterium-containing species  $D_2$ , HD,  $D_2O$ ,  $CD_3$ , and  $CD_4$  are monitored using a residual gas analyzer.  $D_2$  and HD are typically the prominent desorption species, and deuterium retention is calculated from the weighted integral of their partial pressure profiles. A calibrated deuterium leak, assumed applicable also for the mixed isotope HD, facilitates conversion of the desorption integrals into a total retention value.

Figure 30 shows desorption fluxes for two targets previously exposed at temperature regimes of  $\sim 600$  K (Fig. 30a) and  $\sim 1000$  K (Fig. 30b). Spectra for targets exposed to plasmas of pure deuterium (dashed lines) and deuterium with  $f_{Be} = 0.001$  (solid lines) are compared. Targets exposed to the pure deuterium plasma received a total ion fluence of  $4.0 \times 10^{26} \text{ m}^{-2}$  while those subject to

the beryllium contamination plasma received a smaller fluence of only  $2.0 \times 10^{26} \text{ m}^{-2}$ .

Figure 30 shows desorption flux trends for the deuterium-containing species,  $m/e = 3$  (HD), 4 ( $D_2$ ) as the targets are heated under vacuum at a constant rate of temperature increase to 1373 K. There is no significant trend in  $CD_4$  desorption or any other deuterium-containing species. The deuterium uptake in graphite is increased in targets exposed to beryllium-containing plasmas compared to a pure deuterium plasma. This result has also been confirmed with NRA of the exposed samples.<sup>227</sup> For targets exposed at  $\sim 600$  K, thermal release is characterized by a release peak at  $\sim 800$  K with a factor of  $>5$  increase in the amount of desorbed deuterium in the beryllium contaminated case. The targets exposed at  $\sim 1000$  K do not show strong thermal release at  $\sim 900$  K presumably because of the higher temperature during plasma exposure. In both temperature regimes the mixed-material surface shows a reduced temperature for the onset of desorption.

In Fig. 31 retention is plotted against target surface temperature during exposure. Data are shown for

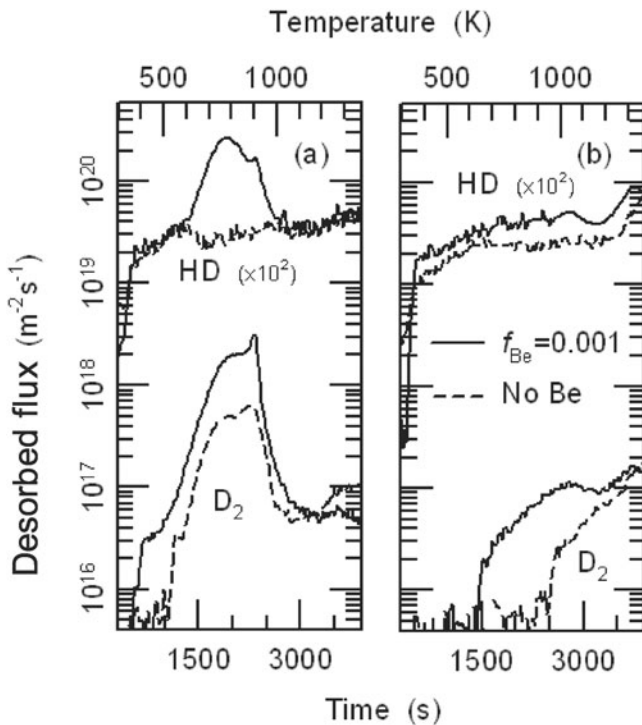


Fig. 30. Thermal desorption spectroscopy profiles for graphite targets previously exposed to pure (dashed lines) and beryllium-contaminated ( $f_{Be} = 0.001$ , solid lines) deuterium plasma at (a)  $\sim 600$  K and (b) 1000 K. The deuterium ion fluence was  $4.0 \times 10^{26} \text{ m}^{-2}$  for the case without beryllium injection and  $2.0 \times 10^{26} \text{ m}^{-2}$  for the cases with beryllium injection (from Ref. 227).

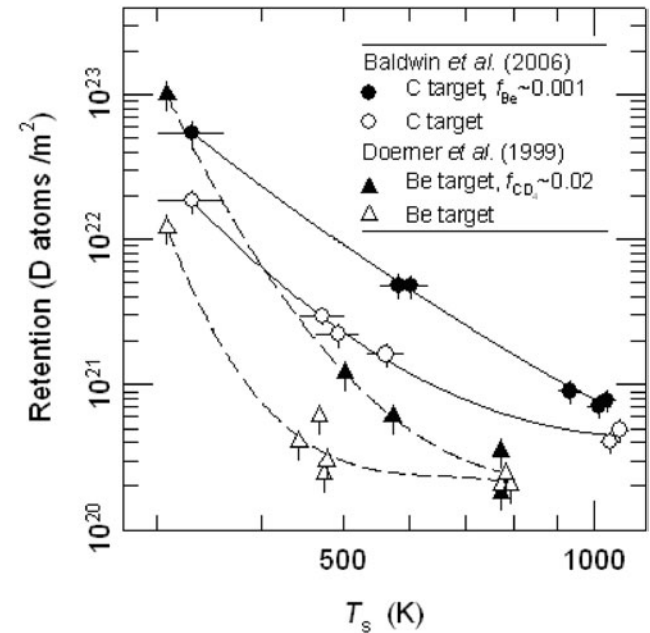


Fig. 31. Deuterium retention in targets as a function of target temperature during plasma exposure. Data are shown from Baldwin and Doerner<sup>225</sup> for graphite targets exposed to a deuterium plasma with and without beryllium injection ( $f_{Be} = 0.001$ ) and from Doerner et al.<sup>228</sup> for pure beryllium targets exposed under similar plasma conditions with and without deuterated methane ( $CD_4$ ,  $\sim 2\%$ ) injection. Both data sets reveal increased retention where a mixed beryllium/carbon surface is present (from Ref. 227).

graphite targets exposed to both beryllium containing,  $f_{\text{Be}} = 0.001$ , and pure, deuterium plasma exposures. The plasma fluences vary from  $2 \times 10^{26}$  to  $5 \times 10^{26}$  D ions  $\text{m}^{-2}$  in this data set. The data show that retention falls significantly with exposure temperature. However, targets with a mixed beryllium-carbon surface show systematically higher retention than targets without. Retention in targets with a mixed-material surface is increased by a factor of  $\sim 4$  at temperatures below 600 K, but this difference is reduced to a factor of  $\sim 2$  at  $\sim 1000$  K. Interestingly, similar trends are observed in the opposite scenario, i.e., beryllium targets exposed to a carbon-containing deuterium plasma. Also shown in Fig. 31 are PISCES mixed-materials retention data from Doerner et al.<sup>228</sup> In those experiments, pure beryllium targets are exposed under similar plasma conditions, and retention is compared for plasma exposures with and without deuterated methane ( $\text{CD}_4$ ,  $\sim 2\%$ ) injection. As with the graphite targets, retention is increased in beryllium targets with a mixed-material layer, and the difference narrows at temperatures beyond 600 K.

The desorption characteristics of graphite targets exposed to a beryllium-containing deuterium plasma are reminiscent of the retention and release behavior of boronized graphite, which exhibits an increase in the retention of hydrogen isotopes as well as a decrease in the release temperature of the trapped hydrogen isotopes.<sup>136</sup> It seems likely that the beryllium-containing plasma bombardment acts to dope the graphite targets during the exposure. Such in situ doping would explain the reduced chemical erosion behavior, the increase in global retention in plasma-exposed surfaces, and the decrease in release temperature of the trapped species.<sup>226</sup>

### V.B. Beryllium-Tungsten Mixed Materials

The other beryllium-containing mixed-material system relevant to the ITER device is the Be-W binary mixture. The tungsten beryllide system<sup>229</sup> consists of three alloys ( $\text{Be}_2\text{W}$ ,  $\text{Be}_{12}\text{W}$ , and  $\text{Be}_{22}\text{W}$ ), all of which have a lower melting temperature than pure tungsten. The importance of beryllide alloy formation was initially observed in PISCES-B because of the unexpected deterioration of the tungsten crucible used in the beryllium oven during the seeding experiments.<sup>230</sup> Subsequent studies of beryllide formation in tungsten samples exposed to beryllium-seeded deuterium discharges have identified the region of plasma conditions necessary for the alloys to form and grow.<sup>231</sup>

In the plasma environment, beryllides begin forming in tungsten surfaces when the temperature reaches  $\sim 873$  K (Ref. 231). However, the diffusion rate of beryllium into tungsten becomes significant only above  $\sim 1073$  K (Ref. 232). It has also been demonstrated that the growth rate of the beryllide alloy is restricted when insufficient beryllium exists in the surface.<sup>231</sup> In the case of ITER utilizing carbon divertor target plates, there

appears to be little likelihood of extensive beryllide formation since the tungsten baffles and dome region will not be hot enough for significant interdiffusion to occur. However, if the ITER design were modified to replace the carbon divertor target plates with tungsten at the divertor strike points, then the tungsten surface would be at much higher temperature, and beryllide growth rates could be significant.<sup>226</sup>

Although there is no information yet available on the deuterium retention characteristics of these mixed Be-W surfaces, one could expect that the high temperatures necessary for their formation might result in little retention of hydrogen isotopes. This, however, still needs to be experimentally verified and is an ongoing area of research.

### V.C. Carbon-Tungsten Mixed Materials

As for hydrogen isotope retention in C-W mixed materials, tungsten carbides and layers of simultaneously deposited carbon and tungsten atoms have been investigated.<sup>233–237</sup>

Chemical vapor deposited (CVD) coatings of tungsten carbides  $\text{W}_2\text{C}$  and  $\text{WC}$  containing  $\sim 10$  at.% of chemically unbound C atoms along with the carbide phase were exposed to a low-energy ( $\sim 200$  eV/D) and high flux ( $\sim 10^{21}$   $\text{m}^{-2} \cdot \text{s}^{-1}$ ) D plasma at various temperatures.<sup>233</sup> The D concentration was measured by means of the  $\text{D}(^3\text{He}, \alpha)\text{H}$  reaction, where both the alpha particles and protons were analyzed. To determine the D concentration at larger depths, an analyzing beam of  $^3\text{He}$  ions with energies varying from 0.69 to 4.0 MeV was used. Additionally, the concentration of deuterium atoms and molecules in the near-surface layers of the plasma-exposed CVD coatings was determined by means of SIMS measurements of  $\text{D}^-$  secondary ion yields and RGA measurements of the partial pressure of  $\text{D}_2$  molecules in the course of surface sputtering. Deuterium molecules were not detected in the RGA measurements, and it may be therefore concluded that deuterium is accumulated in the CVD coatings of tungsten carbides solely as D atoms. Depth profiles of deuterium in the plasma-exposed CVD coatings are shown in Fig. 32. At exposure temperatures above 400 K, D atoms diffuse into the bulk of the coatings and accumulate up to a maximum concentration of  $\sim 2$  at.%. Presumably, deuterium is trapped to carbon precipitates. At temperatures above  $\sim 550$  K, the D concentration in the bulk starts to decrease.

In sequential  $\text{C}^+$  then  $\text{D}^+$  implantation experiments, Poon et al.<sup>237</sup> have shown three zones of D retention: (a) in the outer C layer D retention is similar to what would be expected in graphite; (b) an interface layer of WC with significantly lower D retention; and (c) the substrate W, with W-like D retention levels.

Deuterium retentions in carbon and carbon-tungsten mixed films deposited by reactive magnetron sputtering in  $\text{D}_2$  atmosphere at a pressure of 0.3 to 0.5 Pa have been

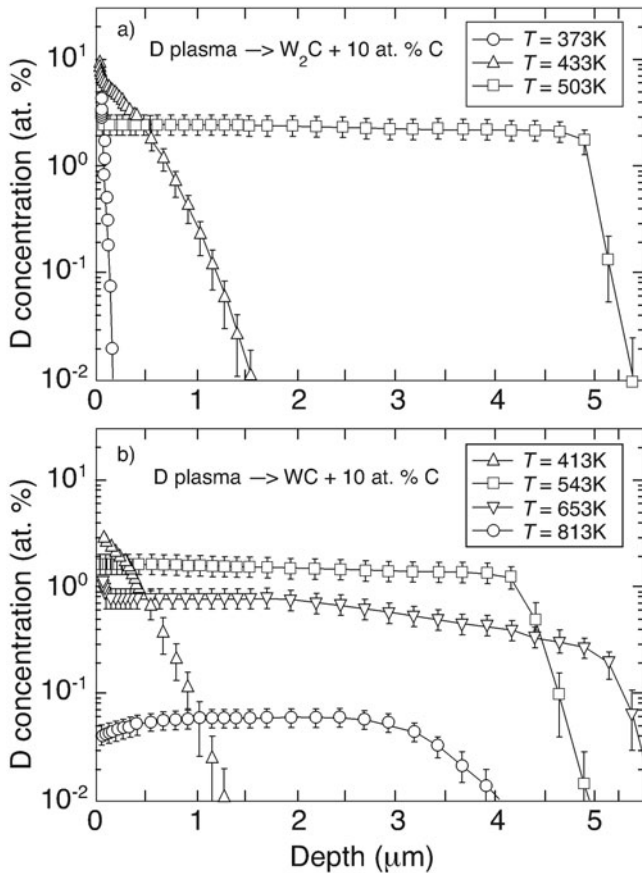


Fig. 32. Depth profiles of (a) deuterium trapped in CVD  $W_2C$  and (b) WC coatings exposed to a low-energy ( $\sim 200$  eV/D) and high ion flux ( $1.1 \times 10^{21} \text{ m}^{-2} \cdot \text{s}^{-1}$ ) deuterium plasma to a fluence of  $\sim 2 \times 10^{24} \text{ D} \cdot \text{m}^{-2}$  at various temperatures (from Ref. 233).

investigated by means of SIMS and RGA measurements.<sup>234</sup> In the C and C-W films, deuterium is distributed homogeneously throughout the film thickness. When the deposition temperature increases, the D concentration in the C films varies from  $\sim 0.4$  D/C (atomic ratio) at 400 K to  $\sim 0.02$  D/C at 973 K (Fig. 33). Similarly, the D concentration in the C-W films falls from  $\sim 0.02$  D/(C + W) at 400 K to values below  $10^{-4}$  D/(C + W) at 973 K. In spite of the presence of carbon atoms in the C-W mixed films (up to 30%), the concentration of deuterium in these films is much lower than is expected from the assumption that the W-C mixed film consists of tungsten and graphite inclusions. The deuterium concentration in the W-C mixed films is close in value to that in tungsten carbides (Fig. 33).

Several types of carbon dust and C-W dust were prepared by  $D_2$  arc discharges using carbon and carbon-tungsten electrodes, respectively.<sup>235</sup> The dust was prepared by changing the substrate temperature while maintaining a constant discharge pressure of 1.6 Pa. The

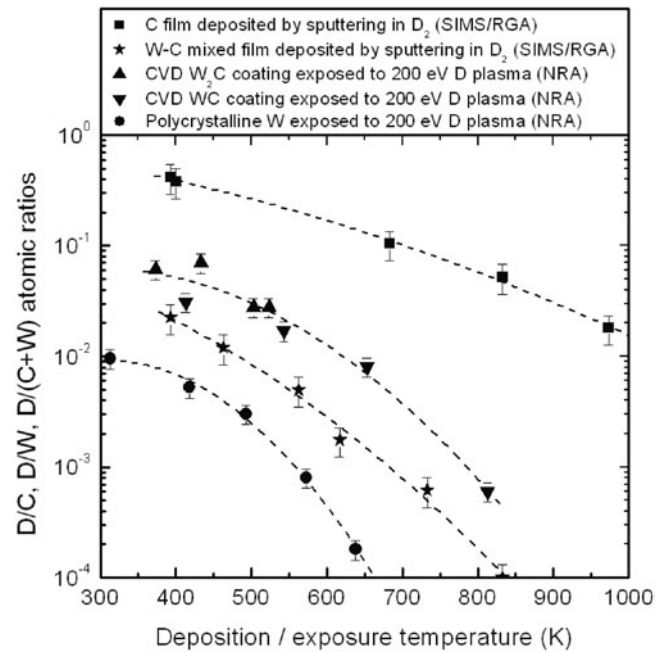


Fig. 33. Deuterium concentration in the bulk of C and C-W mixed films ( $C/W < 30/70$ ) deposited by magnetron sputtering in  $D_2$  atmosphere (from Ref. 234); the near-surface layer of CVD WC and  $W_2C$  coatings exposed to D plasma (from Ref. 235); the near-surface layer of PCW exposed to D plasma (from Ref. 138) as a function of deposition/exposure temperature. The D concentration was determined by means of SIMS combined with RGA (SIMS/RGA) and NRA.

amount of retained deuterium was measured by TDS, whereas the number of C and W atoms was estimated from the weight of the dust and from the C and W concentrations obtained by Auger electron spectroscopy. The results indicate that the deuterium concentration for the carbon dust and C-W dust ( $C/W = 70/30$ ) is reduced from 0.33 to 0.12 D/C and from  $\sim 0.5$  to 0.05 D/(C + W), respectively, when the substrate temperature increases from 300 to 850 K. Katayama et al.<sup>236</sup> reported that in C-W codeposition layers ( $C/W > 60/40$ ) formed at the substrate temperatures in the range from 338 to 393 K by the sputtering method using hydrogen rf plasma, the hydrogen or deuterium concentration is in the range between 0.16 and 0.45 H/(C + W).

It may be concluded that a C-W mixed layer containing carbon  $> 60$  at.% can trap hydrogen, or deuterium, to the same degree as the C layer. The retained hydrogen is thought to be mainly trapped to carbon. When a C-W mixed layer contains only  $\sim 30$  at.% of C atoms, hydrogen isotope accumulation is one to two orders of magnitude lower, depending on temperature, than the accumulation in a pure C layer. It is believed that hydrogen retention is reduced because of formation of tungsten carbides.

#### V.D. Mixed-Material Experience in Tokamaks

The first wall of JET is protected from ion impact by carbon tiles, which cover approximately one-half of the vacuum vessel surface. Charge-exchange neutrals, however, interact with all PFCs including uncovered areas of the vacuum vessel (which is manufactured from the nickel-based alloy Inconel®). Once a week during plasma operations, beryllium is evaporated inside JET from evaporator heads at four equi-spaced locations near the outer midplane. The plasma thus interacts with a complex PFC geometry, and the surface composition of each component may vary with time and with the distance to the Be evaporators. The impurity content of the plasma is determined by the species sputtered from this mixture of PFC surfaces: Carbon is the dominant impurity, with Be at a mean value of ~8% of the C level, and Ni, Cr, and Fe (from the Inconel®) at least an order of magnitude lower than the Be. Impurities leaving the confined plasma enter the SOL and in JET are swept toward the inner divertor by the SOL flow.<sup>238</sup>

Impurities arriving at the inner divertor may be expected to have the same composition as those in the plasma. However, because of the large flux of H-isotope ions and neutrals in the divertor region, carbon atoms arriving along the SOL have a high probability of being chemically sputtered, whereas Be and the metals do not. Thus, in JET the region of the inner divertor intercepted by the SOL is found to have a deposited film enriched in Be relative to C (Be:C ratios in the range 1 to 2), with a proportion of metals commensurate with the Be. The majority of the carbon is transported to shadowed regions in the corner of the divertor.<sup>85,86,239</sup>

The plasma-facing surface of the inner divertor in JET is thus a mixed material, with film thicknesses up to 90 μm thick on CFC tiles 1 and 3 (Fig. 10) (Refs. 85 and 88). Some work on ascertaining the structure of the layer, such as whether there are Be carbides present, is ongoing. Measurements of properties of the layer relevant to the performance of the inner divertor such as sputtering coefficients, thermal conductivity, H-isotope retention, and detritiation behavior are planned, since similar materials may form in the ITER divertor if the main chamber wall is Be and the divertor target is carbon.

#### V.E. Mixed-Material Summary and Conclusions

The understanding of mixed materials, in general, and their behavior with respect to hydrogen uptake and release, in particular, has increased dramatically during the period of this CRP. However, predictions for what to expect in ITER are still problematic. The biggest uncertainty to addressing mixed-material issues in ITER is the relatively poor understanding of impurity creation rates and locations, as well as imprecise predictions of the material transport in the edge and SOL of confined plasmas.

Given these uncertainties, one can still predict that where carbon-containing mixed materials exist, there is a higher probability of finding larger amounts of retained hydrogen isotopes. For example, the D/C ratio approached unity in JET in divertor codeposited surfaces composed of primarily carbon. On mixed-material surfaces in JET that contained large amounts of metallic species (Be/C ~ 1), the tritium retention is typically about an order of magnitude less.<sup>84</sup>

Operation at higher surface temperature can reduce tritium retention in two ways. Firstly, at higher surface temperature, the hydrogen retention in mixed materials decreases, as it does with mono-elemental materials. Secondly, during operation at higher temperature with carbon-based mixed materials, the carbon tends to bond as a carbide at higher temperature. This effect can alleviate the likelihood of hydrogen bonding to the carbon atoms, thereby reducing retention as well as reducing the chemical erosion of carbon, which reduces the source term for codeposition.

### VI. DETRITIATION OF PLASMA-FACING MATERIALS

Tritium removal from PFCs is a critical issue for the operation and licensing of magnetic fusion reactors. Tritium is important in safety assessments; it is also expensive and in short supply. In next-step machines the order-of-magnitude increase in duty cycle will greatly increase the tritium accumulated per day of plasma operations while drastically reducing the time available for its removal.<sup>240</sup> The lack of tokamak demonstrations of tritium removal at the speed and efficiency required for ITER (Ref. 241) has led to questions on the licenseability of carbon PFCs during the tritium phase on ITER. Techniques for tritium removal from metal PFCs and mixed materials are less well developed especially for tritium trapped deep in the material. Hydrogen removal from codeposits has been previously reviewed in Refs. 3 and 6 through 9.

The use of carbon as a first-wall material has shown that substantial amounts of the fuel injected into the vacuum vessel are codeposited in surface layers and/or implanted into the surface of the carbon tiles (Sec. III.C). A particular concern is the location of these deposits; in several tokamaks deposits are found in regions shadowed from the plasma such as duct scrapers (TEXTOR), beneath the divertor (ASDEX), and on louvers beyond the inner corner of the divertor (JET). Access to such deposits for in situ cleaning may be difficult. The layers are basically hydrocarbons in chemical composition; i.e., they contain massive amounts of hydrogen, and occasionally their thicknesses may reach a few tens of micrometers. Even worse, sometimes they become so thick that they spall off to form flakes, many of which fall into the subdivertor zones of the machine.

Tritium removal techniques are typically tested first ex situ on tiles retrieved from tokamaks; however, tokamak demonstrations are essential to demonstrate that tritium is not simply reabsorbed before evacuation from the tokamak or redistributed as dust in inaccessible regions. Numerous experimental techniques have been investigated for the in situ and ex situ detritiation of the plasma-facing materials. While the in situ techniques are limited by the conditions permissible inside the torus, the ex situ detritiation techniques can employ much more aggressive treatments both in temperature and/or reagents (use of oxygen, ozone, etc.) that are normally not possible inside the vacuum vessel. A number of these detritiation techniques have been tested during the period of this CRP and are described briefly in Secs. VI.A, VI.B, and VI.C. First, noninvasive in situ techniques such as gas treatments are considered, then techniques involving the use of equipment to clean off deposits in situ such as laser and photon cleaning (Sec. VI.B) (which as a backup solution can also clean components ex situ) are considered, and finally techniques designed for detritiation of components ex situ prior to disposal are described (Sec. VI.C).

### VI.A. In Situ Detritiation by Gas Treatments

#### VI.A.1. Cleaning in Oxygen

One of the methods proposed for the removal of tritium from tokamak codeposits is thermo-oxidation, which removes the codeposit via the formation of reaction products  $D_2O$ ,  $CO$ , and  $CO_2$  (Refs. 242 and 243). Laboratory studies have demonstrated that the codeposit erosion rates and the associated D removal rates depend on the film structure, the oxidation temperature, and oxygen pressure, e.g., Refs. 244 and 245. Recent oxidation studies of DIII-D codeposits have shown that the effect of increasing the temperature and/or pressure leads to increases in the initial erosion rates and decreases in the final D content.<sup>244,245</sup> Significantly larger initial erosion rates are best achieved by increasing the temperature rather than increasing the pressure; see Fig. 34 (Ref. 244). At 673 K and 79 kPa, the D content was reduced by about an order of magnitude in 15 min, roughly corresponding to a film erosion rate of  $\sim 10 \mu\text{m/h}$  (Ref. 244).

The final D content after prolonged oxidation is seen to decrease with increasing temperature and increasing pressure.<sup>244</sup> After 2 h of oxidation at 673 K and 79 kPa, the remaining D content was reduced to  $\sim 5 \times 10^{20} \text{ D/m}^2$ , down by a factor of  $\sim 30$  from the initial level of  $\sim 1 \times 10^{22}$  to  $2 \times 10^{22} \text{ D/m}^2$ , and a further decreasing trend with increasing oxidation time is evident as seen in Fig. 34 (Ref. 244). A possible explanation of the reduced oxidation rate with oxidation time is the buildup of impurity elements in the deposited films by the preferential erosion of carbon. For the DIII-D specimens studied,<sup>244–248</sup>

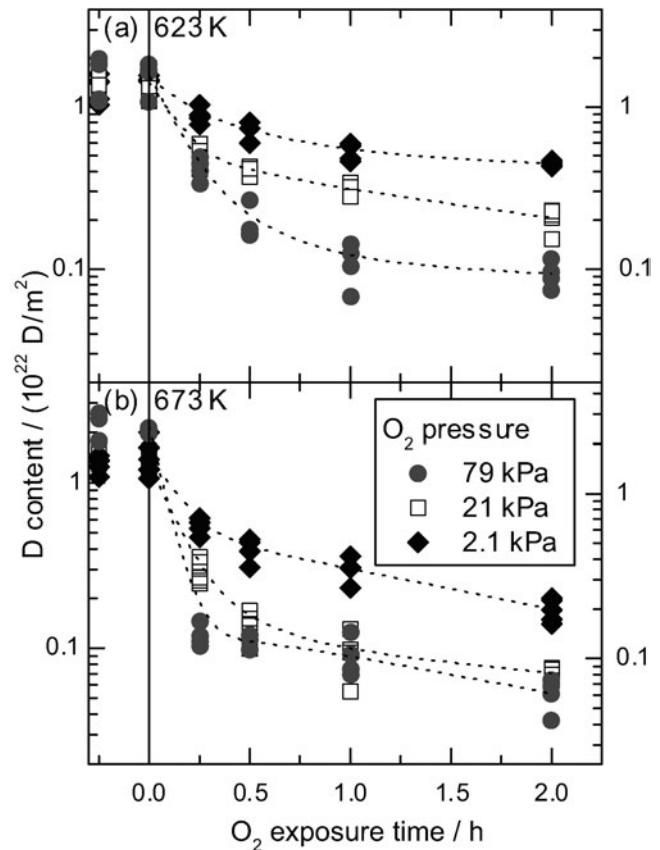


Fig. 34. Measured D content and derived codeposit film thickness for DIII-D divertor tile specimens as a function of oxidation time (data are from Ref. 244).

the “D removal efficiency” (i.e., reduction in D content divided by the initial D content) as a function of initial near-surface boron impurity concentrations is plotted in Fig. 35 (Ref. 244); B was the dominant impurity. For an initial B content of  $\sim 2$  to 3%, the D removal efficiency at 673 K and 79 kPa  $O_2$  pressure was  $>95\%$ . (By comparison, the oxidative erosion rate of the graphite substrate is orders of magnitude lower than the erosion rate of tokamak codeposits.<sup>8,249</sup>)

Oxidation has also been performed on thick (10 to 250  $\mu\text{m}$ ) codeposits with high impurity content [up to 50% Be/(Be + C)] removed from the JET MkII-GB divertor after the 1998–2001 campaign.<sup>85</sup> During oxidation at 623 K and 20-kPa  $O_2$  pressure, the initial D removal rates increase nearly linearly with inherent D content; see Fig. 36. About 50% of the inherent D was removed in the first 15 min, independent of thickness and Be content, and after 8 h of oxidation,  $>85\%$  of the inherent D was removed; see Fig. 37. This implies that the structure of the codeposit is likely to be highly porous such that erosion occurs throughout the layer and not from the geometric surface inward.<sup>250</sup> The observed different effects of B (DIII-D) and Be (JET) on the

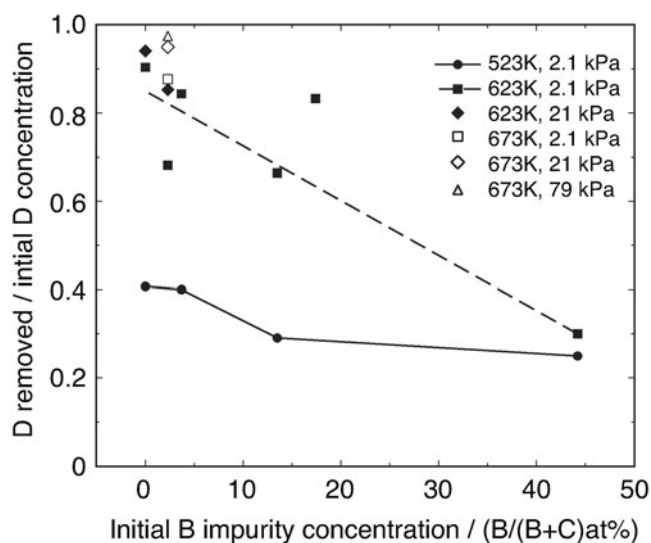


Fig. 35. DIII-D divertor codeposits: Loss of D content due to oxidation divided by the initial D content plotted against the initial boron impurity content in the near surface of the codeposit (data are from Refs. 244, 246, 247, and 248).

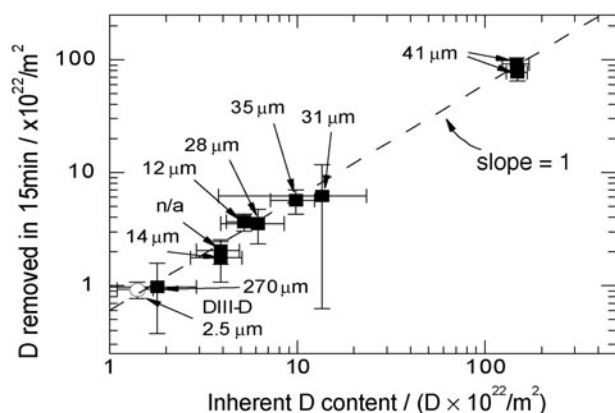


Fig. 36. JET divertor codeposits: Initial D removal rate (based on the first 15 min of oxidation) versus inherent D content (data are from Ref. 250).

codeposit removal rates are attributed to differences in the chemistry involving  $B_2O_3$  and BeO (Ref. 250). Post-oxidation analysis of the codeposit is currently underway.

#### Oxidation experience in tokamaks

Controlled oxidation experiments performed in TEXTOR (Ref. 251) at 500 to 700 K temperature and 0.7- to 30-Pa  $O_2$  pressure have also shown the release of CO,  $CO_2$  and water. Similar results were also obtained in HT-7 (Ref. 252). Additional tokamak experience with oxidation has been inadvertently obtained from the oc-

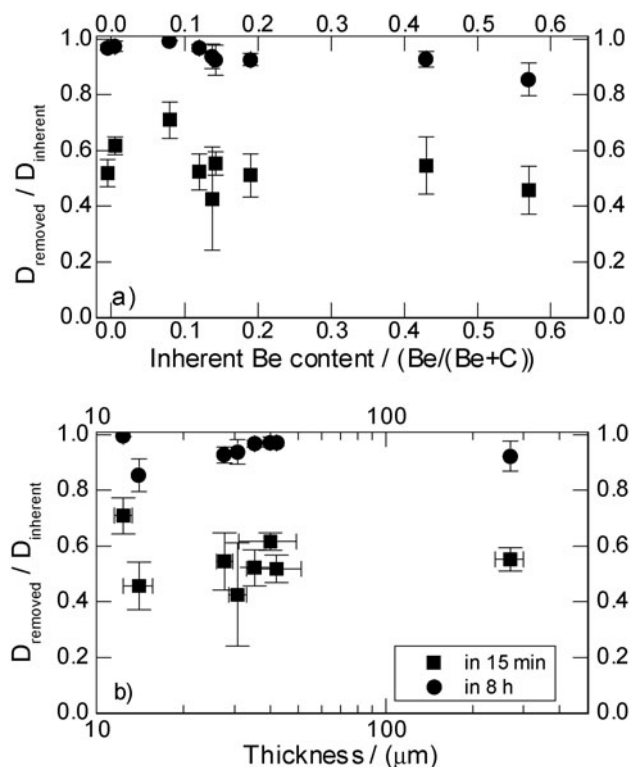


Fig. 37. JET divertor codeposits: The amount of D removed during the first 15 min and during the full 8 h of oxidation period, normalized by the inherent D content, is plotted as a function of (a) inherent Be/(Be + C) content and (b) codeposit thickness (data are from Ref. 250).

casional accidental air leaks into operating tokamaks at elevated temperatures. In all of these cases, including the controlled TEXTOR oxidation tests, postoxidation plasma operation was recovered after applying normal wall-conditioning procedures, e.g., GDC in  $D_2$  and He in TEXTOR (Ref. 251).

#### Implication for ITER

Assuming that ITER codeposits will have similar structure and impurity content as the JET codeposits, we would expect that thermo-oxidation at 623 K and 20-kPa  $O_2$  pressure would remove >85% of the D from the codeposit after ~8 h, independent of Be content and codeposit thickness.

The release of tritium from codeposits during thermo-oxidation will be predominantly in the form of  $T_2O$ /DTO (Ref. 242). Thermo-oxidation in ITER might liberate up to 700 g of T along with 470 g of D, leading to the production of ~4900 g (D, T) $_2O$ . The baseline water processing rate for the ITER tritium plant is 33 g/h. At this rate it would take 150 h (~6 days) to process this tritiated water. Thus, a scale-up of the current water detritiation

system or a separate tritiated water processing system would likely be needed to accommodate this load.

Highly tritiated water is corrosive; because of this it will be important to ensure that no tritiated water vapor is allowed to condense as liquid and remain for extended periods of time. The tritiated water vapor must be transported through ductwork, and it is important to ensure that this vapor does not condense in unwanted locations. This might necessitate additional heating of ductwork and components. However, it is already recognized that tritiated water in the normal torus exhaust will not be diluted by (H,D)<sub>2</sub>O, and heated ductwork is planned whether or not thermo-oxidation is used.

#### VI.A.2. Use of Helium-Oxygen Discharges

The possible synergy of adding O to a He glow discharge along with heating has been examined by Kunz et al.,<sup>253</sup> using a graphite tile covered with a relatively thick codeposited layer removed from the TFTR reactor with a D/C ratio of  $\sim 0.2$ . The samples were examined before and after treatment microscopically using Auger scanning electron microscopy and by IBA techniques. The samples were then exposed to a He-O glow discharge at temperatures varying from 373 to 513 K (the latter being the highest obtainable temperature in ITER without draining the coolant). The gas consisted of 80% helium and 20% oxygen and was held at a pressure of 13.2 Pa during the discharge. The gas purity was maintained by slowly pumping on the vacuum vessel at the same time fresh gas was supplied.

After exposure to the glow for 4 h at 443 K, the amount removed was  $< 1 \mu\text{m}$ , implying a removal rate of  $\sim 0.35$  carbon atoms/ion.<sup>253</sup> Much higher rates were reported by Hsu<sup>254</sup> (five carbon atoms/ion) and Jacob et al.<sup>255</sup> This may be due to differences in the films treated, or due to a sharp decrease in rate with time as observed by Cowgill.<sup>256</sup> Microscopic examination of Cowgill's samples after low-temperature exposure revealed a "grass-like" or "hairlike" structure that is resistant to further removal. The increased temperature used in this study apparently does not facilitate oxygen reaction with the individual strands of the structure. IBA suggested some loss of deuterium from near the surface.<sup>256</sup>

In the more recent work of Hu et al.,<sup>252</sup> oxidation with both ion cyclotron resonance (ICR) discharge and GDC at 400 to 470 K yielded codeposited layer removal rates of about 20 times that of He ICR and He GDC. While the use of carbon removal rate *per hour* in Ref. 252 instead of *per unit area per hour* made the removal rates difficult to quantify, the simple fact that the removal rate was only twenty times that of He GDC clearly shows that O<sup>+</sup> fluxes would need to be increased significantly for this process to be of use for deposit removal in ITER.

In conclusion, the available results confirm that this combination of removal techniques is not an effective way of removing the codeposited carbon/tritium layer produced in fusion reactors.

## VI.B. Photon Cleaning: Laser and Flashlamp

### VI.B.1. General

Laser-induced desorption<sup>257</sup> or ablation<sup>258</sup> is a reliable method to remove tritium retained in near-surface layers of a PFC. Advantages of tritium removal using lasers are the ability to remove tritium from plasma-shadow regions, little or no production of hazardous tritiated water, and no deconditioning of plasma-facing surfaces with oxygen. Many experiments on the removal of hydrogen isotopes from carbon materials have been conducted using different types of laser or photon sources with various wavelengths, pulse durations, and intensities; see Refs. 259 through 276.

When a laser beam is irradiated on carbon materials, many different processes can occur depending on the laser intensity  $I_L$ . In the region where  $I_L$  is less than the threshold intensity for ablation  $I_{ablation}$  or vaporization [nonablation region (NAR)], only thermal desorption of hydrogen isotopes occurs. When  $I_L$  is  $> I_{ablation}$  (ablation region), sublimation of both carbon materials and hydrogen isotopes occurs, and ablative removal of the target materials starts. While continuous lasers can attain the highest time-average intensities, pulsed lasers can attain very high peak intensities and are usually used for the ablation region. When  $I_L$  is increased further, ionization of ablated carbon materials due to inverse bremsstrahlung absorption and multiphoton ionization begin at another threshold laser intensity  $I_{ionize}$  (Refs. 275, 276, and 277). Hereafter, the region at  $I_{ablation} < I_L < I_{ionize}$  is referred as the weak-ablation region (WAR) and that at  $I_L > I_{ionize}$  as the strong-ablation region<sup>270,271</sup> (SAR). In Fig. 38 NAR, WAR, and SAR are distinguished in terms of emitted particles, ions, and photons.<sup>278</sup>

Laser-induced desorption in NAR with a surface temperature of  $\sim 1000$  to 2000 K has released gaseous deuterium and tritium molecules from codeposited layers of  $\sim 100\text{-}\mu\text{m}$  thickness.<sup>267</sup> In the ablation region, the surface layers (including the hydrogen contained therein) are continuously removed. In WAR, however, the released hydrocarbons would stick or redeposit somewhere near the ablated area with incorporation of tritium. In this respect, SAR is more desirable because of larger removal efficiency and less production of tritiated hydrocarbons although it faces the issue of the subsequent removal of ablated tritiated particulates from the vessel.

In the following sections three different sets of experiments are described: photon cleaning (Sec. VI.B.2) and two examples of the use of lasers in different modes—desorption of tritium (NAR) (Sec. VI.B.3) and strong ablation (SAR) (Sec. VI.B.4).

### VI.B.2. Flashlamp Cleaning of JET Divertor Tiles

A photon cleaning unit consisting of a flashlamp capable of delivering 500 J at 5 Hz with a pulse width of

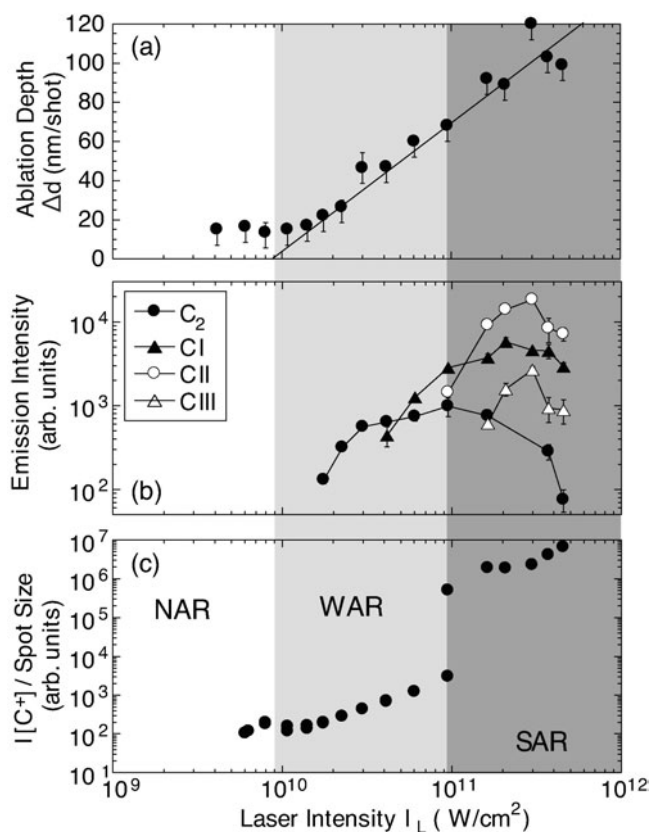


Fig. 38. (a) Ablation depth per laser shot,  $\Delta d$ ; (b) intensities of optical emission  $I[C_2]$  (471.5 nm),  $I[CI]$  (909.4 nm),  $I[CII]$ , (426.7 nm), and  $I[CIII]$  (465.1 nm) roughly at the 600th laser shot; and (c)  $C^+$  signal intensity  $I[C^+]$  of time of flight mass spectroscopy versus laser intensity  $I_L$ . Three regions, NAR, WAR, and SAR, are distinguished (after Sakawa et al.<sup>278</sup>).

140  $\mu\text{s}$  was used to remove tritium from deposited films on tiles from JET. Trials of the photon cleaning unit were carried out in-vessel using remote handling at JET (Ref. 271), and further trials were completed in the beryllium handling facility (BeHF) at a range of pulse energies and repetition rates.<sup>279</sup> Tiles were examined with IBA and SIMS before and after treatment. At low energies ( $<100$  J), some H isotopes were desorbed but only from the top 1  $\mu\text{m}$  at the surface of the film. For pulse energies from 150 to 300 J, a limited removal of material from the tile surface was observed, but this was insufficient for cleaning off thick films.

In further trials, tiles were sectioned before and after treatment with 500-J pulses. By comparing the difference in thickness between the untreated and treated regions, the total amount of material removed was 70  $\mu\text{m}$  from a region at the edge of the tile and 90  $\mu\text{m}$  from an area away from the edge,  $\sim 40\%$  of the deposit in the latter area. From the total number of pulses used to treat the two regions, removal rates were of the order 0.05 and

0.03  $\mu\text{m}/\text{pulse}$ , respectively. The total T removed from the tile was  $\sim 0.081$  Ci (8.4  $\mu\text{g}$  T) from a total area of  $18 \times 10^{-4}$   $\text{m}^2$ .

During cleaning, the release of T per pulse was found to decrease with an increasing number of pulses. Results from SIMS show the presence of nickel at the surface.<sup>279</sup> This indicates that Ni is not removed efficiently during the photon cleaning process and consequently builds up on the surface. Physical removal of this layer restored the T release rate to its previous value. SIMS and IBA show that D is partially depleted ahead of the removal front, to a depth of  $\sim 10$   $\mu\text{m}$ .

Based on these removal rates, and assuming a continuous operation of the flashlamp at 500 J/pulse and frequency of 5 Hz, a 10- $\mu\text{m}$  deposit would be removed at the rate of 0.06  $\text{m}^2/\text{h}$ . In order to increase the removal rate, the temperatures at the tile surface would need to be raised. This might be achieved with minor modifications to the current photon cleaning system so that lower-energy pulses in rapid succession could be delivered to the tile surface; however, application to ITER would require a major increase in removal rate and the necessary technology to remove the ablation products from the vessel.

### VI.B.3. Laser Cleaning by Desorption of Tritium

A novel method for tritium release was proposed by Skinner et al.<sup>257</sup> in 1997 and has been successfully demonstrated on codeposited layers on tiles retrieved from TFTR and from JET (Refs. 265 and 267). A scanning continuous-wave Nd laser beam was focused to  $\approx 100$   $\text{W}/\text{mm}^2$  and scanned at high speed over the codeposits, heating them to temperatures of  $\approx 2300$  K for  $\sim 10$  ms in either air or argon atmospheres. Up to 87% of the codeposited tritium was thermally desorbed from the JET and TFTR samples in laboratory experiments. Fiber-optic coupling between the laser and scanner was implemented that would enable the laser to be located remotely from the tokamak.<sup>267</sup> The temperature excursion would also release volatile impurities from the tiles, and improved wall conditioning may prove to be a significant collateral benefit to subsequent plasma operations. Unlike laser ablation techniques (Sec. VI.B.4) that create particulate debris that could be dispersed to hard-to-access areas, this technique generates gaseous tritium, mostly in the elemental form that can be pumped out of the tokamak (such a laser thermal desorption technique has been extensively used by Haasz et al. to measure D content in various materials, including codeposits, e.g., Refs. 244, 245, and 250). This technique also avoids the drawbacks of thermo-oxidative erosion that generates tritium as DTO, drawbacks that include the passivation of the oxygen gettering capacity of beryllium PFCs, conditioning time needed to remove oxygen and recover normal plasma operations, potential damage to in-vessel components, and the cost of

processing large quantities of DTO exhaust.<sup>280</sup> Interestingly, the temperature excursion of the codeposited layer was significantly higher than a bare graphite surface (2043 K compared to 1353 K), implying a much reduced thermal conductivity.<sup>269</sup> An interesting change in the surface morphology was observed after laser treatment of C-Be deposits on JET tiles. The previously uniform layer becomes broken up into submillimeter “globules,” suggesting melting of the beryllium component.<sup>269</sup>

High-power Nd lasers with fiber-optically coupled scanning heads are a proven technology in manufacturing. For a next-step device, we envisage a scaled-up system with a multikilowatt laser beam delivered by fiber optics on a robotic arm or mobile robot inside the vessel<sup>281</sup> (Fig. 39). Energetically, 30 MJ is needed to heat the top 100  $\mu\text{m}$  of a 50- $\text{m}^2$  codeposited area from 673 to 2273 K, and this corresponds to the output of a 3-kW laser for 3 h. Miniaturized scan heads could be used in

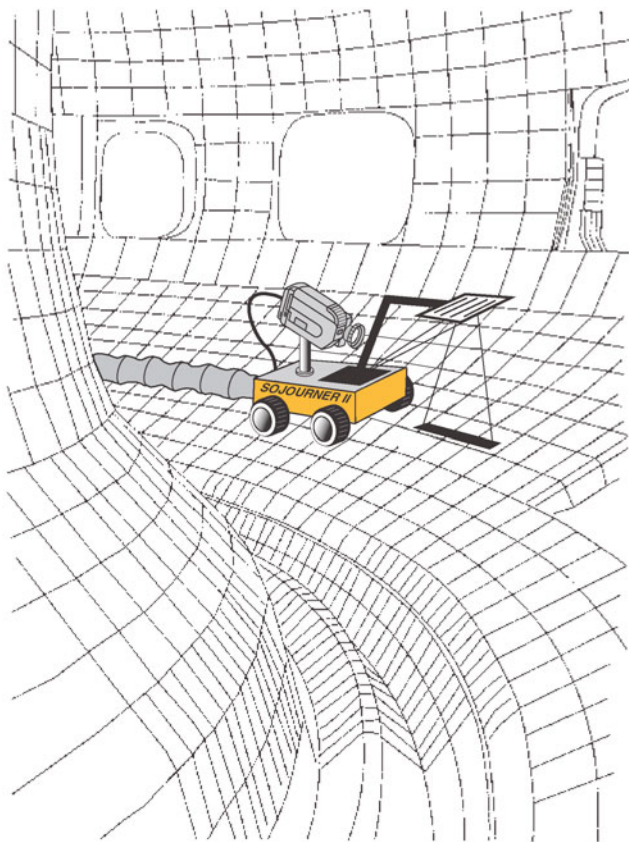


Fig. 39. Conceptual design of a detritiation robot inside a next-step tokamak. The umbilical cord contains a fiber optic that transmits an external laser beam to a scanning mirror. The laser beam is line focused onto the tile, rapidly heating the surface and releasing tritium. The design was inspired by the Sojourner robotic explorer deployed on Mars in 1997 (from Ref. 281 with kind permission of Springer Science and Business Media).

hard-to-access areas such as tile gaps. Clearly, much work remains to be done to develop this technique at an engineering scale; however, the results show that this technique appears to be a promising in situ method for tritium removal in a next-step D-T fusion device.

If oxygen is present, tritiated water may be released during laser desorption. Tritiated water is corrosive and needs special precautions in comparison with elemental tritium gas (see Sec. VI.A.1); in addition, tritiated water can be reabsorbed on tokamak walls and is commonly observed in thermal desorption measurements on samples kept in air. Experiments<sup>273,282</sup> with laser energies of 400, 230, and 70  $\text{mJ}/\text{cm}^2$ , which are well below the ablation threshold, demonstrated that after five pulses of 20-ns duration,  $\sim 90$ , 65, and 50% of deuterium was released from the TEXTOR bumper limiter tiles containing  $10^{22}$   $\text{D}/\text{m}^2$ . HD and  $\text{D}_2$  were observed in the residual gas; the HD apparently originated from residual water released under laser impact. HDO is also expected from residual water, and its absence in the quadrupole mass spectrometer (QMS) spectrum is attributed to its absorption on the walls of the ultrahigh vacuum ( $10^{-10}$ -mbar) system.

Additional experiments<sup>283</sup> with a 400  $\text{mJ}/\text{cm}^2$  laser beam were performed in vacuum,  $\text{H}_2$  gas environment (24 mbars), and  $\text{O}_2$  gas environment (2.4 and 24 mbars). It was found that HD and  $\text{D}_2$  components were very similar after laser pulses in vacuum, hydrogen, and low pressure of oxygen. After irradiation at high pressure of oxygen,  $\text{D}_2 + \text{HD}$  decreased by a factor of 2 to 3, while heavy water (HDO and  $\text{D}_2\text{O}$ ), which gave only a few percent of D release in vacuum and at low pressure of  $\text{O}_2$ , increased. Heavy water in this case can be formed during laser-induced dissociation of oxygen gas at high temperature. Though the increase of QMS water signals after laser shots in vacuum was small, its background increased from experiment to experiment. This can be interpreted as an indirect indication that heavy water was released during laser shots in vacuum, but it was absorbed by walls giving only a rise of the background. The absorption by walls was demonstrated in separate experiments where a water leak was arranged. The water signal rose with time to a steady-state level, and the delay time was  $\sim 30$  min in the system with a large wall surface but was only  $\sim 1$  min in a smaller system. More detailed experiments on measurements of mass spectra after laser impact are necessary.

#### VI.B.4. Detritiation by Laser Ablation

When removing tritium from thick codeposits such as may occur in ITER, it is advantageous to remove the films themselves, as this decreases the potential hazard posed by large accumulations of carbon dust in ITER. One detritiation method considered here is to use a laser in an SAR regime. Equipment for the detritiation of JET tiles by laser ablation within the JET Beryllium Handling

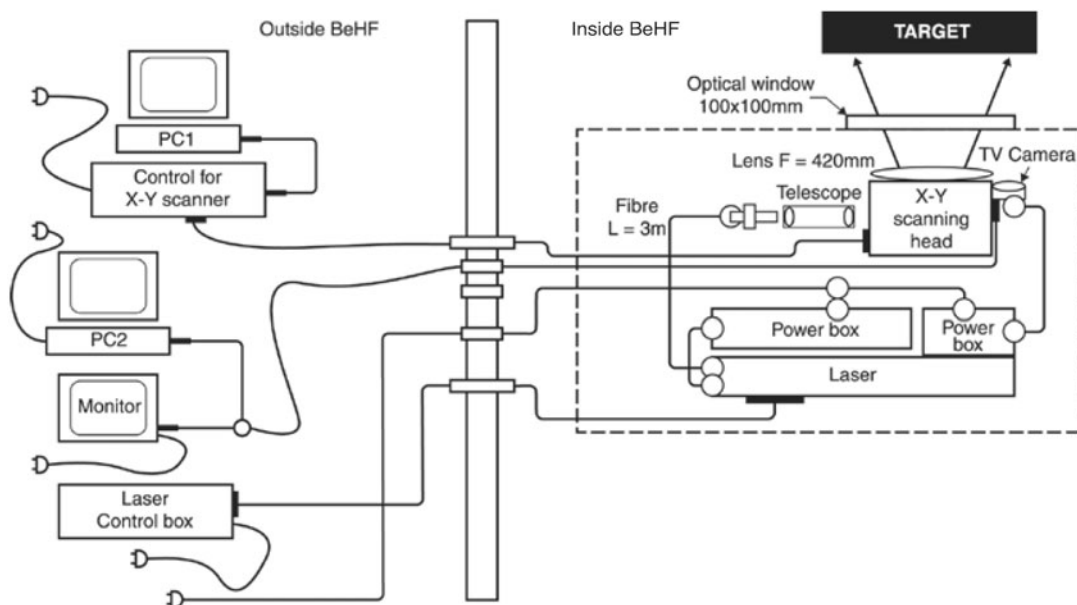


Fig. 40. Schematic of the equipment used inside and outside the BeHF during laser ablation experiments.

Facility (BeHF) has been developed at Commissariat à l'Énergie Atomique, Saclay.<sup>270</sup>

Tiles from the JET divertor were mounted on a stand in a slit box in the BeHF. The sealed box containing a laser, scanning mechanism, and viewing camera was wrapped in polyethylene and supported on a table so that the scanned beam could pass through an open slit into the slit box and illuminate the sample tile at normal incidence (Fig. 40). Sockets on the sealed box connected to the laser, etc., were connected via a bulwark plate in the BeHF wall to power supplies and drive units that could be operated from outside the BeHF. A Nd-YAG laser with a pulse energy of 1 mJ, a beam diameter of 100  $\mu\text{m}$ , a pulse length of 120 ns, and a repetition rate of 20 kHz was used.

A single scan was sufficient to completely change the appearance of the treated region; instead of the smooth film, the fiber planes of the CFC substrate were clearly visible.<sup>284</sup> In the case of three passes, the deposited film, which was up to 300  $\mu\text{m}$  thick in this region, was removed completely as shown by IBA, but some of the CFC substrate ( $\sim 10 \mu\text{m}$ ) had also been eroded as shown by the cross sections in Fig. 41. Note also the sharp edge to the treated region. The laser energy required for removal of substrate material is higher than that for removal of a codeposited film. Thus, by optimizing the laser energy, it would be possible to avoid any removal of substrate material, if this were necessary.

It is not clear in what form the film is removed by the laser (gas, particulates, etc.), as all the ablated material was swept from the slit box by the ventilation flow. Also, during the trials, less tritium release was recorded by the stack monitors than expected (e.g., an order of magnitude

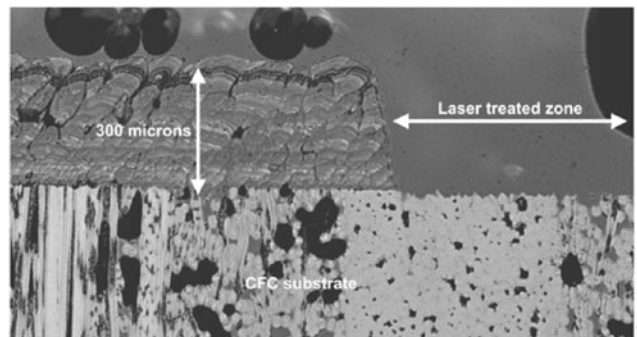


Fig. 41. Cross-section cut from a laser-treated CFC JET divertor tile at the edge of the laser-treated region (from Ref. 284).

less than observed during the flashlamp cleaning trials reported in Sec. VI.B.2); further work is in progress to elucidate these points. However, for ITER it is essential that the ablated material be removed from the machine. This may be done either by setting up a gas flow in the vicinity of the ablation or by treating divertor cassettes after removal from the vessel.

The laser was configured to scan over a maximum area of 500  $\times$  500  $\text{mm}^2$  with a limited effective depth of field. Alternative configurations are being developed that are more suitable for accessing difficult places, such as in the ITER divertor: Since the laser delivery is via a fiber-optic cable, there are no inherent limitations. The tests have shown that laser ablation is a possible technique for removing large areas of plasma-deposited layers.

## VI.C. Cleanup After Removal from the Tokamak

### VI.C.1. Gamma Irradiation of Flakes

A very large fraction of the tritium remaining in JET after the DTE1 campaign was found to be retained in flakes at the inner louvers. The flakes exhibit a layered structure and a D/C ratio ranging from 0.7 to 0.8 containing 96% carbon, 3% oxygen, and traces of various metals, mostly beryllium. The flakes were similar in composition and structure to the adherent deposited films on the sections of tiles shadowed from the plasma close to the louvers. A sample of these flakes was characterized at the hot cells of the Forschungszentrum Karlsruhe [Tritium Laboratory Karlsruhe (TLK)].

The physicochemical analysis at TLK revealed an average specific surface area of  $(4.7 \pm 0.3) \text{ m}^2 \cdot \text{g}^{-1}$  and a density of  $1.69 \pm 0.02 \text{ g} \cdot \text{cm}^{-3}$ , whereas their D/T ratio was estimated to be equal to 50 (Ref. 285). Their average tritium activity was also measured by calorimetry and was found to be  $1.17 \pm 0.1 \text{ TBq}$  per gram of flakes or 3.3 mg tritium per gram of flakes.

The flakes are naturally off-gassing, and over a storage period of 21 months at TLK, the average off-gassing rate was assessed to be 0.58 Ci ( $60 \mu\text{g} \cdot \text{T}$ ) per gram of flakes per month. Over a following period of 2 yr, the tritium off-gassing rate showed a slow decrease to reach the average value of 0.37 Ci/g per month. Under inert atmosphere the off-gassing rate rapidly decreases while the presence of moisture seems to speed up the off-gassing process.

This off-gassing behavior may be explained by a radiation-induced mechanism based on the tritium beta decay. After the tritium beta decay, the beta particle collides with the surrounding molecules and atoms and has sufficient energy (average 5.7 keV per beta) to produce multiple excitations, T-C bond breaking, and ionization of the surrounding molecules. One of the authors (NB) attempted, therefore, to enhance such a process by using an additional external irradiation, such as gamma irradiation.

After several months of irradiation at TLK under a gamma field generated by four  $^{57}\text{Co}$  sources, for a total dose of 3.5 Mrads, the off-gassed tritiated species released by the sample were tracked using a mass spectrometer and compared with the species released before irradiation. It was observed that the oxygen amount (mass 32) and the amount of CO or  $\text{C}_2\text{H}_4$  (mass 28) were similar before and after irradiation. It seems likely that it is the water presence that is responsible for the oxygen release and once the water is consumed, the oxygen amount released by the sample is diminished, the same way the tritium off-gassing rate of the flakes is diminished.

The gamma sources were not strong ( $\sim 6 \text{ krad/h}$ ), and the gamma irradiation did not enhance significantly the tritium off-gassing rate of the flakes. The reason is that the tritium content in the flakes ( $\sim 3 \text{ mg}$  tritium)

delivers a much higher dose than the gamma sources. In this regard 1 g of tritium delivers  $\sim 0.324 \text{ W/g}$  or 32 krad/s. Consequently, the dose rate delivered by the 1 g flakes (containing 3 mg tritium) is  $\sim 345 \text{ krad/h}$ , which is much higher than the 6 krad/h delivered by the three gamma sources. Moreover, the photoelectric effect generated by the gamma irradiation is very weak for low-Z (hydrocarbon) materials but increases for high-Z materials as a larger number of secondary electrons would be produced.

### VI.C.2. Thermal Release of Tritium from Carbon-Based Deposits

Thermal release studies of tritium from specimens from the plasma-exposed side of carbon tiles used in JET have already shown that heating the samples under moist air atmosphere, temperatures  $> 723 \text{ K}$  are required to release most of the tritium.<sup>140</sup> With a view to heating the samples at as high as possible temperatures in an inert gas, three samples from the inner divertor tile IN3 of JET were retrieved using the coring technique and heated up to 1373 K in helium containing 0.1 vol% hydrogen.

The samples were heated with a ramp rate of  $7 \text{ K} \cdot \text{min}^{-1}$  up to holding temperatures of 773, 823, and 873 K, and then after cooling down, the thermal treatment was repeated with a subsequent heating ramp rate of  $15 \text{ K} \cdot \text{min}^{-1}$  up to 1373 K. After having reached the final temperature, the sample was held at 1373 for 30 to 90 min. Several peaks were observed between 673 and 1273 K corresponding to the release of a number of various tritiated species. Typical thermal release results are shown in Fig. 42.

Heating the plasma-exposed sample IN3-Cy18-A1 at 773 K releases only part of the trapped tritium; all the tritium is released only after thermal treatment at 1373 K. Figure 42 clearly indicates that at least two types of hydrogen bonding are present in the codeposited layers. One type is "easily" broken at temperatures between 723 and 823 K; a second much stronger bond requires higher temperatures ( $\sim 1073 \text{ K}$ ) to break the bond and release the total amount of the contained tritium.

From this study<sup>140</sup> it appears that the gas-solid reactions taking place during the thermal treatment of a carbon sample are quite complicated and involve various tritiated hydrocarbon species having one or two carbon atoms in their structure. As the deuterium and tritium content for such compounds is very high, e.g., D/C  $\sim 0.75$ , such small chain hydrocarbons must exhibit mainly an  $sp^3$  hybridization. On the other hand, it has been reported that an  $sp^3$  H-C bond does not have the same energy as an  $sp^2$  H-C bond.<sup>286</sup> Indeed, the dissociation energy of the H-C bond increases as the  $p$  character of the carbon in the  $s$ - $p$  hybridization decreases. In other words, passing from an  $sp^3$  hybridization to  $sp^2$  and then to  $sp$ , the H-C bond becomes shorter and shorter and therefore stronger, requiring higher temperatures to break the bond.

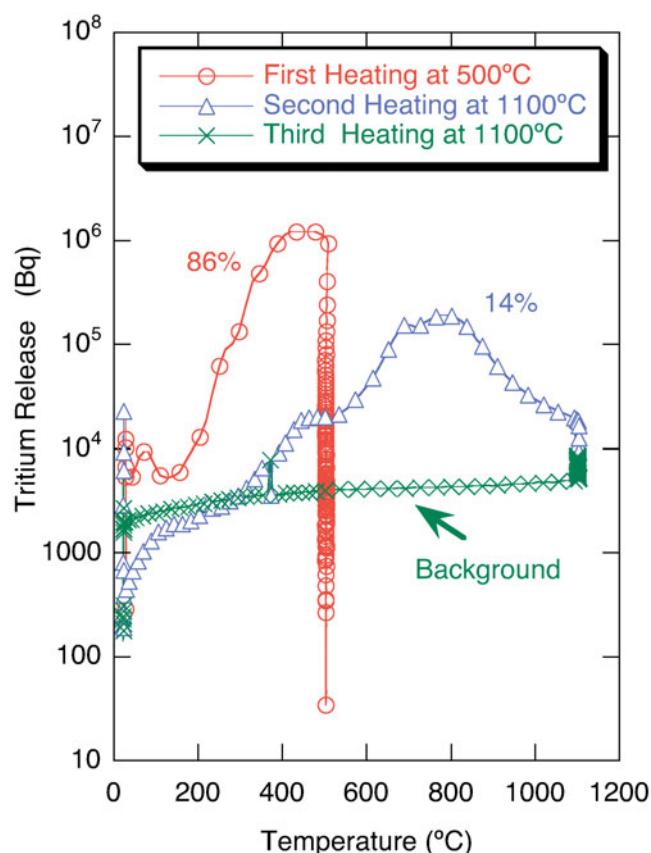


Fig. 42. Tritium release from the plasma-exposed JET sample IN3-Cyl8-A1 after three successive heat treatments under He gas exposure with 0.1% $H_2$ .

Accordingly, we attributed the first type of the released tritium (between 723 and 823 K) to the tritium diffused between the fibers and grains while the various observed peaks correspond to the various  $s$ - $p$  hybridizations of carbon in the T-C bonds. On the other hand, the second type of peaks, observed at higher temperature ( $\sim 1073$  K), has been attributed to tritium released after the intragranular diffusion.

A more detailed investigation<sup>287</sup> has shown that the presence of various peaks observed between 673 and 1073 K corresponds to the various alkyl, or isotopic, substitutions that the  $sp^3$  carbon can have.

### VI.C.3. Detritiation of Stainless Steel

Detritiation of stainless steel in wet atmosphere was investigated after saturation in T gas.<sup>288</sup> Release was found to be mainly in the form of HTO molecules. It was observed that Type 316 stainless steel with a thick technological oxide layer demonstrates rates of detritiation comparable to the rates predicted by a simple diffusion-limited mechanism of release. It was suggested that surface oxides promote water absorption and dissociation as

well as T-HO recombination and facilitate in this way detritiation of metals.

### VI.D. Detritiation Summary and Conclusions

There is no clear answer to date on the best way to control the in-vessel tritium inventory in ITER, which is likely to be concentrated in parts of the divertor structure difficult to access.<sup>3</sup> A method of reducing the inventory on a regular basis (e.g., overnight) without requiring the magnetic fields to be turned off, without affecting the torus vacuum, and without producing any hazardous waste would be the ideal solution. Oxygen gas will reach all parts of the machine, but efficient removal of codeposits will require the heating of some components of the divertor (where codeposits form) to temperatures  $\geq 573$  K. The reaction products of oxidation include tritiated water, which will require appropriate consideration in the design of the exhaust processing plant in ITER (Sec. VI.A.1). Oxygen treatment is relevant for the removal of carbon-based and mixed C-Be deposits. Laser technology may be used in situ during an extended outage (Sec. VI.B.3), but access to all appropriate regions of codeposition may be difficult. Laser-induced thermal desorption releases elemental tritium that can be pumped out. Laser ablation is very effective at removing thick deposits, assuming access is possible, but it leads to the release of particulates (Sec. VI.B.4).

Although the level of codeposition, or coimplantation, of H isotopes in beryllium-rich layers at room temperature is similar to that expected in carbon-rich codeposits, the concentration decreases much more rapidly with temperature in the former (as discussed in Sec. II.E). In addition, it is easier to remove the deuterium content at low temperature from beryllium-rich films than from carbon-rich films. This is shown in Fig. 43, where data from outgassing measurements of beryllium-rich codeposits<sup>289</sup> is replotted and compared to data from thermally desorbing carbon-rich codeposits.<sup>290</sup> For comparison the design value for the maximum bake temperature achievable in the ITER divertor after the coolant is drained from the divertor components is 650 K. Detritiation for ITER is thus critically dependent on final decisions regarding the first-wall composition and operating scenarios.

## VII. SUMMARY AND RECOMMENDATIONS

Designing a robust interface between a burning plasma and the material world poses severe challenges for future fusion reactors. The high stored energy and pulse duration in ITER coupled with the lack of experience in contemporary tokamaks with the proposed combination of plasma-facing materials makes the choice of these materials among the highest risk factors for ITER. The tritium inventory is a major source term in

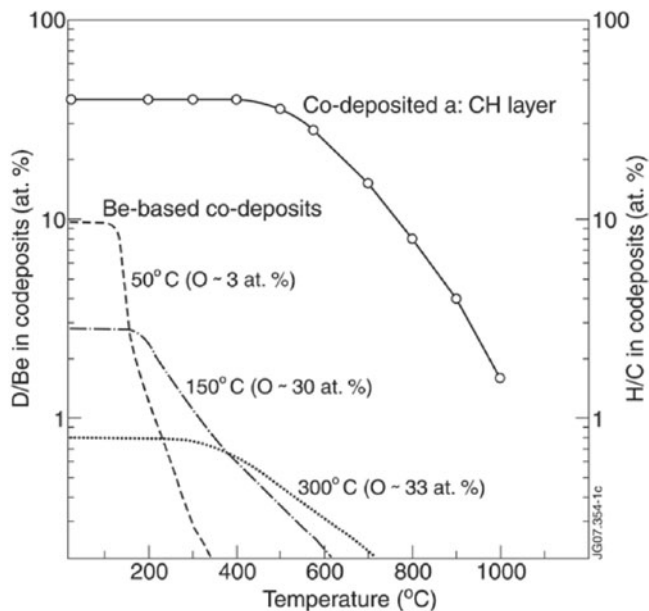


Fig. 43. Comparison of hydrogen isotope desorption characteristics from beryllium-based and carbon-based codeposits. Beryllium-based codeposit data are from Baldwin et al.<sup>289</sup> (the labels refer to the temperature and oxygen concentration during deposition). The co-deposited a:CH layer data are from Causey et al.<sup>290</sup>

accident scenarios, and erosion and tritium retention are decisive factors in material selection, licensing, and the future schedule of plasma operations. Advances in materials technology, especially in high-Z materials and in He cooling technology that will permit high wall temperatures, are essential parts of the long-term solution. This paper has presented recent results from research on plasma-facing materials proposed for ITER: Be, C, and W as well as mixtures of these materials with a special focus on tritium uptake and possible release mechanisms.

A key feature of beryllium is the development of connected porosity in material exposed to energetic hydrogen isotope ions. After extensive bombardment, an open honeycomb-type structure develops that extends beyond the particle range. The open porosity is an excellent getter of oxygen, and the affinity of hydrogen to metal oxides results in 0.3 to 0.4 H/Be tied at least partially to the oxide. This porosity growth can account for the strong pumping of hydrogen observed in tokamak discharges. After a discharge, the gas begins to escape from the porosity with a time constant of tens of seconds or can diffuse along grain boundaries deeper into the material. However, the oxide layer is expected to be very thin (nanometer-scale thickness), and hence, the hydrogenic retention in beryllium will still be dominated by codeposition of fuel atoms with either beryllium or carbon (if it is present).

Carbon has been a favored material for PFCs ever since the replacement of tungsten with carbon facilitated the first achievement of fusion-relevant temperatures in the PLT tokamak.<sup>291</sup> Carbon has excellent thermomechanical properties and low radiative cooling of the plasma because of its low-Z. The key issue for ITER is carbon's ability to trap tritium. Eroded C (atoms/molecules/radicals) can be transported in the plasma edge until they intercept solid surfaces where redeposition, in conjunction with H isotopes, can result in the continuous growth of tritium-containing codeposited layers. Full carbon machines such as JET and TFTR experienced tritium retention fractions that would be intolerable for ITER. Nevertheless, carbon is maintained as an option for limited areas of the ITER divertor target; however, its use will require frequent interventions for tritium removal. The formation of codeposited layers in tile gaps and tritium diffusion into the bulk material adds to the challenge. Tritium retention levels decrease with increasing temperature; however, the maximum bake temperature of ITER's PFCs is limited.

Hydrogen retention in tungsten is mainly controlled by hydrogen's low solubility and high diffusivity. In unirradiated tungsten, the diffusing hydrogen is trapped at intrinsic defects in the bulk. However, during deuterium ion irradiation or plasma exposure, the deuterium concentration in the implantation zone greatly exceeds the solubility limit and causes plastic deformation, leading to a sudden increase in trapping sites and the concurrent accumulation of deuterium, both in the form of D<sub>2</sub> molecules and D atoms, at depths of several micrometers. The amount of hydrogenic retention is temperature dependent. While the level of retention in unirradiated tungsten is expected to be lower than retention levels in Be- and C-containing codeposits, the creation of neutron-induced displacements/traps will increase the retention of hydrogen in tungsten. Experiments are currently underway to investigate this effect.

In general, one can predict that where carbon- and beryllium-containing mixed-material codeposits exist, there is a probability of finding large amounts of retained hydrogen isotopes. However, the amount of retention decreases with increasing temperature, as it does with mono-elemental materials. Although an extensive database exists on hydrogen retention, both from laboratory and tokamak experiments, predictions for what to expect in ITER are still problematic because of the relatively poor understanding of impurity creation rates and locations and uncertainties in material transport in the edge and SOL of toroidal plasmas.

Once the in-vessel tritium inventory in ITER approaches the administrative 700 g tritium limit,<sup>292</sup> plasma operations will have to cease, and the tritium will here to be removed by some means. The resulting availability of the machine for plasma operations will sensitively depend on the tritium accumulation rate, which in turn depends on the final selection of plasma-facing materials

(and the resulting mixed materials) as well as on the speed and efficiency of tritium removal. Candidate tritium removal techniques include passive removal by oxidation and active removal by surface heating or ablation. The lack so far of a demonstration of tritium removal at the required speed and efficiency from a contemporary tokamak with ITER's mix of materials poses risks for ITER's availability for plasma operations and makes tritium retention a decisive factor in the selection of ITER's plasma-facing materials.

The following topics are recommended for high-priority research and development:

1. determination of the effectiveness of tritium removal techniques from Be and BeO codeposits with carbon and tungsten impurities
2. quantification of the effect of ion- and neutron-induced damage on tritium trapping, permeation, and retention in tungsten
3. the capability to exchange components of ITER's first wall. This is critical if unacceptably high erosion or excessive tritium inventory occurs.
4. techniques of tritium and dust removal should not be pioneered on ITER. Candidate techniques should be validated in contemporary tokamaks; JET with its ITER-like wall materials is an attractive possibility.

#### ACKNOWLEDGMENTS

We would like to acknowledge the hospitality of the Atomic and Molecular Data Unit of the International Atomic Energy Agency (IAEA) in hosting the CRP meetings and its encouragement to collaborate in this area of research. The authors would like to thank G. Czechowicz for assistance with the figures. This work was supported in part by U.S. Department of Energy grant DE-AC02-76CH03073 and DE-FG02-07ER54912, International Science and Technology Center grant 2805, and IAEA contract 12138-ru. The financial support provided by the Natural Sciences and Engineering Research Council of Canada is gratefully acknowledged. Grant-in-aid of the Ministry of Education, Culture, Sports, Science and Technology—Japan for Scientific Research 17206092 and Scientific Research in Priority Area 461 (Tritium for Fusion) is gratefully acknowledged. Funding jointly by the U.K. Engineering and Physical Sciences Research Council and by the European Communities under the contract of Association between EUR-ATOM and U.K. Atomic Energy Authority is also acknowledged.

#### REFERENCES

1. "12th Meeting of the IFRC Subcommittee on Atomic and Molecular Data for Fusion," International Atomic Energy Agency Summary Report INDC(NDS)-420, available on the Internet at <http://www-nds.iaea.org/reports-new/indc-reports/indc-nds/indc-nds-0420.pdf> (2000).

2. G. FEDERICI and C. H. SKINNER, "Tritium Inventory in the Materials of the ITER Plasma Facing Components," *Nuclear Fusion Research—Understanding Plasma-Surface Interactions*, Vol. 78, p. 287, D. REITER and R. E. H. CLARK, Eds., in *Springer-Verlag Series in Chemical Physics*, Springer Verlag, Heidelberg (2005).

3. G. FEDERICI et al., "Plasma-Material Interactions in Current Tokamaks and Their Implications for Next Step Fusion Reactors," *Nucl. Fusion*, **41**, 1967 (2001).

4. R. A. CAUSEY, "Hydrogen Isotope Retention and Recycling in Fusion Reactor Plasma-Facing Components," *J. Nucl. Mater.*, **300**, 91 (2002).

5. A. A. HAASZ and J. W. DAVIS, "Hydrogen Retention in and Release from Carbon Materials," *Nuclear Fusion Research, Springer-Verlag Series in Chemical Physics*, p. 225, R. E. H. CLARK and D. H. REITER, Eds., Springer Verlag, Heidelberg, Germany (2005).

6. C. H. SKINNER, J. P. COAD, and G. FEDERICI, "Tritium Removal from Carbon Plasma Facing Components," *Phys. Scripta*, **T111**, 92 (2004).

7. G. FEDERICI, J. N. BROOKS, M. ISELI, and C. H. WU "In-Vessel Tritium Retention and Removal in ITER-FEAT," *Phys. Scripta*, **T91**, 76 (2001).

8. J. W. DAVIS and A. A. HAASZ, "Overview of Thermo-Oxidation of Tokamak Codeposits," *Phys. Scripta*, **T91**, 33 (2001).

9. G. F. COUNSELL and C. H. WU, "In-Situ Detection and Removal of Carbon Debris—A Challenge for Next Step Fusion Devices," *Phys. Scripta*, **T91**, 70 (2001).

10. *J. Nucl. Mater.*, **363–365** (2007).

11. A. LOARTE et al., "A New Look at JET Operation with Be as a Plasma Facing Material," *J. Nucl. Mater.*, **337–339**, 816 (2005).

12. A. A. PISAREV, "Tritium Solubility and Diffusivity in Beryllium," *Fusion Technol.*, **28**, 1262 (1995).

13. P. M. S. JONES and R. GIBSON, "Hydrogen in Beryllium," *J. Nucl. Mater.*, **21**, 353 (1967).

14. W. A. SWANSIGER, "Summary Abstract: Tritium Solubility in High Purity Beryllium," *J. Vac. Sci. Technol. A*, **4**, 3, 1216 (1986).

15. V. I. SHAPOVALOV and Y. M. DUKEL'SKII, "The Beryllium-Hydrogen Phase Diagram," *Izv. Akad. Nauk SSSR Metally*, **5**, 201 (1988).

16. E. ABRAMOV, M. P. RIEHM, and D. A. THOMSON, "Deuterium Permeation and Diffusion in High-Purity Beryllium," *J. Nucl. Mater.*, **175**, 90 (1990).

17. I. L. TAZHIBAIEVA et al., "Deuterium Permeation Through Beryllium with Surface Element Control," *Proc. 18th Symp. Fusion Technology*, Karlsruhe, Germany, August 22–26, 1994, Vol. 1, p. 427 (1994).

18. D. A. THOMPSON and R. G. MACAULAY-NEWCOMBE, "Deuterium Absorption and Desorption in Potential Fusion Reactor Materials," CFFTP Annual Report I-9425, Canadian Fusion Fuels Technology Project (1994).
19. D. A. THOMPSON and R. G. MACAULAY-NEWCOMBE, "Solubility, Diffusion, and Desorption of Hydrogen Isotopes in Beryllium and Tungsten," ITER Task T227 (1996); see also CFFTP Report G-9711, Canadian Fusion Fuels Technology Project (1997).
20. R. M. AL'TOVSKIY et al., "Hydrogen Permeability of Beryllium," *Russian Metall.*, **3**, 51 (1981).
21. R. A. ANDERL et al., "Hydrogen Transport Behavior of Beryllium," *J. Nucl. Mater.*, **196-198**, 986 (1992).
22. R. A. CAUSEY et al., "Tritium Retention and Migration in Beryllium," *J. Nucl. Mater.*, **176-177**, 654 (1990).
23. R. A. ANDERL et al., "Hydrogen Isotope Retention in Beryllium for Tokamak Plasma Facing Applications," *J. Nucl. Mater.*, **273**, 1 (1999).
24. R. A. LANGLEY, "Interaction of Implanted Deuterium and Helium with Beryllium: Radiation Enhanced Oxidation," *J. Nucl. Mater.*, **85-86**, 1123 (1979).
25. W. R. WAMPLER, "Retention and Thermal Release of Deuterium Implanted in Beryllium," *J. Nucl. Mater.*, **122-123**, 1598 (1984).
26. W. MOLLER, N. M. U. SCHERZER, and J. BOHDANSKY, "Retention and Release of Deuterium Implanted into Beryllium," IPP-JET Report 26 (1985).
27. W. R. WAMPLER, "Trapping of Deuterium in Beryllium," *J. Nucl. Mater.*, **196-198**, 981 (1992).
28. A. A. HAASZ and J. W. DAVIS, "Deuterium Retention in Beryllium, Molybdenum and Tungsten at High Fluences," *J. Nucl. Mater.*, **241-243**, 1076 (1997).
29. N. YOSHIDA, S. MIZUSAWA, R. SAKAMOTO, and T. MUROGA, "Radiation Damage and Deuterium Trapping in Deuterium Ion Injected Beryllium," *J. Nucl. Mater.*, **233-237**, 874 (1996).
30. H. D. FALTER, D. CIRIC, J. P. COAD, and D. GODDEN, "Deuterium Implantation in Actively Cooled Beryllium Monoblocks," JET Report R(97)03 (1997).
31. R. G. MACAULAY-NEWCOMBE, D. A. THOMPSON, and W. W. SMELTZER, "Deuterium Diffusion, Trapping, and Release in Ion-Implanted Beryllium," *Fusion Eng. Des.*, **18**, 419 (1991).
32. W. L. HSU et al., "Transient Release of Deuterium from Beryllium after Plasma Ion Implantation," *J. Nucl. Mater.*, **176-177**, 218 (1990).
33. R. A. CAUSEY, G. R. LONGHURST, and W. HARBIN, "Tritium Retention in S-65 Beryllium After 100 eV Plasma Exposure," *J. Nucl. Mater.*, **241-243**, 1041 (1997).
34. R. P. DOERNER, A. GROSSMAN, S. LUCKHARDT, R. SERAYDARIAN, F. C. SZE, and D. G. WHYTE, "Response of Beryllium to Deuterium Plasma Bombardment," *J. Nucl. Mater.*, **257**, 51 (1998).
35. V. M. SHARAPOV, L. E. GAVRILOV, V. S. KULIKAVKAS, and A. V. MARKIN, "Deuterium Accumulation in Beryllium in Contact with Atomic Deuterium at 740 K," *J. Nucl. Mater.*, **233-237**, 870 (1996).
36. V. N. CHERNIKOV et al., "Gas-Induced Swelling of Beryllium Implanted with Deuterium Ions," *J. Nucl. Mater.*, **233-237**, 860 (1996).
37. V. K. ALIMOV, V. N. CHERNIKOV, and A. P. ZAKHAROV, "Depth Distribution of Deuterium Atoms and Molecules in Beryllium Implanted with D Ions," *J. Nucl. Mater.*, **241-243**, 1047 (1997).
38. A. V. MARKIN, V. N. CHERNIKOV, S. Y. RYBAKOV, and A. P. ZAKHAROV, "Thermal Desorption of Deuterium Implanted in Beryllium," *J. Nucl. Mater.*, **233-237**, 865 (1996).
39. M. MAYER, "Codeposition of Deuterium with BeO at Elevated Temperatures," *J. Nucl. Mater.*, **240**, 164 (1997).
40. R. A. CAUSEY and D. S. WALSH, "Codeposition of Deuterium with Beryllium: Letter to the Author," *J. Nucl. Mater.*, **254**, 84 (1998).
41. M. J. BALDWIN, K. SCHMID, R. P. DOERNER, A. WILTNER, R. SERAYDARIAN, and C. LINSMEIER, "Composition and Hydrogen Isotope Retention Analysis of Co-Deposited C/Be Layers," *J. Nucl. Mater.*, **337-339**, 590 (2005).
42. G. SAIBENE et al., "Hydrogen Recycling Coefficient in Beryllium," *J. Nucl. Mater.*, **176-177**, 618 (1990).
43. R. SARTORI et al., "Deuterium Release Measurements in the Be Phase of JET and Determination of Tritium Content in the Exhaust Gas," *J. Nucl. Mater.*, **176-177**, 624 (1990).
44. J. EHRENBERG et al., "Analysis of Deuterium Recycling in JET Under Beryllium First Wall Conditions," *J. Nucl. Mater.*, **176-177**, 226 (1990).
45. P. ANDREW and M. PICK, "Hydrogen Retention in the First Wall," *J. Nucl. Mater.*, **220-222**, 601 (1994).
46. W. ECKSTEIN, "Physical Sputtering and Radiation-Enhanced Sublimation," *Physical Processes of the Interaction of Fusion Plasmas with Solids*, p. 93, W. O. HOFER and J. ROTH, Eds., Academic Press, Amsterdam, Netherlands (1996).
47. W. ECKSTEIN et al., "Particle Induced Erosion of Be, C and W in Fusion Plasmas, Part B: Physical Sputtering and Radiation-Enhanced Sublimation," *Atomic and Plasma-Material Interaction Data for Fusion*, Vol. 7B, International Atomic Energy Agency, Vienna (2001).
48. E. VIETZKE and A. A. HAASZ, "Chemical Erosion," *Physical Processes of the Interaction of Fusion Plasmas with Solids*, p. 135, W. O. HOFER and J. ROTH, Eds., Academic Press, Amsterdam, Netherlands (1996).

49. A. A. HAASZ, J.A. STEPHENS, E. VIETZKE, W. ECKSTEIN, J. W. DAVIS, and Y. HIROOKA., "Particle-Induced Erosion of Be, C and W in Fusion Plasmas, Part A: Chemical Erosion of Carbon-Based Materials," *Atomic and Plasma-Material Interaction Data for Fusion*, Vol. 7A, International Atomic Energy Agency, Vienna (1998).
50. A. A. HAASZ and J. W. DAVIS, "Erosion of Carbon in Dual-Beam Experiments: An Overview," *Phys. Scripta*, **111**, 68 (2004).
51. A. A. HAASZ, P. FRANZEN, J. W. DAVIS, S. CHIU, and C. S. PITCHER, "Two-Region Model for Hydrogen Trapping in and Release from Graphite," *J. Appl. Phys.*, **77**, 66 (1995).
52. S. CHIU and A. A. HAASZ, "Molecule Formation due to Sequential and Simultaneous Exposure of Graphite to H<sup>+</sup> and D<sup>+</sup>," *J. Nucl. Mater.*, **196–198**, 972 (1992).
53. W. N. REYNOLDS, *Physical Properties of Graphite*, Elsevier, Amsterdam (1968).
54. R.-D. PENZHORN et al., "Tritium Depth Profiles in Graphite and Carbon Fibre Composite Material Exposed to Tokamak Plasmas," *J. Nucl. Mater.*, **288**, 170 (2001).
55. R. A. CAUSEY, M. I. BASKES, and K. L. WILSON, "The Retention of Deuterium and Tritium in POCO AXF-5Q Graphite," *J. Vac. Sci. Technol.*, **A4**, 1189 (1986).
56. J. ROTH et al., "Deuterium Retention in Carbon Fibre Composites NB31 and N11 Irradiated with Low-Energy D Ions," *J. Nucl. Mater.*, **363–365**, 822 (2007).
57. P. HUCKS, K. FLASKAMP, and E. VIETZKE, "The Trapping of Thermal Atomic Hydrogen on Pyrolytic Graphite," *J. Nucl. Mater.*, **93–94**, 558 (1980).
58. P. C. STANGEBY, O. AUCIELLO, A. A. HAASZ, and B. L. DOYLE, "Trapping of Sub-eV Hydrogen and Deuterium Atoms in Graphite," *J. Nucl. Mater.*, **122&123**, 1592 (1984).
59. V. CHERNIKOV, A.E. GORODETSKY, S. L. KANASHENKO, A. P. ZAKHAROV, W. R. WAMPLER, and B. L. DOYLE, "Trapping of Deuterium in Boron and Titanium Modified Graphites Before and After Carbon Ion Irradiation," *J. Nucl. Mater.*, **217**, 250 (1994).
60. R. C. BANSAL, F. J. VASTOLA, and P. L. WALKER Jr., "Studies on Ultra-Clean Carbon Surfaces—III. Kinetics of Chemisorption of Hydrogen on Graphon," *Carbon*, **9**, 185 (1990).
61. R. A. STREHLOW, "Chemisorption of Tritium on Graphites at Elevated Temperature," *J. Vac. Sci. Technol. A*, **4**, 1183 (1986).
62. R. A. CAUSEY, "The Interaction of Tritium with Graphite and Its Impact on Tokamak Operations," *J. Nucl. Mater.*, **162–164**, 151 (1989).
63. H. ATSUMI, S. TOKURA, and M. MIYAKE, "Absorption and Desorption of Deuterium on Graphite at Elevated Temperatures," *J. Nucl. Mater.*, **155–157**, 241 (1988).
64. R. A. CAUSEY, T. S. ELLEMAN, and K. VERGHESE, "Hydrogen Diffusion and Solubility in Pyrolytic Carbon," *Carbon*, **17**, 323 (1979).
65. H. D. ROHRIG, P. G. FISCHER, and R. HECKER, "Tritium Balance in High-Temperature Gas-Cooled Reactors," *J. Am. Ceram. Soc.*, **59**, 316 (1976).
66. V. MALKA, H. D. ROHRIG, and R. HECKER, "Investigations on Sorption and Diffusion of Tritium in HTGR-Graphite," *Proc. Conf. Tritium Technology in Fission, Fusion, and Isotope Applications*, 1980, p. 102.
67. J. W. DAVIS, A. A. HAASZ, and P. C. STANGEBY, "Hydrocarbon Formation due to Combined H<sup>+</sup> Ion and H<sup>0</sup> Atom Impact on Pyrolytic Graphite," *J. Nucl. Mater.*, **155–157**, 234 (1988).
68. A. A. HAASZ and J. W. DAVIS, "Comparison of the Chemical Erosion of Carbon/Carbon Composites and Pyrolytic Graphite," *J. Nucl. Mater.*, **175**, 84 (1990).
69. J. W. DAVIS and A. A. HAASZ, "Chemical Erosion of Carbon/Carbon Composites Doped with Boron and Silicon," *J. Nucl. Mater.*, **195**, 166 (1992).
70. B. V. MECH, A. A. HAASZ, and J. W. DAVIS, "Isotopic Effects in Hydrocarbon Formation due to Low-Energy H<sup>+</sup>/D<sup>+</sup> Impact on Graphite," *J. Nucl. Mater.*, **255**, 153 (1998).
71. E. SALONEN, K. NORDLUND, J. KEINONEN, and C. H. WU, "Swift Chemical Sputtering of Amorphous Hydrogenated Carbon," *Phys. Rev. B*, **63**, 195415 (2001).
72. L. I. VERGARA et al., "Methane Production from ATJ Graphite by Slow Atomic and Molecular D Ions: Evidence for Projectile Molecule-Size-Dependent Yields at Low Energies," *J. Nucl. Mater.*, **357**, 9 (2006).
73. R. G. MACAULAY-NEWCORBE, A. A. HAASZ, and J. W. DAVIS, "Low-Energy Tritium Ion Erosion of Graphite," *J. Nucl. Mater.*, **337–339**, 857 (2005).
74. B. V. MECH, A. A. HAASZ, and J. W. DAVIS, "Model for the Chemical Erosion of Graphite due to Low-Energy H<sup>+</sup> and D<sup>+</sup> Impact," *J. Appl. Phys.*, **84**, 1655 (1998).
75. A. A. HAASZ and J. W. DAVIS, "Hydrogen Isotope Effects on the Erosion of Carbon," *Fusion Sci. Technol.*, **50**, 58 (2006).
76. M. BALDEN and J. ROTH, "New Weight-Loss Measurements of the Chemical Erosion Yields of Carbon Materials Under Hydrogen Ion Bombardment," *J. Nucl. Mater.*, **280**, 39 (2000).
77. W. ECKSTEIN, C. GARCIA-ROSALES, J. ROTH, and W. OTTENBERGER, "Sputtering Data," IPP Garching Report IPP 9/82, Max-Planck-Institut für Plasmaphysik (1993).
78. S. J. STUART, P. S. KRSTIC, T. A. EMBRY, and C. O. REINHOLD, "Methane Production by Deuterium Impact at Carbon Surfaces," *Nucl. Instrum. Methods B*, **255**, 202 (2007).

79. C. HOPF, A. VON KEUDEL, and W. JACOB, "Chemical Sputtering of Hydrocarbon Films," *J. Appl. Phys.*, **94**, 2373 (2003).
80. D. G. WHYTE et al., "Reduction of Divertor Carbon Sources in DIII-D," *J. Nucl. Mater.*, **290–293**, 356 (2001).
81. G. M. WRIGHT, A. A. HAASZ, J. W. DAVIS, and R. G. MACAULAY-NEWCORBE, "Chemical Erosion of DIII-D Lower Divertor Tiles," *J. Nucl. Mater.*, **337–339**, 74 (2005).
82. J. P. COAD, M. RUBEL, and C. H. WU, "The Amount and Distribution of Deuterium Retained in the JET Divertor After the C and Be Phases in 1994–95," *J. Nucl. Mater.*, **241–243**, 408 (1997).
83. J. P. COAD et al., "Evidence for Impurity Drift in the Scrape-Off Layer of JET," *Europhysics Conference Abstracts: Controlled Fusion and Plasma Physics*, Maastricht, Holland, June 14–18, 1999, Vol. 23J, p. 53, European Physical Society (1999).
84. J. P. COAD et al., "Erosion/Deposition Issues at JET," *J. Nucl. Mater.*, **290–293**, 224 (2001).
85. J. P. COAD et al., "Overview of Material Re-Deposition and Fuel Retention Studies at JET with the Gas Box Divertor," *Nucl. Fusion*, **46**, 350 (2006).
86. J. P. COAD et al., "Erosion and Deposition in the JET MkII-SRP Divertor," *J. Nucl. Mater.*, **363–365**, 287 (2007).
87. M. MAYER, R. BEHRISCH, K. PLAMANN, P. L. ANDREW, J. P. COAD, and A. T. PEACOCK, "Wall Erosion and Material Transport to the Mark I Carbon Divertor of JET," *J. Nucl. Mater.*, **266–269**, 604 (1999).
88. J. P. COAD et al., "Erosion/Deposition in JET During the Period 1999–2001," *J. Nucl. Mater.*, **313–316**, 419 (2003).
89. H.-G. ESSER et al., "Effect of Plasma Configuration on Carbon Migration Measured in the Inner Divertor of JET Using Quartz Microbalance," *J. Nucl. Mater.*, **337–339**, 84 (2005).
90. G. F. MATTHEWS et al., "Material Migration in JET," *Europhysics Conference Abstracts: Controlled Fusion and Plasma Physics*, St. Petersburg, Russia, July 7–11, 2003, Vol. 27A, P-3.198, European Physical Society (2003).
91. K. KRIEGER et al., "Erosion and Migration of Tungsten Employed at the Central Column Heat Shield of ASDEX Upgrade," *J. Nucl. Mater.*, **307–311**, 139 (2002).
92. T. PÜTTERICH et al., "Carbon Influx Studies in the Main Chamber of ASDEX Upgrade," *Plasma Phys. Control. Fusion*, **45**, 1873 (2003).
93. R. DUX et al., "Tungsten Erosion at the ICRH Limiters in ASDEX Upgrade," *J. Nucl. Mater.*, **363–365**, 112 (2007).
94. M. MAYER et al., "Carbon Erosion and Migration in Fusion Devices," *Phys. Scripta*, **T111**, 55 (2004).
95. M. MAYER et al., "Carbon Erosion and Deposition on the ASDEX Upgrade Divertor Tiles," *J. Nucl. Mater.*, **337–339**, 119 (2005).
96. M. MAYER et al., "Erosion of Tungsten and Carbon Markers in the Outer Divertor of ASDEX-Upgrade," *Phys. Scripta*, **T128**, 106 (2007).
97. A. KALLENBACH et al., "Spectroscopic Investigation of Carbon Migration with Tungsten Walls in ASDEX Upgrade," *J. Nucl. Mater.*, **363–365**, 60 (2007).
98. M. MAYER, V. ROHDE, A. VON KEUDEL, and ASDEX-UPGRADE TEAM, "Characterisation of Deposited Hydrocarbon Layers Below the Divertor and in the Pumping Ducts of ASDEX Upgrade," *J. Nucl. Mater.*, **313–316**, 429 (2003).
99. M. MAYER, V. ROHDE, and ASDEX-UPGRADE TEAM, "Further Insight into the Mechanism of Hydrocarbon Layer Formation Below the Divertor of ASDEX Upgrade," *Nucl. Fusion*, **46**, 914 (2006).
100. K. KRIEGER et al., "Formation of Deuterium-Carbon Inventories in Gaps of Plasma Facing Components," *J. Nucl. Mater.*, **363–365**, 870 (2007).
101. V. ROHDE, M. MAYER, J. LIKONEN, R. NEU, T. PÜTTERICH, and E. VAINONEN-AHLGREN, "Carbon Erosion and a:C-H Layer Formation at ASDEX Upgrade," *J. Nucl. Mater.*, **337–339**, 847 (2005).
102. W. JACOB, "Redeposition of Hydrocarbon Layers in Fusion Devices," *J. Nucl. Mater.*, **337–339**, 839 (2005).
103. M. MAYER et al., "Hydrogen Inventories in Nuclear Fusion Devices," *J. Nucl. Mater.*, **290–293**, 381 (2001).
104. C. H. SKINNER et al., "Studies of Tritiated Co-Deposited Layers in TFTR," *J. Nucl. Mater.*, **290–293**, 486 (2001).
105. G. HAAS, R. MAINGI, J. NEUHAUSER, ASDEX-UPGRADE TEAM, and DIII-D TEAM, "Dynamic Retention in the Walls of the Tokamaks ASDEX Upgrade and DIII-D," *J. Nucl. Mater.*, **266–269**, 1065 (1999).
106. W. R. WAMPLER, "Ion Beam Analysis for Fusion Energy Research," *Nucl. Instrum. Methods B*, **219–220**, 836 (2004).
107. J. E. MENARD et al., "Overview of Recent Physics Results from the National Spherical Torus Experiment (NSTX)," *Nucl. Fusion*, **47**, S645 (2007).
108. C. H. SKINNER, H. KUGEL, A. L. ROQUEMORE, J. HOGAN, W. R. WAMPLER, and NSTX TEAM, "Time-Resolved Deposition Measurements in NSTX," *J. Nucl. Mater.*, **337–339**, 129 (2005).
109. C. H. SKINNER et al., "Pulse-by-Pulse Measurements of Dynamic Retention and Deposition in NSTX," *J. Nucl. Mater.*, **363–365**, 247 (2007).
110. K. SUGIYAMA, T. TANABE, K. MASAKI, and N. MIYA, "Tritium Distribution Measurement of the Tile Gap of JT-60U," *J. Nucl. Mater.*, **367–370**, 1248 (2007).

111. K. MASAKI et al., "Retention Characteristics of Hydrogen Isotopes in JT-60U," *J. Nucl. Mater.*, **337–339**, 553 (2005).
112. T. TANABE et al., "Tritium Retention and Carbon Deposition on Plasma Facing Materials," *J. Nucl. Mater.*, **345**, 89 (2005).
113. T. SHIBAHARA et al., "Hydrogen Isotope Retention of JT-60U W-Shaped Divertor Tiles Exposed to DD Discharges," *J. Nucl. Mater.*, **356**, 115 (2006).
114. Y. GOTOH et al., "Long-Term Erosion and Re-Deposition of Carbon in the Divertor Region of JT-60U," *J. Nucl. Mater.*, **356**, 138 (2006).
115. K. SUGIYAMA et al., "Ion Beam Analysis of H and D Retention in the Near Surface Layers of JT-60U Plasma Facing Wall Tiles," *J. Nucl. Mater.*, **363–365**, 949 (2007).
116. J. P. SHARPE et al., "Characterization of Dust Collected from NSTX and JT-60U," *J. Nucl. Mater.*, **337–339**, 1004 (2005).
117. H. TAKENAGA et al., "Study of Global Wall Saturation Mechanisms in Long-Pulse ELMy H-Mode Discharges on JT-60U," *Nucl. Fusion*, **46**, S39 (2006).
118. K. MASAKI et al., "Tritium Distribution in JT-60U W-Shaped Divertor," *J. Nucl. Mater.*, **313–316**, 514 (2003).
119. T. TANABE, "On the Possibility of ITER Starting with Full Carbon," *Fusion Eng. Des.*, **81**, 139 (2006).
120. T. TANABE et al., "Imaging Plate Technique for Determination of Tritium Distribution of Graphite Tiles of JT-60U," *J. Nucl. Mater.*, **307–311**, 1441 (2002).
121. P. WIENHOLD et al., "Investigation of Carbon Transport in the Scrape-Off Layer of TEXTOR-94," *J. Nucl. Mater.*, **290–293**, 362 (2001).
122. A. KRETER et al., "Investigation of Carbon Transport by  $^{13}\text{CH}_4$  Injection Through Graphite and Tungsten Test Limiters in TEXTOR," *Plasma Phys. Control. Fusion*, **48**, 1401 (2006).
123. J. LIKONEN et al., "Studies of Impurity Deposition/Implantation in JET Divertor Tiles Using SIMS and Ion Beam Techniques," *Fusion Eng. Des.*, **66–68**, 219 (2003).
124. Y. NOBUTA et al., "Deposition and Transport of  $^{13}\text{C}$  from Methane Injection into Outer Divertor Plasma in JT-60U," *Europhysics Conference Abstracts: 34th Conf. Plasma Physics*, Warsaw, Poland, July 2–6, 2007, Vol. 31F, p. P-1.024, European Physical Society (2007).
125. E. VAINONEN-AHLGREN et al., "Studies on  $^{13}\text{C}$  Deposition in ASDEX Upgrade," *J. Nucl. Mater.*, **337–339**, 55 (2005).
126. S. L. ALLEN et al., " $^{13}\text{C}$  Transport Studies in L-Mode Divertor Plasmas on DIII-D," *J. Nucl. Mater.*, **337–339**, 30 (2005).
127. W. R. WAMPLER et al., "Measurements of Carbon, Deuterium and Boron Deposition in DIII-D," *J. Nucl. Mater.*, **337–339**, 134 (2005).
128. W. R. WAMPLER et al., "Transport and Deposition of  $^{13}\text{C}$  from Methane Injection into Partially Detached H-Mode Plasmas in DIII-D," *J. Nucl. Mater.*, **363–365**, 72 (2007).
129. J. D. ELDER et al., "OEDGE Modeling of the DIII-D H-Mode  $^{13}\text{CH}_4$  Puffing Experiment," *J. Nucl. Mater.*, **363–365**, 140 (2007).
130. A. G. McLEAN et al., "Spectroscopic Characterization and Simulation of Chemical Sputtering Using the DiMES Porous Plug Injector in DIII-D," *J. Nucl. Mater.*, **363–365**, 86 (2007).
131. A. G. McLEAN et al., "Characterization of Chemical Sputtering Using the Mark II DiMES Porous Plug Injector in Attached and Detached Divertor Plasmas of DIII-D," presented at 18th Int. Conf. Plasma Surface Interactions, Toledo, Spain, May 26–30, 2008, *J. Nucl. Mater.* (submitted for publication).
132. B. L. DOYLE, W. R. WAMPLER, D. K. BRICE, and S. T. PICRAUX, "Saturation and Isotopic Replacement of Deuterium in Low-Z Materials," *J. Nucl. Mater.*, **93–94**, 551 (1980).
133. G. STAUDENMAIER et al., "Trapping of Deuterium Implanted in Carbon and Silicon: A Calibration for Particle-Energy Measurements in the Plasma Boundary of Tokamaks," *J. Nucl. Mater.*, **84**, 149 (1979).
134. A. A. HAASZ and J. W. DAVIS, "Fluence Dependence of Deuterium Trapping in Graphite," *J. Nucl. Mater.*, **209**, 155 (1994).
135. M. BALDEN et al., "Deuterium Retention by Implantation in Carbide-Doped Graphites," *Phys. Scripta*, **T102**, 38 (2003).
136. A. A. HAASZ and J. W. DAVIS, "Deuterium Retention in Doped Graphites," *J. Nucl. Mater.*, **232**, 219 (1996).
137. J. W. DAVIS, A. A. HAASZ, and D. S. WALSH, "Flux and Fluence Dependence of  $\text{H}^+$  Trapping in Graphite," *J. Nucl. Mater.*, **176&177**, 992 (1990).
138. V. Kh. ALIMOV and J. ROTH, "Hydrogen Isotope Retention in Plasma-Facing Materials: Review of Recent Experimental Results," *Phys. Scripta*, **T128**, 6 (2007).
139. B. EMMOTH, M. RUBEL, and E. FRANCONI, "Deep Penetration of Deuterium in Carbon Based Substrates Exposed to PISCES-A Plasma," *Nucl. Fusion*, **30**, 1140 (1990).
140. R.-D. PENZHORN et al., "Tritium in Plasma Facing Components," *Fusion Eng. Des.*, **56&57**, 105 (2001).
141. N. BEKRIS et al., "Tritium Depth Profiles in 2D and 4D CFC Tiles from JET and TFTR," *J. Nucl. Mater.*, **313–316**, 501 (2003).
142. J. ROTH et al., "Trapping, Detrapping and Replacement of keV Hydrogen Implanted into Graphite," *J. Nucl. Mater.*, **93&94**, 601 (1980).
143. J. BUCALOSSO et al., "Deuterium In-Vessel Retention Characterisation Through the Use of Particle Balance on Tore Supra," *J. Nucl. Mater.*, **363–365**, 759 (2007).

144. A. PISAREV et al., "Thermal Desorption of Deuterium from Graphite After Ion Implantation, Plasma Impact, and Exposure in Gas," presented at 17th Int. Vacuum Congress, Stockholm, Sweden, July 2–6, 2007, Rep. PSTF07-Or2.
145. R. SARTORI, G. SAIBENE, D. H. J. GOODALL, E. USSELMANN, J. P. COAD, and D. HOLLAND, "Deuterium Release Measurements in the Be Phase of JET and Determination of Tritium Content in the Exhaust Gas," *J. Nucl. Mater.*, **176&177**, 624 (1990).
146. J. P. COAD, "An Appraisal of Deuterium Retention in JET," *J. Nucl. Mater.*, **226**, 156 (1995).
147. T. LOARER, "Fuel Retention in Tokamaks," presented at 18th Int. Conf. Plasma Surface Interactions, Toledo, Spain, May 26–30 2008, *J. Nucl. Mater.* (submitted for publication).
148. C. H. SKINNER et al., "Modeling of Tritium Retention in TFTR," *J. Nucl. Mater.*, **266–269**, 940 (1999).
149. R.-D. PENZHORN et al., "Tritium Profiles in Tiles from the First Wall of Fusion Machines and Techniques for Their Detritiation," *J. Nucl. Mater.*, **279**, 139 (2000).
150. M. MAYER et al., "The Deuterium Inventory in ASDEX Upgrade," *Nucl. Fusion*, **47**, 1607 (2007).
151. M. MAYER et al., "Carbon Deposition and Deuterium Inventory in ASDEX Upgrade," *Proc. 20th IAEA Fusion Energy Conf.*, IAEA-CN-116/EX/5-24, International Atomic Energy Agency (2005).
152. K. SUGIYAMA, T. TANABE, C. H. SKINNER, and C. A. GENTILE, "Measurement of Tritium Surface Distribution on TFTR Bumper Limiter Tiles," *Phys. Scripta*, **T108**, 68 (2004).
153. T. TANABE et al., "Tritium Distribution Measurement of JET Mk IIGB Divertor Tiles," *J. Nucl. Mater.*, **363–365**, 949 (2007).
154. T. TANABE et al., "Tritium Retention of Plasma Facing Components in Tokamaks," *J. Nucl. Mater.*, **313–316**, 478 (2003).
155. V. ROHDE, M. MAYER, and ASDEX-UPGRADE TEAM, "On the Formation of a-C:D Layers and Parasitic Plasmas Underneath the Roof Baffle of the ASDEX-Upgrade Divertor," *J. Nucl. Mater.*, **313–316**, 337 (2003).
156. K. OHYA, T. TANABE, and J. KAWATA, "Simulation of Redeposition Patterns of Hydrocarbons Released from Carbon Target in Divertors," *Fusion Eng. Des.*, **81**, 205 (2006).
157. K. INAI and K. OHAYA, "Simulation of Hydrocarbon Redeposition in the Gaps Between Divertor Tiles," *J. Nucl. Mater.*, **363–365**, 915 (2007).
158. R. A. CAUSEY, W. L. CHRISMAN, J. CRAWFORD, and J. M. GAHL, "Tritium Retention in Tokamak Disruption-Produced Carbon Debris," *J. Nucl. Mater.*, **210**, 333 (1994).
159. W. J. CARMACK, R. A. ANDERL, R. J. PAWELKO, G. L. SMOLIK, and K. A. McCARTHY, "Characterization and Analysis of Dusts Produced in Three Experimental Tokamaks: TFTR, DIII-D, and Alcator C-Mod," *Fusion Eng. Des.*, **51–52**, 477 (2000).
160. C. H. SKINNER, C. A. GENTILE, M. M. MENON, and R. E. BARRY, "Flaking of Co-Deposited Hydrogenated Carbon Layers on the TFTR Limiter," *Nucl. Fusion*, **39**, 1081 (1999).
161. C. H. SKINNER, C. A. GENTILE, L. CIEBIERA, and S. LANGISH, "Tritiated Dust Levitation by Beta Induced Static Charge," *Fusion Sci. Technol.*, **45**, 11 (2004).
162. N. BEKRIS and R.-D. PENZHORN, "Characterization of Dust and Flakes Generated in Fusion Machines after DD and DT Operations," *Forschungszentrum Karlsruhe Wissenschaftliche Berichte*, Report No. FZKA 6858 (2003).
163. A. L. ROQUEMORE et al., "3D Measurements of Mobile Dust Particle Trajectories in NSTX," *J. Nucl. Mater.*, **363–365**, 222 (2007).
164. A. BADER, C. H. SKINNER, A. L. ROQUEMORE, and S. LANGISH, "Development of an Electrostatic Dust Detector for Use in a Tokamak Reactor," *Rev. Sci. Instrum.*, **75**, 370 (2004).
165. C. H. SKINNER, A. L. ROQUEMORE, A. BADER, W. R. WAMPLER, and NSTX TEAM, "Deposition Diagnostics for Next-Step Devices," *Rev. Sci. Instrum.*, **75**, 4213 (2004).
166. C. VOINIER, C. H. SKINNER and A. L. ROQUEMORE, "Electrostatic Dust Detection on Remote Surfaces," *J. Nucl. Mater.*, **346**, 266 (2005).
167. C. V. PARKER, C. H. SKINNER, and A. L. ROQUEMORE, "Controlling Surface Dust in a Tokamak," *J. Nucl. Mater.*, **363–365**, 1461 (2007).
168. R. A. CAUSEY and T. J. VENHAUS, "The Use of Tungsten in Fusion Reactors: A Review of the Hydrogen Retention and Migration Properties," *Phys. Scripta*, **T94**, 9 (2001).
169. G. R. LONGHURST, "TMAP7: Tritium Migration Analysis Program, User Manual," INEEL/EXT-04-02352, Idaho National Laboratory (2004).
170. M. POON, A. A. HAASZ, and J. W. DAVIS, "Modelling Deuterium Release During Thermal Desorption of D<sup>+</sup>-Irradiated Tungsten," *J. Nucl. Mater.*, **374**, 390 (2008).
171. R. FRAUENFELDER, "Solution and Diffusion of Hydrogen in Tungsten," *J. Vac. Sci. Technol.*, **6**, 388 (1969).
172. L. N. RYABCHIKOV, "Mass Spectrometric Investigation of the Degassing of Molybdenum, Tungsten and Niobium on Heating Them in Vacuum," *Ukr. Fiz. Zh.*, **9**, 293 (1964).
173. A. P. ZAKHAROV, V. M. SHARAPOV, and E. I. EVKO, "Hydrogen Permeability of Mono- and Poly-Crystals of Molybdenum and Tungsten," *Fiz. Khim. Mekh. Mater.*, **9**, 2, 29 (1973).
174. G. BENAMATI, E. SERRA, and C. H. WU, "Hydrogen and Deuterium Transport and Inventory Parameters Through

- W and W-Alloys for Fusion Reactor Applications,” *J. Nucl. Mater.*, **283–287**, 1033 (2000).
175. C. GARCIA-ROSALES, P. FRANZEN, H. PLANK, J. ROTH, and E. GAUTHIER, “Re-Emission and Thermal Desorption of Deuterium from Plasma Sprayed Tungsten Coatings for Application in ASDEX-Upgrade,” *J. Nucl. Mater.*, **233–237**, 803 (1996).
176. P. FRANZEN, C. GARCIA-ROSALES, H. PLANK, and V. ALIMOV, “Hydrogen Trapping in and Release from Tungsten: Modeling and Comparison with Graphite with Regard to Its Use as Fusion Reactor Material,” *J. Nucl. Mater.*, **241–243**, 1082 (1997).
177. A. MAZAYEV, R. AVARBE, and Y. VILK, “Solubility of Hydrogen in Tungsten at High Temperatures and Pressures,” *Izv. Akad. Nauk. USSR Metall.*, **6**, 233 (1968).
178. R. FRAUENFELDER, “Permeation of Hydrogen Through Tungsten and Molybdenum,” *J. Chem. Phys.*, **48**, 3955 (1967).
179. E. AITKEN H. BRASSVIE, P. CONN, E. DUDERSTA, and R. FRYXELL, “Permeability of Tungsten to Hydrogen from 1300 Degrees to 2600 Degrees C and to Oxygen from 2000 Degrees to 2300 Degrees C,” *Trans. Met. Soc. AIME*, **239**, 1565 (1967).
180. R. A. ANDERL, D. HOLLAND, G. LONGHURST, R. PAWELKO, C. TRYBUS, and C. SELLERS, “Deuterium Transport and Trapping in Polycrystalline Tungsten,” *Fusion Technol.*, **21**, 745 (1992).
181. T. NAGASAKI, M. SAIDOH, R. YAMADA, and H. OHNO, “Ion-Driven Permeation and Surface Recombination Coefficient of Deuterium for Iron,” *J. Nucl. Mater.*, **202**, 228 (1993).
182. I. TAKAGI, H. FUJITA, and K. HIGASHI, “Experiments on Potential Energy Diagram for Hydrogen Isotopes on Nickel Surface,” *J. Nucl. Mater.*, **266–269**, 697 (1999).
183. R. CAUSEY, K. WILSON, T. VENHAUS, and W. WAMPLER, “Tritium Retention in Tungsten Exposed to Intense Fluxes of 100 eV Tritons,” *J. Nucl. Mater.*, **266–269**, 467 (1999).
184. A. HAASZ, J. DAVIS, M. POON, and R. MACAULAY-NEWCOMBE, “Deuterium Retention in Tungsten for Fusion Use,” *J. Nucl. Mater.*, **258–263**, 889 (1998).
185. V. KH. ALIMOV, M. MAYER, and J. ROTH, “Differential Cross Section of the  $D(^3\text{He}, p)^4\text{He}$  Nuclear Reaction and Depth Profiling of Deuterium up to Large Depths,” *Nucl. Instrum. Methods B*, **234**, 169 (2005).
186. V. KH. ALIMOV, J. ROTH, and M. MAYER, “Depth Distribution of Deuterium in Single- and Polycrystalline Tungsten up to Depths of Several Micrometers,” *J. Nucl. Mater.*, **337–339**, 619 (2005).
187. V. KH. ALIMOV and J. ROTH, “Hydrogen Isotope Retention in Plasma-Facing Materials: Review of Recent Experimental Results,” *Phys. Scripta*, **T128**, 6 (2007).
188. A. VAN VEEN, J. DE VRIES, D. SEGERS, and G. J. ROZING, “Hydrogen Defect Interaction in Tungsten Observed with PA,” *Positron Annihilation*, p. 543, P. C. JAIN, R. M. SINGRU, and K. P. GOPINATHAN, Eds., World Scientific Publishing Company, Singapore (1985).
189. A. A. HAASZ, M. POON, and J. W. DAVIS, “The Effect of Ion Damage on Deuterium Trapping in Tungsten,” *J. Nucl. Mater.*, **266–269**, 520 (1999).
190. T. VENHAUS, R. CAUSEY, R. DOERNER, and T. ABELN, “Behavior of Tungsten Exposed to High Fluences of Low Energy Hydrogen Isotopes,” *J. Nucl. Mater.*, **290–293**, 505 (2001).
191. W. WANG, J. ROTH, S. LINDIG, and C. H. WU, “Blister Formation of Tungsten due to Ion Bombardment,” *J. Nucl. Mater.*, **299**, 124 (2001).
192. M. Y. YE, H. KANEHARA, S. FUKUDA, N. OHNO, and S. TAKAMURA, “Blister Formation on Tungsten Surface Under Low Energy and High Flux Hydrogen Plasma Irradiation in NAGDIS-I,” *J. Nucl. Mater.*, **313–316**, 72 (2003).
193. T. SHIMADA, Y. UEDA, and M. NISHIKAWA, “Mechanism of Blister Formation on Tungsten Surface,” *Fusion Eng. Des.*, **66–68**, 247 (2003).
194. Y. UEDA, T. SHIMADA, and M. NISHIKAWA, “Impact of Carbon Impurities in Hydrogen Plasmas on Tungsten Blistering,” *Nucl. Fusion*, **44**, 62 (2004).
195. K. TOKUNAGA et al., “Blister Formation and Deuterium Retention on Tungsten Exposed to Low Energy and High Flux Deuterium Plasma,” *J. Nucl. Mater.*, **337–339**, 887 (2005).
196. G.-N. LUO, W. M. SHU, and M. NISHI, “Incident Energy Dependence of Blistering at Tungsten Irradiated by Low Energy High Flux Deuterium Plasma Beams,” *J. Nucl. Mater.*, **347**, 111 (2005).
197. G.-N. LUO, W. M. SHU, and M. NISHI, “Influence of Blistering on Deuterium Retention in Tungsten Irradiated by High Flux Deuterium 10–100 eV Plasmas,” *Fusion Eng. Des.*, **81**, 957 (2006).
198. J. H. EVANS, “The Role of Implanted Gas and Lateral Stress in Blister Formation Mechanisms,” *J. Nucl. Mater.*, **76&77**, 228 (1978).
199. S. K. DAS, M. KAMINSKY, and G. FENSKE, “On the Correlation of Blister Diameter and Blister Skin Thickness in Helium-Ion-Irradiated Nb,” *J. Appl. Phys.*, **50**, 3304 (1979).
200. J. ROTH, “Blistering and Bubble Formation,” *Applications of Ion Beams to Materials*, p. 280, G. CARTER, J. S. COLLIGAN, and N. A. GRANT, Eds., The Institute of Physics, London (1976).
201. E. P. EERNISSE and S. T. PICRAUX, “Role Integrated Lateral Stress in Surface Deformation of He-Implanted Surfaces,” *J. Appl. Phys.*, **48**, 9 (1977).

202. J. B. CONDON and T. SCHOBBER, "Hydrogen Bubbles in Metals," *J. Nucl. Mater.*, **207**, 1 (1993).
203. V. KH. ALIMOV, A. V. GOLUBEVA, and J. ROTH (2006) (unpublished).
204. A. A. HAASZ, J. W. DAVIS, M. POON, and R. G. MACAULAY-NEWCORBE, "Deuterium Retention in Tungsten for Fusion Use," *J. Nucl. Mater.*, **258–263**, 889 (1998).
205. R. CAUSEY, K. WILSON, T. VENHAUS, and W. R. WAMPLER, "Tritium Retention in Tungsten Exposed to Intense Fluxes of 100 eV Tritons," *J. Nucl. Mater.*, **266–269**, 467 (1999).
206. M. POON, R. G. MACAULAY-NEWCORBE, J. W. DAVIS, and A. A. HAASZ, "Flux Dependence of Deuterium Retention in Single Crystal Tungsten," *J. Nucl. Mater.*, **307–311**, 723 (2002).
207. M. POON, A. A. HAASZ, J. W. DAVIS, and R. G. MACAULAY-NEWCORBE, "Impurity Effects and Temperature Dependence of D Retention in Single Crystal Tungsten," *J. Nucl. Mater.*, **313–316**, 199 (2003).
208. M. POON, R. G. MACAULAY-NEWCORBE, J. W. DAVIS, and A. A. HAASZ, "Effects of Background Gas Impurities During D<sup>+</sup> Irradiation on D Trapping in Single Crystal Tungsten," *J. Nucl. Mater.*, **337–339**, 629 (2005).
209. M. W. THOMPSON, *Defects and Radiation Damage in Metals*, Cambridge University (1969).
210. A. D. QUASTEL, J. W. DAVIS, A. A. HAASZ, and R. G. MACAULAY-NEWCORBE, "Effect of Post-D<sup>+</sup>-Irradiation Time Delay and Pre-TDS Heating on D Retention in Single Crystal Tungsten," *J. Nucl. Mater.*, **359**, 8 (2006).
211. H. ELEVELD and A. VAN VEEN, "Void Growth and Thermal Desorption of Deuterium from Voids in Tungsten," *J. Nucl. Mater.*, **212–215**, 1421 (1994).
212. A. V. GOLUBEVA, M. MAYER, J. ROTH, V. A. KURNAEV, and O. V. OGORODNIKOVA, "Deuterium Retention in Rhenium-Doped Tungsten," *J. Nucl. Mater.*, **363–365**, 893 (2007).
213. H. T. LEE, A. A. HAASZ, J. W. DAVIS, and R. G. MACAULAY-NEWCORBE, "Hydrogen and Helium Trapping in Tungsten Under Single and Sequential Irradiations," *J. Nucl. Mater.*, **360**, 196 (2007).
214. H. T. LEE, A. A. HAASZ, J. W. DAVIS, R. G. MACAULAY-NEWCORBE, D. G. WHYTE, and G. M. WRIGHT, "Hydrogen and Helium Trapping in Tungsten Under Simultaneous Irradiations," *J. Nucl. Mater.*, **363–365**, 898 (2007).
215. J. R. FRANSENS, M. S. ABD EL KERIEM, and F. PLEITER, "Hydrogen-Vacancy Interaction in Tungsten," *J. Phys. Condens. Mater.*, **3**, 9871 (1991).
216. V. KH. ALIMOV, K. ERTL, J. ROTH, and K. SCHMID, "Deuterium Retention and Lattice Damage in Tungsten Irradiated with D Ions," *Phys. Scripta*, **T94**, 34 (2001).
217. M. MAYER et al., "Carbon Balance and Deuterium Inventory from a Carbon Dominated to a Full Tungsten ASDEX-Upgrade," presented at 18th Int. Conf. Plasma Surface Interactions, Toledo, Spain, May 26–30, 2008, *J. Nucl. Mater.* (submitted for publication).
218. R. P. DOERNER, "The Implications of Mixed-Material Plasma-Facing Surfaces in ITER" *J. Nucl. Mater.*, **363–365**, 32 (2007).
219. D. M. GOEBEL, G. CAMPBELL, and R. W. CONN, "Plasma-Surface Interaction Experimental Facility (PISCES) for Materials and Edge Physics Studies," *J. Nucl. Mater.*, **121**, 277 (1984).
220. R. P. DOERNER, M. J. BALDWIN, and K. SCHMID, "The Influence of a Beryllium Containing Plasma on the Evolution of a Mixed-Material Surface," *Phys. Scripta*, **T111**, 75 (2004).
221. K. SCHMID, M. BALDWIN, R. DOERNER, and A. WILTNER, "Influence of Beryllium Plasma Impurities on the Erosion of Graphite," *Nucl. Fusion*, **44**, 815 (2004).
222. K. SCHMID, M. BALDWIN, and R. DOERNER, "Influence of Beryllium Plasma Seeding on the Erosion of Carbon," *J. Nucl. Mater.*, **337–339**, 862 (2005).
223. M. J. BALDWIN, K. SCHMID, R. P. DOERNER, A. WILTNER, R. SERAYDARIAN, and CH. LINSMEIER, "Composition and Hydrogen Isotope Retention Analysis of Codeposited C/Be Layers," *J. Nucl. Mater.*, **337–339**, 590 (2005).
224. D. NISHIJIMA, M. J. BALDWIN, R. P. DOERNER, and R. SERAYDARIAN, "Parametric Studies of Carbon Erosion Mitigation Dynamics in Beryllium Seeded Deuterium Plasmas," *J. Nucl. Mater.*, **363–365**, 1261 (2007).
225. M. J. BALDWIN and R. P. DOERNER, "A Time Resolved Study of the Mitigation of Graphite Chemical Erosion in Deuterium Plasmas Containing Beryllium," *Nucl. Fusion*, **46**, 444 (2006).
226. R. P. DOERNER et al., "Interaction of Beryllium Containing Plasma with ITER Materials," *Phys. Scripta*, **T128**, 115 (2007).
227. M. J. BALDWIN et al., "Mixed-Material Layer Formation on Graphite Exposed to Deuterium Plasmas Containing Beryllium," *J. Nucl. Mater.*, **358**, 96 (2006).
228. R. P. DOERNER, A. A. GROSSMAN, S. LUCKHARDT, R. SERAYDARIAN, F. C. SZE, and D. G. WHYTE, "Mixed-Material Coating Formation on Plasma Facing Components," *J. Nucl. Mater.*, **266–269**, 392 (1999).
229. H. OKAMOTO and L. E. TANNER, in *Phase Diagrams of Binary Tungsten Alloys*, S. V. NAGENDRA NAIDU and P.

- RAMO RAO, Eds., Indian Institute of Metals, Calcutta, India (1991).
230. R. P. DOERNER, M. J. BALDWIN, and R. A. CAUSEY, "Beryllium-Tungsten Mixed-Material Interactions," *J. Nucl. Mater.*, **342**, 63 (2005).
231. M. J. BALDWIN, D. BUCHENAUER, R. P. DOERNER, R. A. CAUSEY, W. M. CLIFT, and K. SCHMID, "Be-W Alloy Formation in Static and Divertor-Plasma Simulator Experiments," *J. Nucl. Mater.*, **363–365**, 1179 (2007).
232. CH. LINSMEIER et al., "Binary Beryllium-Tungsten Mixed Materials," *J. Nucl. Mater.*, **363–365**, 1129 (2007).
233. V. KH. ALIMOV and J. ROTH, Personal Communication.
234. V. KH. ALIMOV and D. A. KOMAROV, "Deuterium Retention in Carbon and Tungsten-Carbon Mixed Films Deposited by Magnetron Sputtering in D<sub>2</sub> Atmosphere," *J. Nucl. Mater.*, **313–316**, 599 (2003).
235. H. YOSHIDA et al., "Deuterium Retention in Carbon Dust and Carbon-Tungsten Mixed Dust Prepared by Deuterium Arc Discharge," *J. Nucl. Mater.*, **329–333**, 790 (2004).
236. K. KATAYAMA, T. KAWASAKI, Y. MANABE, H. NAGASE, T. TAKRISHI, and M. NISHIKAWA, "Hydrogen Retention in Carbon-Tungsten Co-Deposition Layer Formed by Hydrogen RF Plasma," *Thin Solid Films*, **506–507**, 188 (2006).
237. M. POON, J. W. DAVIS, and A. A. HAASZ, "Effect of Carbon Pre-Implantation on Deuterium Retention in Tungsten," *J. Nucl. Mater.*, **283–287**, 1062 (2000).
238. S. K. ERENTS, R. A. PITTS, W. FUNDAMENSKI, J. P. GUNN, and G. F. MATTHEWS, "A Comparison of Experimental Measurements and Code Results to Determine Flows in the JET SOL," *Plasma Phys. Control. Fusion*, **46**, 1757 (2004).
239. J. P. COAD et al., "Erosion/Deposition Issues at JET," *J. Nucl. Mater.*, **290–293**, 224 (2001).
240. G. FEDERICI et al., "Assessment of Erosion and Tritium Codeposition in ITER-Feat," *J. Nucl. Mater.*, **290–293**, 260 (2001).
241. C. H. SKINNER and G. FEDERICI, "Is Carbon a Realistic Choice for ITER's Divertor?" *Phys. Scripta*, **T124**, 18 (2006).
242. A. A. HAASZ, S. CHIU, J. E. PIERRE, and Y. I. GUDIMENKO, "Thermo-Oxidative Erosion of Amorphous Hydrogenated Carbon Films," *J. Vac. Sci. Technol. A*, **14**, 184 (1996).
243. S. ALBERICI, H. K. HINSSSEN, R. MOORNMANN, and C. H. WU, "Deuterium Release Rates in a-C:D-Layers During Oxygen Attack," *J. Nucl. Mater.*, **266–269**, 754 (1999).
244. A. A. HAASZ, C. TSUI, J. W. DAVIS, and R. OCHOUKOV, "Thermo-Oxidation of Codeposits from DIII-D Divertor Tiles," *Phys. Scripta*, **T128**, 55 (2007).
245. R. OCHOUKOV, A. A. HAASZ, and J. W. DAVIS, "Pressure Dependence of Oxidative Removal of Tokamak Codeposits," *Phys. Scripta*, **T124**, 27 (2006).
246. J. W. DAVIS, P. B. WRIGHT, R. G. MACAULAY-NEWCOMBE, A. A. HAASZ, and C. G. HAMILTON, "Chemical Erosion of Boronized Films from DIII-D Tiles," *J. Nucl. Mater.*, **290–293**, 66 (2001).
247. P. B. WRIGHT, J. W. DAVIS, R. G. MACAULAY-NEWCOMBE, C. G. HAMILTON, and A. A. HAASZ, "Chemical Erosion of DIII-D Divertor Tile Specimens," *J. Nucl. Mater.*, **313–316**, 158 (2003).
248. J. W. DAVIS and A. A. HAASZ, "Oxygen Removal of Codeposited a-C:D Layers from Tokamak Tiles," *J. Nucl. Mater.*, **266–269**, 478 (1999).
249. J. W. DAVIS, C. G. HAMILTON, and A. A. HAASZ, "O<sub>2</sub> Erosion of Graphite Tile Substrates," *J. Nucl. Mater.*, **288**, 148 (2001).
250. C. K. TSUI, A. A. HAASZ, J. W. DAVIS, J. P. COAD, and J. LIKONEN, "Thermo-Oxidation of Be-Containing Codeposits from JET Divertor Tiles," *Nucl. Fusion*, 035008 (2008).
251. V. PHILIPPS, H. G. ESSER, and J. VON SEGGERN, "Removal of Redeposited Layers and Hydrogen Release by Oxygen Ventilation of TEXTOR-94," *J. Nucl. Mater.*, **266–269**, 386 (1999).
252. J. S. HU, J. G. LI, X. M. WANG, Y. P. ZHAO, and HT-7 TEAM, "Oxidation for Deposits Removal and Hydrogen Release on HT-7," *J. Nucl. Mater.*, **363–365**, 862 (2007).
253. C. L. KUNZ, R. A. CAUSEY, M. CLIFT, W. R. WAMPLER, and D. F. COWGILL, "Removal of the Codeposited Carbon Layer Using He-O Glow Discharge," *J. Nucl. Mater.*, **367–370**, 1512 (2007).
254. W. L. HSU, "Glow-Discharge Removal of Codeposited Carbon Films in Graphite-Lined Tokamak Reactors," *J. Vac. Sci. Technol. A*, **7**, 1047 (1989).
255. W. JACOB, B. LANDKAMMER, and C. H. WU, "Removal of Codeposited Layers by ECR Discharge Cleaning," *J. Nucl. Mater.*, **266–269**, 552 (1999).
256. D. F. COWGILL, Sandia National Laboratories (1992) (unpublished).
257. C. H. SKINNER, H. KUGEL, D. MUELLER, B. L. DOYLE, and W. R. WAMPLER, "Tritium Removal by CO<sub>2</sub> Laser Heating," *Proc. 17th IEEE/NPSS Symp. Fusion Engineering*, San Diego, California, 1997, p. 321, Institute of Electrical and Electronics Engineers Nuclear and Plasma Sciences Society (1998).
258. D. WATANABE et al., "Properties of Hydrogen Desorption from Co-Deposits on JT-60 Graphite Tile by Pulsed-Laser Ablation," *J. Nucl. Mater.*, **363–365**, 972 (2007).

259. K. TUKONAGA, H. YAGI, S. FUKUDA, T. MUROGA, and N. YOSHIDA, "Effects of Deuterium Ion Irradiation on Gas Emission and Sublimation of Graphite by Pulse High Heat Load," *J. Nucl. Mater.*, **212–215**, 1467 (1994).
260. D. KEROACK and B. TERREAULT, "Re-Emission of Deuterium Implanted in Carbon by Laser Desorption," *J. Nucl. Mater.*, **231**, 47 (1996).
261. Y. OYA et al., "Re-Emission of Deuterium Implanted in Carbon by Laser Desorption," *J. Nucl. Mater.*, **290–293**, 469 (2001).
262. W. M. SHU et al., "Tritium Decontamination of TFTR Carbon Tiles Employing Ultra-Violet Light," *J. Nucl. Mater.*, **290–293**, 482 (2001).
263. D. D. R. SUMMERS et al., "In-Situ Measurement of Hydrogen Retention in JET Carbon Tiles," *J. Nucl. Mater.*, **290–293**, 496 (2001).
264. A. HUBER et al., "In-Situ Measurements of Trapped Hydrogen by Laser by Laser Desorption in TEXTOR-94," *Phys. Scripta*, **T94**, 102 (2001).
265. C. H. SKINNER et al., "Tritium Removal from Codeposits on Carbon Tiles by a Scanning Laser," *J. Nucl. Mater.*, **301**, 98 (2002).
266. W. M. SHU, Y. KAWAKUBO, and M. F. NISHI, "Tritium Recovery from Co-Deposited Layers Using 193-nm Laser," *Appl. Phys. A*, **76**, 421 (2003).
267. C. H. SKINNER, N. BEKRIS, J. P. COAD, C. A. GENTILE, and M. GLUGLA, "Tritium Removal from JET and TFTR Tiles by a Scanning Laser," *J. Nucl. Mater.*, **313–316**, 496 (2003).
268. W. M. SHU, Y. KAWAKUBO, K. MASAKI, and M. F. NISHI, "Ablative Removal of Codeposits on JT-60 Carbon Tiles by an Excimer Laser," *J. Nucl. Mater.*, **313–316**, 584 (2003).
269. C. H. SKINNER et al., "Thermal Response of Tritiated Codeposits from JET and TFTR to Transient Heat Pulses," *Phys. Scripta*, **T103**, 34 (2003).
270. F. LE GUERN, C. HUBERT, S. MOUSSET, E. GAUTHIER, C. BLANC, P. WODLING, and J. M. WEULERSSE, "Laser Ablation Tests Performed on TORE-SUPRA Graphite Samples," *J. Nucl. Mater.*, **410–416**, 410 (2004).
271. K. J. GIBSON, G. F. COUNSELL, C. CURRAN, M. J. FORREST, M. J. KAY, and K. G. WATKINS, "The Removal of Co-Deposited Hydrocarbon Films from Plasma Facing Components Using High-Power Pulsed Flashlamp Irradiation," *J. Nucl. Mater.*, **337–339**, 565 (2005).
272. B. SCHWEER et al., "Laser Desorption of Deuterium Retained in Re-Deposited Carbon Layers at TEXTOR and JET," *J. Nucl. Mater.*, **337–339**, 570 (2005).
273. B. EMMOTH et al., "Fuel Removal from Bumper Limiter Tiles by Using a Pulsed Excimer Laser," *J. Nucl. Mater.*, **337–339**, 639 (2005).
274. T. SHIBAHARA, Y. SAKAWA, and T. TANABE, "Hydrogen Release Behavior from Graphite Under Pulsed Laser Irradiation," *J. Nucl. Mater.*, **337–339**, 654 (2005).
275. Y. SAKAWA, T. SHIBAHARA, K. SATO, and T. TANABE, "Pulsed Laser Ablation of Hydrogen-Implanted Graphite Target," *J. Plasma Fusion Res. Ser.*, **7**, 138 (2006).
276. Y. SAKAWA, K. SATO, T. SHIBAHARA, and T. TANABE, "Ablation of Hydrogen-Implanted Graphite Target Using Pulsed Laser Beam," *Fusion Eng. Des.*, **81**, 381 (2006).
277. E. G. GAMALY, A. V. RODE, and B. LUTHER-DAVIES, "Laser Ablation of Carbon at the Threshold of Plasma Formation," *Appl. Phys. A*, **69** (Suppl.), S121 (1999).
278. Y. SAKAWA, D. WATANABE, T. SHIBAHARA, K. SUGIYAMA, and T. TANABE, "Pulsed-Laser Ablation of Co-Deposits on JT-60 Graphite Tile," *J. Nucl. Mater.*, **367–370**, 1516 (2007).
279. A. WIDDOWSON et al., "Efficacy of Photon Cleaning of JET Divertor Tiles," *J. Nucl. Mater.*, **363–365**, 341 (2007).
280. C. H. SKINNER, C. GENTILE, J. HOSEA, D. MUELLER, G. FEDERICI, and R. HAANGE, "Report on the IEA Workshop Tritium Experience in Large Tokamaks; Application to ITER," *Nucl. Fusion*, **39**, 271 (1999).
281. C. H. SKINNER and G. FEDERICI, "Tritium Issues in Next Step Devices," *Proc. Int. Conf. Advanced Diagnostics for Magnetic and Inertial Fusion*, Varenna, Italy, September 3–7, 2001, in *Advanced Diagnostics for Magnetic and Inertial Fusion*, p. 277, P. E. STOTT et al., Eds., Kluwer Academic/Plenum Publishers, New York (2002).
282. T. ÅKERMARK, B. EMMOTH, and H. BERGSÅKER, "Laser Annealing in Combination with Mass Spectroscopy, A Technique to Study Deuterium on Tokamak Carbon Samples, A Tool for Detritiation," *J. Nucl. Mater.*, **359**, 220 (2006).
283. T. ÅKERMARK, B. EMMOTH, and A. PISAREV, Private Communication.
284. A. WIDDOWSON et al., "Detritiation of JET Tiles by Laser Cleaning," *J. Fusion Sci. Technol.*, **54**, 51 (2008).
285. N. BEKRIS et al., "Characterisation of Flakes Generated in JET after DD and DT Plasma Operations," *J. Nucl. Mater.*, **337–339**, 659 (2005).
286. J. D. COX, "A Bond Energy Scheme for Aliphatic and Benzenoid Compounds," *Tetrahedron*, **18**, 1337 (1962).
287. N. BEKRIS, J. P. COAD, C. H. SKINNER, C. A. GENTILE, E. DAMM, and W. NAEGLE, "Thermal Release Rate of Tritium Trapped in Bulk and Plasma Exposed Surfaces of Carbon Specimens Obtained from JET Divertor," *J. Nucl. Mater.*, **367–370**, 1254 (2007).

288. Y. TORIKAI, A. PISAREV, M. MATSUYAMA, and K. WATANABE, Toyama University (2002) (unpublished).
289. M. J. BALDWIN, K. SCHMID, R. P. DOERNER, A. WILTNER, R. SERAYDARIAN, and C. LINSMEIER, "Composition and Hydrogen Isotope Retention Analysis of Co-Deposited C/Be Layers," *J. Nucl. Mater.*, **337–339**, 590 (2005).
290. R. A. CAUSEY, W. R. WAMPLER, and D. S. WALSH, "Comparison of the Thermal Stability of the Codeposited Carbon/Hydrogen Layer to That of the Saturated Implant Layer," *J. Nucl. Mater.*, **176&177**, 987 (1990). [Note for web searching: this paper is listed as being on p. 992 though the paper version and downloaded article bear the page number 987.]
291. E. B. MESERVEY et al., "The Effect of Plasma Surface Interactions on PLT Plasma Parameters," *J. Nucl. Mater.*, **93–94**, 267 (1980).
292. S. CIATTAGLIA et al., "An Integrated Approach of In-Vacuum Vessel Dust and Tritium Inventory Control in ITER," *Proc. Symp. Fusion Technology*, Rostock, Germany, September 2008, *Fusion Eng. Des.* (to be published).